

Spectral Sparsification for Communication-Efficient Collaborative Rotation and Translation Estimation

Yulun Tian and Jonathan P. How

Abstract—We propose fast and communication-efficient optimization algorithms for multi-robot rotation averaging and translation estimation problems that arise from collaborative simultaneous localization and mapping (SLAM), structure-from-motion (SfM), and camera network localization applications. Our methods are based on theoretical relations between the Hessians of the underlying Riemannian optimization problems and the Laplacians of suitably weighted graphs. We leverage these results to design a collaborative solver in which robots coordinate with a central server to perform approximate second-order optimization, by solving a *Laplacian system* at each iteration. Crucially, our algorithms permit robots to employ *spectral sparsification* to sparsify intermediate dense matrices before communication, and hence provide a mechanism to trade off accuracy with communication efficiency with provable guarantees. We perform rigorous theoretical analysis of our methods and prove that they enjoy (local) *linear* rate of convergence. Furthermore, we show that our methods can be combined with graduated non-convexity to achieve *outlier-robust* estimation. Extensive experiments on real-world SLAM and SfM scenarios demonstrate the superior convergence rate and communication efficiency of our methods.

Index Terms—Simultaneous localization and mapping, optimization, multi-robot systems.

I. INTRODUCTION

Collaborative spatial perception is a fundamental capability for multi-robot systems to operate in unknown, GPS-denied environments. State-of-the-art systems (*e.g.*, [1]–[6]) rely on optimization-based back-ends to achieve accurate multi-robot simultaneous localization and mapping (SLAM). Often, a central server receives data from all robots (*e.g.* in the form of factor graphs [7]) and solves the underlying large-scale optimization for the entire team. In comparison, *collaborative optimization* frameworks leverage robots’ local computation and iterative communication (either peer-to-peer or coordinated by a server), and thus have the potential to scale to larger scenes and support more robots.

Recent works focus on developing fully distributed algorithms in which robots carry out iterative optimization via peer-to-peer message passing [8]–[13]. While these methods are flexible in terms of the required communication architecture, they often suffer from slow convergence due to their first-order nature and the inherent poor conditioning of typical

SLAM problems. To resolve the slow convergence issue, an alternative is to pursue a *second-order* optimization framework. A prominent example is DDF-SAM [14]–[16], in which robots marginalize out internal variables (*i.e.*, those without inter-robot measurements) in their local factor graphs before communication. From an optimization perspective, robots partially eliminate their local Hessians and communicate the resulting matrices. However, a shortcoming of this approach is that the transmitted matrices are usually *dense* (even if the original problem is sparse), and hence could result in long transmission times that prevent the team from obtaining a timely solution.

To address the aforementioned technical gaps, this work presents results towards collaborative optimization that achieves both *fast convergence* and *efficient communication*. Specifically, we develop new algorithms for solving multi-robot rotation averaging and translation estimation. These problems are fundamental and have applications ranging from initialization for pose graph SLAM [17], structure-from-motion (SfM) [18], and camera network localization [8]. Our approach is based on a server-client architecture (Fig. 1a), in which multiple robots (clients) coordinate with a server to collaboratively solve the optimization problem leveraging local computation. The crux of our method lies in exploiting theoretical relations between the Hessians of the optimization problems and the Laplacians of the underlying graphs. We leverage these theoretical insights to develop a fast collaborative optimization method in which each iteration computes an *approximate second-order* update by replacing the Hessian with a *constant* Laplacian matrix, which improves efficiency in both computation and communication. Furthermore, during communication, robots use *spectral sparsification* [19], [20] to sparsify intermediate dense matrices resulted from elimination of its internal variables. Figs. 1b to 1d show a high-level illustration of our approach. By varying the degree of sparsification, our method thus provides a principled way for trading off accuracy with communication efficiency. The theoretical properties of spectral sparsification allow us to perform rigorous convergence analysis, and establish *linear* rates of convergence for our methods. Lastly, we also present an extension to *outlier-robust* estimation by combining our approach with graduated non-convexity (GNC) [21], [22].

Contributions. The key contributions of this work are summarized as follows:

- We present collaborative optimization algorithms for multi-robot rotation averaging and translation estimation under the server-client architecture, which enjoy fast convergence (in terms of the number of iterations) and efficient communication through the use of *spectral sparsification*.
- In contrast to the typical sublinear convergence of prior methods, we prove (local) *linear convergence* for our meth-

The authors are with the Department of Aeronautics and Astronautics, Massachusetts Institute of Technology, 77 Massachusetts Ave, Cambridge, MA 02139, USA. {yulun, jhow}@mit.edu. This work was supported in part by ARL DCIST under Cooperative Agreement Number W911NF-17-2-0181, and in part by ONR under BRC Award N000141712072.

The authors gratefully acknowledge Dr. Kaveh Fathian, Parker Lusk, Dr. Kasra Khosoussi, Dr. David M. Rosen, and anonymous reviewers for helpful comments. The authors would also like to thank Prof. Pierre-Antoine Absil for insightful discussions on the linear convergence of approximate Newton methods on Riemannian manifolds.

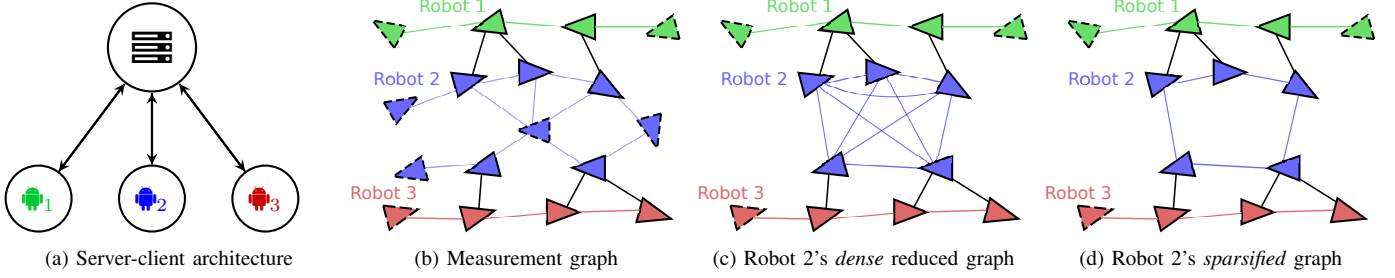


Fig. 1: (a) Information flow in server-client architecture. Each communication round consists of an *upload* stage (clients to server) and a *download* stage (server to clients). (b) Example 3-robot problem visualized as a graph. For each robot $\alpha \in \{1, 2, 3\}$, its vertices (variables) \mathcal{V}_α are shown in a distinct color. Each edge corresponds to a relative measurement between two variables. Separators (solid line) correspond to variables with inter-robot measurements, and the remaining variables form the interior vertices (dashed line). (c) For robot 2, elimination of its interior vertices creates a *dense* matrix S_2 , which corresponds to a dense graph over its separators. (d) In our approach, robot 2 achieves communication efficiency by transmitting a sparse approximation \tilde{S}_2 of the original dense matrix S_2 , which also corresponds to a sparsified graph over its separators.

ods and show that the rate of convergence depends on the user-defined sparsification parameter.

- We present an extension to *outlier-robust* estimation by combining the proposed algorithms with GNC.
- We perform extensive evaluations of our methods and demonstrate their values on real-world SLAM and SfM scenarios with outlier measurements.

Lastly, while our algorithms and theoretical guarantees cover separate rotation averaging and translation estimation, we demonstrate through our experiments that their combination can be used to achieve robust initialization for pose graph optimization (PGO), which is another fundamental problem commonly used in collaborative SLAM.

Paper Organization. The rest of this paper is organized as follows. The remainder of this section introduces necessary notation and mathematical preliminaries, and in Sec. II, we review related works. Sec. III formally introduces the problem formulation, communication architecture, and relevant applications. In Sec. IV, we establish theoretical relations between the Hessians and the underlying graph Laplacians. Then, in Sec. V, we leverage these theoretical results to design fast and communication-efficient solvers for the problems of interest and establish convergence guarantees. Finally, Sec. VI presents numerical evaluations of the proposed algorithms.

Notations and Preliminaries

Table V in the appendix summarizes detailed notations used in this work. Unless stated otherwise, lowercase and uppercase letters denote vectors and matrices, respectively. We define $[n] \triangleq \{1, 2, \dots, n\}$ as the set of positive integers from 1 to n .

Linear Algebra and Spectral Approximation. \mathcal{S}^n and \mathcal{S}_+^n denote the set of $n \times n$ symmetric and symmetric positive semidefinite matrices, respectively. We use \otimes to denote the Kronecker product. For a positive integer n , $\mathbf{1}_n \in \mathbb{R}^n$ and $I_n \in \mathbb{R}^{n \times n}$ denote the vector of all ones and the Identity matrix. For any matrix A , $\ker(A)$ and $\text{image}(A)$ denote the kernel (nullspace) and image (span of column vectors) of A , respectively. A^\dagger denotes the Moore-Penrose inverse of A , which coincides with the inverse A^{-1} when A is invertible. When $A \in \mathcal{S}^n$, $\lambda_1(A), \dots, \lambda_n(A)$ denote the real eigenvalues of A sorted in increasing order. When $A \in \mathcal{S}_+^n$, we also define $\|X\|_A \triangleq \sqrt{\text{tr}(X^\top A X)}$ where X is of compatible dimensions.

Following [23], [24], for $A, B \in \mathcal{S}^n$ and $\epsilon > 0$, we say that B is an ϵ -approximation of A , denoted as $A \approx_\epsilon B$, if the following holds,

$$e^{-\epsilon} B \preceq A \preceq e^\epsilon B, \quad (1)$$

where $B \preceq A$ means $A - B \in \mathcal{S}_+^n$. Note that (1) is symmetric and holds under composition: if $A \approx_\epsilon B$ and $B \approx_\delta C$, then $A \approx_{\epsilon+\delta} C$. Furthermore, if A is singular, the relation (1) implies that B is necessarily singular and $\ker(A) = \ker(B)$.

Graph Theory. A weighted undirected graph is denoted as $G = (\mathcal{V}, \mathcal{E}, w)$, where \mathcal{V} and \mathcal{E} denote the vertex and edge sets, and $w : \mathcal{E} \rightarrow \mathbb{R}_{>0}$ is the edge weight function that assigns each edge $(i, j) \in \mathcal{E}$ a positive weight w_{ij} . For a graph G with n vertices, its *graph Laplacian* $L(G; w) \in \mathcal{S}_+^n$ is defined as,

$$L(G; w)_{ij} = \begin{cases} \sum_{k \in \text{Nbr}(i)} w_{ik}, & \text{if } i = j, \\ -w_{ij}, & \text{if } i \neq j, (i, j) \in \mathcal{E}, \\ 0, & \text{otherwise.} \end{cases} \quad (2)$$

In (2), $\text{Nbr}(i) \subseteq \mathcal{V}$ denotes the neighbors of vertex i in the graph. Our notation $L(G; w)$ serves to emphasize that the Laplacian of G depends on the edge weight w . When the edge weight w is irrelevant or clear from context, we will write the graph as $G = (\mathcal{V}, \mathcal{E})$ and its Laplacian as $L(G)$ or simply L . The graph Laplacian L always has a zero eigenvalue, i.e., $\lambda_1(L) = 0$. The second smallest eigenvalue $\lambda_2(L)$ is known as the *algebraic connectivity*, which is always positive for connected graphs.

Riemannian Manifolds. The reader is referred to [25], [26] for a comprehensive review of optimization on matrix manifolds. In general, we use \mathcal{M} to denote a smooth matrix manifold. For integer $n > 1$, \mathcal{M}^n denotes the product manifold formed by n copies of \mathcal{M} . $T_x \mathcal{M}$ denotes the tangent space at $x \in \mathcal{M}$. For tangent vectors $\eta, \xi \in T_x \mathcal{M}$, their inner product is denoted as $\langle \eta, \xi \rangle_x$, and the corresponding norm is $\|\eta\|_x = \sqrt{\langle \eta, \eta \rangle_x}$. In the rest of the paper, we drop the subscript x as it will be clear from context. At $x \in \mathcal{M}$, the injectivity radius $\text{inj}(x)$ is a positive constant such that the exponential map $\text{Exp}_x : T_x \mathcal{M} \rightarrow \mathcal{M}$ is a diffeomorphism when restricted to the domain $U = \{\eta \in T_x \mathcal{M} : \|\eta\| < \text{inj}(x)\}$. In this case, we define the logarithm map to be $\text{Log}_x \triangleq \text{Exp}_x^{-1}$. Unless otherwise mentioned, we use $\text{d}(x, y)$ to denote the geodesic distance between two points $x, y \in \mathcal{M}$ induced by

the Riemannian metric. In addition, it holds that $d(x, y) = \|v\|$ where $v = \text{Log}_x(y)$; see [26, Proposition 10.22].

The Rotation Group $\text{SO}(d)$. The rotation group is denoted as $\text{SO}(d) = \{R \in \mathbb{R}^{d \times d} : R^\top R = I, \det(R) = 1\}$. The tangent space at R is given by $T_R \text{SO}(d) = \{RV : V \in \text{so}(d)\}$, where $\text{so}(d)$ is the space of $d \times d$ skew-symmetric matrices. In this work, we exclusively work with 2D and 3D rotations. We define a basis for $T_R \text{SO}(3)$ such that each tangent vector $\eta \in T_R \text{SO}(3)$ is identified with a vector $v \in \mathbb{R}^3$,

$$\eta = R[v]_\times = R \begin{bmatrix} 0 & -v_3 & v_2 \\ v_3 & 0 & -v_1 \\ -v_2 & v_1 & 0 \end{bmatrix}. \quad (3)$$

Note that (3) defines a bijection between $\eta \in T_R \text{SO}(3)$ and $v \in \mathbb{R}^3$. For $d = 2$, we can define a similar basis for the 1-dimensional tangent space $T_R \text{SO}(2)$, where each tangent vector $\eta \in T_R \text{SO}(2)$ is identified by a scalar $v \in \mathbb{R}$ as,

$$\eta = R[v]_\times = R \begin{bmatrix} 0 & -v \\ v & 0 \end{bmatrix}. \quad (4)$$

We have overloaded the notation $[\cdot]_\times$ to map the input scalar or vector to the corresponding skew-symmetric matrix in $\text{so}(2)$ or $\text{so}(3)$. Under the basis given in (3) and (4), the inner product on the tangent space is defined by the corresponding vector dot product, i.e., $\langle \eta_1, \eta_2 \rangle = v_1^\top v_2$ where $v_1, v_2 \in \mathbb{R}^p$ are vector representations of η_1 and η_2 , and $p = \dim \text{SO}(d) = d(d-1)/2$. We define the function $\text{Exp} : \mathbb{R}^p \rightarrow \text{SO}(d)$ as,

$$\text{Exp}(v) = \exp([v]_\times), \quad (5)$$

where $\exp(\cdot)$ denotes the conventional matrix exponential. Note that $\text{Exp} : \mathbb{R}^p \rightarrow \text{SO}(d)$ should not be confused with the exponential mapping on Riemannian manifolds $\text{Exp}_x : T_x \mathcal{M} \rightarrow \mathcal{M}$, although the two are closely related in the case of rotations. Specifically, at a point $R \in \text{SO}(d)$ where $d \in \{2, 3\}$, the exponential map can be written as $\text{Exp}_R(\eta) = R \text{Exp}(v)$. Lastly, we also denote Log as the inverse of Exp in (5).

II. RELATED WORKS

In this section, we review related work in collaborative SLAM (Sec. II-A), graph structure on rotation averaging and PGO (Sec. II-B), and the applications of spectral sparsification and Laplacian linear solvers (Sec. II-C).

A. Collaborative SLAM

Systems. State-of-the-art collaborative SLAM systems rely on optimization-based back-ends to accurately estimate robots' trajectories and maps in a global reference frame. In *fully centralized* systems (e.g., [1]–[3]), robots upload their processed measurements to a central server that in practice could contain e.g., odometry factors, visual keyframes, and/or lidar keyed scans. Using this information, the server is responsible for managing the multi-robot maps and solving the entire back-end optimization problem. In contrast, in systems leveraging *distributed* computation (e.g. [4]–[6], [18], [27]), robots collaborate to solve back-end optimization by coordinating with a server or among themselves. The resulting communication usually involves exchanging intermediate iterates needed by distributed optimization to attain convergence.

Optimization Algorithms. To solve factor graph optimization in a multi-robot setting, Cunningham *et al.* develop DDF-SAM [14], [16] where each agent communicates a “condensed graph” produced by marginalizing out internal variables (those without inter-robot measurements) in its local Gaussian factor graph. Researchers have also developed information-based sparsification methods to sparsify the dense information matrix after marginalization using Chow-Liu tree (e.g., [28], [29]) or convex optimization (e.g., [30], [31]). In these works, sparsification is guided by an information-theoretic objective such as the Kullback-Leibler divergence, and requires linearization to compute the information matrix. In comparison, our approach sparsifies the graph Laplacian that does not depend on linearization, and furthermore the sparsified results are used by collaborative optimization to achieve fast convergence.

From an optimization perspective, marginalization corresponds to a domain decomposition approach (e.g., see [32, Chapter 14]) where one eliminates a subset of variables in the Hessian using the Schur complement. Related works use sparse approximations of the resulting matrix (e.g., with tree-based sparsity patterns) to precondition the optimization [33]–[36]. Recent work [27] combines domain decomposition with event-triggered transmission to improve communication efficiency during collaborative estimation. Zhang *et al.* [37] develop a centralized incremental solver for multi-robot SLAM. Fully decentralized solvers for SLAM have also gained increasing attention; see [8]–[13], [38]. In the broader field of optimization, related works include decentralized consensus optimization methods such as [39]–[42]. Compared to these fully decentralized methods, the proposed approach assumes a central server but achieves significantly faster convergence by implementing approximate second-order optimization.

B. Graph Structure in Rotation Averaging and PGO

Prior works have investigated the impact of graph structure on rotation averaging and PGO problems from different perspectives. One line of research [43]–[45] adopts an estimation-theoretic approach and shows that the Fisher information matrix is closely related to the underlying graph Laplacian matrix. Eriksson *et al.* [46] establish sufficient conditions for strong duality to hold in rotation averaging, where the derived analytical error bound depends on the algebraic connectivity of the graph. Recently, Bernreiter *et al.* [47] use tools from graph signal processing to correct onboard estimation errors in multi-robot mapping. Doherty *et al.* [48] propose a measurement selection approach for pose graph SLAM that seeks to maximize the algebraic connectivity of the underlying graph. This paper differs from the aforementioned works by analyzing the impact of graph structure on the underlying optimization problems, and exploiting the theoretical analysis to design novel optimization algorithms in the multi-robot setting.

Among related works in this area, the ones most related to this paper are [49]–[53]. Carlone [49] analyzes the influences of graph connectivity and noise level on the convergence of Gauss-Newton methods when solving PGO. Tron [50] derives the Riemannian Hessian of rotation averaging under the geodesic distance, and uses the results to prove convergence of Riemannian gradient descent. In a pair of

papers [51], [52], Wilson *et al.* study the local convexity of rotation averaging under the geodesic distance, by bounding the Riemannian Hessian using the Laplacian of a suitably weighted graph. Recently, Nasiri *et al.* [53] develop a Gauss-Newton method for rotation averaging under the chordal distance, and show that its convergence basin is influenced by the norm of the inverse reduced Laplacian matrix. Our work differs from [49]–[53] by focusing on the development of fast and communication-efficient solvers in multi-robot teams with provable performance guarantees. During this process, we also prove new results on the connections between the Riemannian Hessian and graph Laplacian, and show that they hold under both geodesic and chordal distance.

C. Spectral Sparsification and Laplacian Solvers

A remarkable property of graph Laplacians is that they admit sparse approximations; see [19] for a survey. Spielman and Srivastava [20] show that every graph with n vertices can be approximated using a sparse graph with $O(n \log n)$ edges. This is achieved using a random sampling procedure that selects each edge with probability proportional to its effective resistance, which intuitively measures the importance of each edge to the whole graph. Batson *et al.* [54] develop a procedure based on the so-called barrier functions for constructing *linear-sized* sparsifiers. Another line of work [55], [56] employs sparsification during approximate Gaussian elimination. Spectral sparsification is one of the main tools that enables recent progress in fast Laplacian solvers (*i.e.*, for solving linear systems of the form $Lx = b$, where L is a graph Laplacian); see [57] for a survey. Peng and Spielman [58] develop a parallel solver that invokes sparsification as a subroutine, which is improved and extended in following works [23], [24]. Recently, Tutunov [59] extends the approach in [58] to solve decentralized consensus optimization problems. In this work, we leverage spectral sparsification to design communication-efficient collaborative optimization methods for rotation averaging with provable convergence guarantees.

III. PROBLEM FORMULATION

This section formally defines the rotation averaging and translation estimation problems in the multi-robot context. For clarity, here we introduce the problems without considering outlier measurements, and present extensions to outlier-robust optimization in Sec. V-D. We review the communication and computation architectures used by our algorithms. Finally, we discuss relevant applications in multi-robot SLAM and SfM.

A. Rotation Averaging

We model rotation averaging using an undirected *measurement graph* $G = (\mathcal{V}, \mathcal{E})$. Each vertex $i \in \mathcal{V} = [n]$ corresponds to a rotation variable $R_i \in \text{SO}(d)$ to be estimated. Each edge $(i, j) \in \mathcal{E}$ corresponds to a noisy relative measurement of the form,

$$\tilde{R}_{ij} = \underline{R}_i^\top \underline{R}_j R_{ij}^{\text{err}}, \quad (6)$$

where $\underline{R}_i, \underline{R}_j \in \text{SO}(d)$ are the latent (ground truth) rotations and $R_{ij}^{\text{err}} \in \text{SO}(d)$ is the measurement noise. In standard rotation averaging, we aim to estimate the rotations by minimizing

the sum of squared measurement residuals, which corresponds to the formulation in Problem 1.

Problem 1 (Rotation Averaging).

$$\underset{R=(R_1, \dots, R_n) \in \text{SO}(d)^n}{\text{minimize}} \quad \sum_{(i,j) \in \mathcal{E}} \kappa_{ij} \varphi(R_i \tilde{R}_{ij}, R_j). \quad (7)$$

For each edge $(i, j) \in \mathcal{E}$, $\kappa_{ij} > 0$ is the corresponding measurement weight. The function φ is defined as either the squared geodesic (8a) or chordal distance (8b),

$$\varphi(R_i \tilde{R}_{ij}, R_j) \triangleq \begin{cases} \frac{1}{2} \left\| \text{Log}(\tilde{R}_{ij}^\top R_i^\top R_j) \right\|^2, & (8a) \\ \frac{1}{2} \left\| R_i \tilde{R}_{ij} - R_j \right\|_F^2. & (8b) \end{cases}$$

In the multi-robot setting, each robot owns a subset of all rotation variables and only knows about measurements involving its own variables; see Fig. 1b for an illustration.

B. Translation Estimation

Similar to rotation averaging, we also consider the problem of estimating multiple translation vectors given noisy relative translation measurements.

Problem 2 (Translation Estimation).

$$\underset{t=(t_1, \dots, t_n) \in \mathbb{R}^{d \times n}}{\text{minimize}} \quad \sum_{(i,j) \in \mathcal{E}} \frac{\tau_{ij}}{2} \|t_j - t_i - \hat{t}_{ij}\|_2^2. \quad (9)$$

Note that (9) is a linear least squares problem. Similar to rotation averaging, (9) can be modeled using the undirected measurement graph $G = (\mathcal{V}, \mathcal{E})$, where vertex i represents the translation variable $t_i \in \mathbb{R}^d$ to be estimated, and edge $(i, j) \in \mathcal{E}$ represents the relative translation measurement $\hat{t}_{ij} \in \mathbb{R}^d$. Lastly, $\tau_{ij} > 0$ is the positive weight associated with measurement $(i, j) \in \mathcal{E}$.

C. Communication and Computation Architecture

In this work, we consider solving Problems 1 and 2 under the *server-client* architecture. As shown in Fig. 1a, a central server coordinates with all robots (clients) to solve the overall problem by distributing the underlying computation to the entire team. In practice, the server could itself be a robot (*e.g.*, in multi-robot exploration scenarios) or a remote machine (*e.g.*, in cloud-based AR/VR applications). Each iteration (communication round) consists of an *upload* stage in which robots perform parallel local computations and transmit their intermediate information to the server, and a *download* stage in which the server aggregates information from all robots and broadcasts back the result. When a direct communication link to the server does not exist, a robot can still participate in this framework by relaying its information through other robots. By leveraging local computations, the server-client architecture can scale better compared to a fully centralized approach in which the server solves the entire optimization problem. At the same time, by implementing second-order optimization algorithms, this architecture also produces significantly faster and more accurate solutions compared to fully distributed

approaches that rely on first-order optimization. In the experiments, we demonstrate the scalability and fast convergence of our approach on large SLAM and SfM problems.

D. Applications

Rotation averaging (Problem 1) is a fundamental problem in robotics and computer vision. In distributed camera networks (e.g., [8]), rotation averaging is used to estimate the orientations of spatially distributed cameras with overlapping fields of view. In distributed SfM (e.g., [18]), rotation averaging is a key step to build large-scale 3D reconstructions from many images. Furthermore, in the context of collaborative SLAM, rotation averaging and translation estimation (Problem 2) can be combined to provide accurate *initialization* for PGO [17]. In state-of-the-art PGO solvers, the cost function often has a separable structure between rotation and translation measurements. For example, SE-Sync [60] uses the formulation,

$$\begin{aligned} \underset{\substack{R=(R_1, \dots, R_n) \in \text{SO}(d)^n, \\ t=(t_1, \dots, t_n) \in \mathbb{R}^{d \times n}}}{\text{minimize}} \quad & \sum_{(i,j) \in \mathcal{E}} \kappa_{ij} \left\| R_i \tilde{R}_{ij} - R_j \right\|_F^2 \\ & + \sum_{(i,j) \in \mathcal{E}} \tau_{ij} \left\| t_j - t_i - R_i \tilde{t}_{ij} \right\|_2^2. \end{aligned} \quad (10)$$

In (10), $R_i \in \text{SO}(d)$ and $t_i \in \mathbb{R}^d$ are rotation matrices and translation vectors to be estimated, $\tilde{R}_{ij} \in \text{SO}(d)$ and $\tilde{t}_{ij} \in \mathbb{R}^d$ are noisy relative rotation and translation measurements, and $\kappa_{ij}, \tau_{ij} > 0$ are constant measurement weights. Notice that in (10), the first sum of terms is equivalent to rotation averaging (Problem 1) under the chordal distance. Furthermore, given fixed rotation estimates $\hat{R} \in \text{SO}(d)^n$, the second sum of terms is equivalent to translation estimation (Problem 2) where each \tilde{t}_{ij} in (9) is given by $\tilde{t}_{ij} = \hat{R}_i \tilde{t}_{ij}$. In both cases, the equivalence is up to a multiplying factor of 1/2, but this is inconsequential since it does not change solutions to the optimization problems. Following Carlone *et al.* [17], we use these observations to initialize PGO in a two-stage process. The first stage initializes the rotation variables using the proposed rotation averaging solver (Sec. V-B). Given the initial rotation estimates, the second stage initializes the translations using the proposed translation estimation solver (Sec. V-C). We note that this initialization scheme does not have theoretical guarantees with respect to the full PGO problem. However, we still demonstrate its practical value through our experiments.

IV. LAPLACIAN SYSTEMS ARISING FROM ROTATION AVERAGING AND TRANSLATION ESTIMATION

In this section, we show that for rotation averaging (Problem 1) and translation estimation (Problem 2), their Hessian matrices are closely related to the Laplacians of suitably weighted graphs. The theoretical relations we establish in this section pave the way for designing fast and communication-efficient solvers in Sec. V.

A. Rotation Averaging

To solve rotation averaging (Problem 1), we resort to an iterative Riemannian optimization framework. Before proceeding, however, one needs to be careful of the inherent

gauge-symmetry of rotation averaging: in (7), note that left multiplying each rotation $R_i \in \text{SO}(d), i \in [n]$ by a common rotation $S \in \text{SO}(d)$ does not change the cost function. As a result, each solution $R = (R_1, \dots, R_n) \in \text{SO}(d)^n$ actually corresponds to an *equivalence class* of solutions in the form of,

$$[R] = \{(SR_1, \dots, SR_n), S \in \text{SO}(d)\}. \quad (11)$$

The equivalence relation (11) shows that rotation averaging is actually an optimization problem defined over a *quotient manifold* $\mathcal{M} = \overline{\mathcal{M}} / \sim$, where $\overline{\mathcal{M}} = \text{SO}(d)^n$ is called the total space and \sim denotes the equivalence relation underlying (11); see [26, Chapter 9] for more details. Accounting for the quotient structure is critical for establishing the relation between the Hessian and the graph Laplacian.

In this work, we are interested in applying Newton's method on the quotient manifold \mathcal{M} due to its superior convergence rate. The Newton update can be derived by considering a local perturbation of the cost function. Specifically, let $R = (R_1, \dots, R_n) \in \text{SO}(d)^n$ be our current rotation estimates. For each rotation matrix R_i , we seek a local correction to it in the form of $\text{Exp}(v_i)R_i$, where $v_i \in \mathbb{R}^p$ is some vector to be determined and $\text{Exp}(\cdot)$ is defined in (5). In (7), replacing each R_i with its correction $\text{Exp}(v_i)R_i$ leads to the following local approximation¹ of the optimization problem,

$$\min_{v \in \mathbb{R}^{pn}} h(v; R) \triangleq \sum_{(i,j) \in \mathcal{E}} \kappa_{ij} \varphi(\text{Exp}(v_i)R_i \tilde{R}_{ij}, \text{Exp}(v_j)R_j). \quad (12)$$

In (12), the overall vector $v \in \mathbb{R}^{pn}$ is formed by concatenating all v_i 's. Compared to (7), the optimization variable in (12) becomes the vector v and the rotations R are treated as fixed. Furthermore, we note that the quotient structure of Problem 1 gives rise to the following *vertical space* [26, Chapter 9.4] that summarizes all directions of change along which (12) is invariant,

$$\mathcal{N} = \text{image}(1_n \otimes I_p) \subset \mathbb{R}^{pn}. \quad (13)$$

Intuitively, \mathcal{N} captures the action of any global left rotation. Indeed, for any $v \in \mathcal{N}$, we have $\text{Exp}(v_i) = \text{Exp}(v_j)$ for all $i, j \in [n]$, and thus the cost function (12) remains constant. Let us denote the gradient and Hessian of (12) as follows,

$$\bar{g}(R) \triangleq \nabla h(v; R)|_{v=0}, \quad \bar{H}(R) \triangleq \nabla^2 h(v; R)|_{v=0}. \quad (14)$$

Our notations $\bar{g}(R)$ and $\bar{H}(R)$ serve to emphasize that the gradient and Hessian are defined in the total space $\overline{\mathcal{M}}$ and depend on the current rotation estimates R . Let $\mathcal{H} \triangleq \mathcal{N}^\perp$ denote the *horizontal space*, which is the orthogonal complement of the vertical space \mathcal{N} . In [26, Chapter 9.12], it is shown that executing the Newton update on the quotient manifold amounts to finding the solution $v \in \mathcal{H}$ to the linear system,

$$\underbrace{(P_H \bar{H}(R) P_H)}_{H(R)} v = -\bar{g}(R), \quad (15)$$

¹ The approximation defined in (12) is closely related to the standard *pullback function* in Riemannian optimization; see Appendix II-D. In this work, we use (12) since the resulting Hessian has a particularly interesting relationship with the graph Laplacian matrix, as shown in Theorem 1.

where P_H is the orthogonal projection onto \mathcal{H} . We note that P_H is symmetric, and so is $H(R)$. Furthermore, it holds that $\bar{g}(R) = P_H \bar{g}(R)$, which follows from known results on optimization over quotient manifolds (see Remark 2 for details). Intuitively, including P_H in (15) accounts for the gauge symmetry by eliminating the effect of any vertical component from v . The following theorem reveals an interesting connection between $H(R)$ defined in (15) and the Laplacian of the underlying graph.

Theorem 1 (Local Hessian Approximation for Rotation Averaging). *Let $\underline{R} \in \text{SO}(d)^n$ denote the set of ground truth rotations from which the noisy measurements \tilde{R}_{ij} are generated according to (6). For any $\delta \in (0, 1/2)$, there exist constants $\bar{\theta}, r > 0$ such that if,*

$$\mathbf{d}(\tilde{R}_{ij}, \underline{R}_i^\top \underline{R}_j) \leq \bar{\theta}, \quad \forall (i, j) \in \mathcal{E}, \quad (16)$$

then for all $R \in B_r(R^*) = \{R \in \text{SO}(d)^n : \mathbf{d}(R, R^*) < r\}$ where $R^* \in \text{SO}(d)^n$ is a global minimizer of Problem 1, it holds that,

$$H(R) \approx_\delta L(G; w) \otimes I_p. \quad (17)$$

In (17), $G = (\mathcal{V}, \mathcal{E})$ is the measurement graph, and $p = \dim \text{SO}(d)$. For edge $(i, j) \in \mathcal{E}$, its edge weight w_{ij} is given by $w_{ij} = \kappa_{ij}$ for the squared geodesic distance cost (8a), and $w_{ij} = 2\kappa_{ij}$ for the squared chordal distance cost (8b).

Before proceeding, we note that Theorem 1 directly implies the following bound on the Hessian $H(R)$.

Corollary 1 (Local Hessian Bound and Condition Number for Rotation Averaging). *Under the assumptions of Theorem 1, define constants $\mu_H = e^{-\delta} \lambda_2(L(G; w))$ and $L_H = e^\delta \lambda_n(L(G; w))$. Then for all $R \in B_r(R^*)$,*

$$\mu_H P_H \preceq H(R) \preceq L_H P_H. \quad (18)$$

In the following, $\kappa_H = L_H / \mu_H$ is referred to as the condition number.

We prove Theorem 1 and Corollary 1 in Appendix II. Theorem 1 shows that under small measurement noise, the Hessian near a global minimizer is well approximated by the Laplacian of an appropriately weighted graph.² In Fig. 2, we perform numerical validation of this result using synthetic chordal rotation averaging problems defined over a 3D grid with 125 rotation variables (Fig. 2a). With a probability of 0.3, we generate noisy relative measurements between pairs of nearby rotations, corrupted by increasing levels of Langevin noise [60, Appendix A]. At each noise level, we obtain the global minimizer R^* (global optimality is certified using the approach in [46]) and numerically compute the smallest constant δ such that $H(R^*) \approx_\delta L \otimes I_p$. Fig. 2b shows the evolution of the empirical approximation constant δ as

²Currently, Theorem 1 only shows the existence of constants $\bar{\theta}, r > 0$ such that the approximation relation (17) holds. In a nutshell, this is because our proof is based on the following key relation that holds in the limit: if we define $\theta_{ij}(R) = \mathbf{d}(\tilde{R}_{ij}, \underline{R}_i^\top \underline{R}_j)$ as the measurement residual of edge $(i, j) \in \mathcal{E}$ at a solution $R \in \text{SO}(d)^n$, then we can show that $H(R) \rightarrow L(G; w) \otimes I_p$ as $\theta_{ij}(R) \rightarrow 0$ for all $(i, j) \in \mathcal{E}$; see discussions around (98) in the appendix. While it would be interesting to derive explicit and accurate bounds for $\bar{\theta}$ and r (as a function of δ), this would require a substantial improvement to our current proof technique, which we leave for future work.

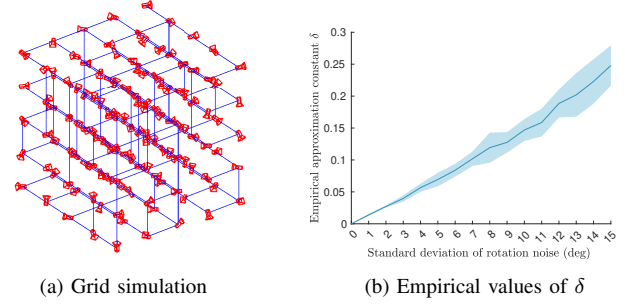


Fig. 2: Empirical validation of the Hessian approximation relation in Theorem 1. (a) Example synthetic chordal rotation averaging problem with 125 rotations. Each rotation is visualized as an oriented camera. Each blue edge shows a relative rotation measurement corrupted by Langevin noise. (b) Evolution of the empirical approximation constant δ such that $H(R^*) \approx_\delta L \otimes I_p$. We perform 20 random runs for each noise level. Solid line denotes the average value for δ and the surrounding shaded area shows one standard deviation.

a function of noise level. In the special case when there is no noise, it can be shown that $H(R^*) = L \otimes I_p$, and thus the empirical δ is zero. In general, the empirical value of δ increases smoothly as the noise level increases. Since the Hessian $H(R)$ varies smoothly with R , our results confirm that the Laplacian is a good approximation of the Hessian locally around R^* , as predicted by Theorem 1.

The result in Theorem 1 directly motivates an *approximate Newton method* that replaces the Hessian with its Laplacian approximation. Specifically, instead of solving (15), one solves the following *approximate Newton* system,

$$(L(G; w) \otimes I_p) v = -\bar{g}(R). \quad (19)$$

In the following, it would be more convenient to consider the matrix form of the above linear system. For this purpose, let us define matrices $V, B(R) \in \mathbb{R}^{n \times p}$,

$$V \triangleq \begin{bmatrix} v_1^\top \\ \vdots \\ v_n^\top \end{bmatrix}, \quad B(R) \triangleq \begin{bmatrix} -\bar{g}_1(R)^\top \\ \vdots \\ -\bar{g}_n(R)^\top \end{bmatrix}. \quad (20)$$

Using properties of the Kronecker product, we can show that (19) is equivalent to,

$$L(G; w)V = B(R). \quad (21)$$

Algorithm 1 shows the pseudocode of the approximate Newton algorithm. Compared to the original Newton's method, Algorithm 1 uses a *constant matrix* across all iterations, and hence could be significantly more computationally efficient by avoiding to re-compute and re-factorize the Hessian matrix at every iteration. For this reason, we believe that Algorithm 1 could be of independent interest for standard (centralized) rotation averaging. Furthermore, in Sec. V, we show that Algorithm 1 admits communication-efficient extensions in multi-robot settings.

Remark 1 (Connections with prior work). Theorem 1 leverages prior theories developed by Tron [50] and Wilson *et al.* [51], [52] and extend them to cover rotation averaging under both geodesic and chordal distance metrics. Nasiri *et al.* [53] first developed Algorithm 1 for chordal

Algorithm 1 APPROXIMATE NEWTON'S METHOD FOR ROTATION AVERAGING

```

1: for iteration  $k = 0, 1, \dots$  do
2:   Compute approximate Newton update by solving
      $L(G; w)V^k = B(R^k)$ .
3:   Update iterate by  $R_i^{k+1} = \text{Exp}(v_i^k)R_i^k$ , for all  $i \in [n]$ .
4: end for
  
```

rotation averaging using a Gauss-Newton formulation. In contrast, we motivate Algorithm 1 by proving the theoretical approximation relation between the Hessian and the graph Laplacian (Theorem 1). Lastly, the theoretical approximation relation we establish also allows us to prove local linear convergence for our methods.

Remark 2 (Feasibility of the approximate Newton system). Using the properties of the graph Laplacian and the Kronecker product, we see that $\ker(L(G; w) \otimes I_p) = \mathcal{N}$ where \mathcal{N} is the vertical space defined in (13). Furthermore, in [26, Chapter 9.8], it is shown that $\bar{g}(R) \perp \mathcal{N}$. Thus, we conclude that $\bar{g}(R) \in \text{image}(L(G; w) \otimes I_p)$, i.e., the linear system (19) and its equivalent matrix form (21) are always feasible. In fact, the system is singular and hence admits infinitely many solutions. Similar to the original Newton's method on quotient manifold, we will select the minimum norm solution v which guarantees that $v \in \mathcal{H}$ [26, Chapter 9.12].

B. Translation Estimation

Unlike rotation averaging, translation estimation (Problem 2) is a convex linear least squares problem. In particular, it can be shown that Problem 2 is equivalent to a linear system involving the graph Laplacian $L(G; \tau)$, where $\tau : \mathcal{E} \rightarrow \mathbb{R}_{>0}$ is the edge weight function that assigns each edge $(i, j) \in \mathcal{E}$ a weight given by the corresponding translation measurement weight τ_{ij} in Problem 2. Denote $M_t = [t_1 \dots t_n]^\top \in \mathbb{R}^{n \times d}$ as the matrix where each row corresponds to a translation vector to be estimated. One can show that the optimal translations are solutions of,

$$L(G; \tau)M_t = B_t, \quad (22)$$

where $B_t \in \mathbb{R}^{n \times d}$ is a constant matrix that only depends on the measurements. Furthermore, each column of B_t belongs to the image of the Laplacian $L(G; \tau)$, so (22) is always feasible; see [60, Appendix B.2] for details. To conclude this section, we note that similar to rotation averaging, translation estimation (Problem 2) is subject to a gauge symmetry. Specifically, two translation solutions M_t and M'_t are equivalent if they only differ by a global translation. Mathematically, this means that $M_t = M'_t + 1_n t_0^\top$ where $1_n \in \mathbb{R}^n$ is the vector of all ones and $t_0 \in \mathbb{R}^d$ is the constant global translation vector.

V. ALGORITHMS AND PERFORMANCE GUARANTEES

In Sec. IV, we have shown that *Laplacian systems* naturally arise when solving the rotation averaging and translation estimation problems; see (21) and (22), respectively. Recall that we seek to find the solution $X \in \mathbb{R}^{n \times p}$ to a linear system of the form,

$$LX = B, \quad (23)$$

where $L \in \mathcal{S}_+^n$ is the Laplacian of the multi-robot measurement graph (see Fig. 1b), and each column of $B \in \mathbb{R}^{n \times p}$ is in the image of L so that (23) is always feasible. For rotation averaging, we have $p = \dim \text{SO}(d)$, and for translation estimation, we have $p = \dim \mathbb{R}^d = d$. In Sec. V-A, we develop a communication-efficient solver for (23) under the server-client architecture described in Sec. III-C. Then, in Sec. V-B and Sec. V-C, we use the developed solver to design communication-efficient algorithms for collaborative rotation averaging and translation estimation, and establish convergence guarantees for both cases. Lastly, in Sec. V-D, we present extension to outlier-robust estimation based on GNC.

A. A Collaborative Laplacian Solver with Spectral Sparsification

We propose to solve (23) using the *domain decomposition* framework [32, Chapter 14], which has been utilized in earlier works such as DDF-SAM [14]–[16] to solve collaborative SLAM problems. This is motivated by the fact that in the multi-robot measurement graph with m robots, there is a natural disjoint partitioning of the vertex set \mathcal{V} :

$$\mathcal{V} = \mathcal{V}_1 \uplus \dots \uplus \mathcal{V}_m, \quad (24)$$

where \mathcal{V}_α contains all vertices (variables) of robot $\alpha \in [m]$ and \uplus denotes the disjoint union. Furthermore, \mathcal{V}_α can be partitioned as $\mathcal{V}_\alpha = \mathcal{F}_\alpha \uplus \mathcal{C}_\alpha$ where \mathcal{C}_α denotes all separator (interface) vertices and \mathcal{F}_α denotes all interior vertices of robot α . In multi-robot SLAM, the separators are given by the set of variables that have inter-robot measurements; see Fig. 1b. Note that given the set of all separators $\mathcal{C} = \mathcal{C}_1 \uplus \dots \uplus \mathcal{C}_m$, robots' interior vertices \mathcal{F}_α become disconnected from each other. The natural vertex partitioning in (24) further gives rise to a disjoint partitioning of the edge set,

$$\mathcal{E} = \mathcal{E}_1 \uplus \dots \uplus \mathcal{E}_m \uplus \mathcal{E}_c. \quad (25)$$

For each robot $\alpha \in [m]$, its local edge set \mathcal{E}_α consists of all edges that connect two vertices from \mathcal{V}_α . In Fig. 1b, the local edges are shown using colors corresponding to the robots. The remaining *inter-robot* edges form \mathcal{E}_c , which are highlighted as bold black edges in Fig. 1b.

In domain decomposition, we adopt a variable ordering in which the interior nodes $\mathcal{F} = \mathcal{F}_1 \uplus \dots \uplus \mathcal{F}_m$ appear before the separators $\mathcal{C} = \mathcal{C}_1 \uplus \dots \uplus \mathcal{C}_m$. With this variable ordering, the Laplacian system (23) can be rewritten as,

$$\begin{bmatrix} L_{11} & & & L_{1c} \\ & \ddots & & \vdots \\ & & L_{mm} & L_{mc} \\ L_{c1} & \dots & L_{cm} & L_{cc} \end{bmatrix} \begin{bmatrix} X_1 \\ \vdots \\ X_m \\ X_c \end{bmatrix} = \begin{bmatrix} B_1 \\ \vdots \\ B_m \\ B_c \end{bmatrix}. \quad (26)$$

For $\alpha \in [m]$, X_α and B_α denote the rows of X and B in (23) that correspond to robot α 's interior variables \mathcal{F}_α . On the other hand, we treat separators *from all robots* as a single block $\mathcal{C} = \mathcal{C}_1 \uplus \dots \uplus \mathcal{C}_m$. In (26), we use the subscript c to index rows and columns of matrices that correspond to \mathcal{C} .

Remark 3 (Computation of (26) under the server-client architecture). Under the server-client architecture we consider, the overall Laplacian system (26) is stored distributedly across the

robots (clients) and the server. Specifically, since each robot α knows the subgraph induced by its own vertices \mathcal{V}_α (e.g., in Fig. 1b, robot 2 knows all edges incident to the blue vertices), it independently computes and stores its Laplacian blocks $L_{\alpha\alpha}$ and $L_{\alpha c}$. Similarly, each robot α also independently computes and stores the block B_α . Meanwhile, we assume that the blocks defined over separators L_{cc} and B_c are handled by the central server that performs additional computations.

In (26), the special “arrowhead” sparsity pattern motivates us to first solve the *reduced system* defined over the separators, obtained by eliminating all interior nodes using the Schur complement [32, Chapter 14.2]:

$$\underbrace{\left(L_{cc} - \sum_{\alpha \in [m]} L_{c\alpha} L_{\alpha\alpha}^{-1} L_{\alpha c} \right)}_{S = \text{Sc}(L, \mathcal{F})} X_c = B_c - \underbrace{\sum_{\alpha \in [m]} L_{c\alpha} L_{\alpha\alpha}^{-1} B_\alpha}_U. \quad (27)$$

In the following, let us define $U_\alpha \triangleq L_{c\alpha} L_{\alpha\alpha}^{-1} B_\alpha$ for each robot $\alpha \in [m]$. Then, the matrix on the right-hand side of (27) can be written as,

$$U \triangleq B_c - \sum_{\alpha \in [m]} U_\alpha. \quad (28)$$

Meanwhile, the matrix S defined on the left-hand side of (27) is the Schur complement resulting from eliminating all interior nodes \mathcal{F} from the full Laplacian matrix L , denoted as $S = \text{Sc}(L, \mathcal{F})$. The next lemma shows S is the sum of multiple smaller Laplacian matrices.

Lemma 1. *For each robot $\alpha \in [m]$, define $G_\alpha = (\mathcal{F}_\alpha \cup \mathcal{C}, \mathcal{E}_\alpha)$ as its local graph induced by its interior edges \mathcal{E}_α . Let S_α be the matrix resulting from eliminating robot α 's interior vertices \mathcal{F}_α from the Laplacian of G_α , i.e., $S_\alpha = \text{Sc}(L(G_\alpha), \mathcal{F}_\alpha)$. Furthermore, define $G_c = (\mathcal{C}, \mathcal{E}_c)$ as the graph induced by inter-robot loop closures \mathcal{E}_c . Then, the matrix S that appears in (27) can be written as,*

$$S = L(G_c) + \sum_{\alpha \in [m]} S_\alpha. \quad (29)$$

Lemma 1 is proved in Appendix III-A. Since Laplacian matrices are closed under Schur complements [23, Fact 4.2], each S_α defined in Lemma 1 is also a Laplacian matrix.³ Furthermore, as a result of Remark 3, each robot α can independently compute $S_\alpha = \text{Sc}(L(G_\alpha), \mathcal{F}_\alpha)$ and $U_\alpha = L_{c\alpha} L_{\alpha\alpha}^{-1} B_\alpha$. This observation motivates a method in which robots first transmit their S_α and U_α to the server in parallel. Upon collecting S_α and U_α from all robots, the server can then form S using (29) and U using (28). It then solves the linear system $SX_c = U$ (27) and broadcasts the solution X_c back to all robots. Finally, once robots receive the separator solutions X_c , they can in parallel recover their interior solutions via back-substitution,

$$X_\alpha = L_{\alpha\alpha}^{-1} (B_\alpha - L_{\alpha c} X_c). \quad (30)$$

³In Lemma 1, we can technically define $G_\alpha = (\mathcal{F}_\alpha \cup \mathcal{C}_\alpha, \mathcal{E}_\alpha)$ since \mathcal{E}_α only involves robot α 's vertices. However, we choose to involve all separators and define $G_\alpha = (\mathcal{F}_\alpha \cup \mathcal{C}, \mathcal{E}_\alpha)$, where any separator from $\mathcal{C} \setminus \mathcal{C}_\alpha$ simply does not have any edges. This is done for notation simplicity, so that after eliminating \mathcal{F}_α from G_α , the resulting S_α matrix is defined over all separators and thus can be added together as in (29).

Algorithm 2 SPARSIFIED SCHUR COMPLEMENT

```

1: function  $\tilde{S} = \text{SPARSIFIEDSCHURCOMPLEMENT}(L, \epsilon)$ 
2:   for each robot  $\alpha$  in parallel do
3:     Compute a sparse approximation  $\tilde{S}_\alpha$  such that  $\tilde{S}_\alpha \approx_\epsilon S_\alpha$ .
4:     Upload  $\tilde{S}_\alpha$  to the server.
5:   end for
6:   Server computes and stores  $\tilde{S} = L(G_c) + \sum_{\alpha \in [m]} \tilde{S}_\alpha$ .
7: end function

```

Algorithm 3 SPARSIFIED LAPLACIAN SOLVER

```

1: function  $X = \text{SPARSIFIEDLAPLACIAN SOLVER}(L, B, \tilde{S})$ 
2:   for each robot  $\alpha$  in parallel do
3:     Compute  $U_\alpha = L_{c\alpha} L_{\alpha\alpha}^{-1} B_\alpha$ .
4:     Upload  $U_\alpha$  to the server.
5:   end for
6:   Server collects  $U_\alpha$  and computes  $U = B_c - \sum_{\alpha \in [m]} U_\alpha$ .
7:   Server solves  $\tilde{S}X_c = U$  (where  $\tilde{S}$  is obtained from Algorithm 2), and broadcasts solution  $X_c$  to all robots.
8:   for each robot  $\alpha$  in parallel do
9:     Compute interior solution  $X_\alpha = L_{\alpha\alpha}^{-1} (B_\alpha - L_{\alpha c} X_c)$ .
10:  end for
11: end function

```

The aforementioned method is a multi-robot implementation of domain decomposition. While it effectively exploits the separable structure in the problem, this method can incur significant communication cost as it requires each robot α to transmit its Schur complement matrix S_α that is potentially dense. This issue is illustrated in Fig. 1c, where for robot 2 (blue) its S_α corresponds to a dense graph over its separators.

In the following, we propose an approximate domain decomposition algorithm that is significantly more communication-efficient while providing *provable approximation guarantees*. Our method is based on the facts that (i) each local Schur complement S_α is itself a graph Laplacian, and (ii) graph Laplacians admit *spectral sparsifications* [19], i.e., for a given approximation threshold $\epsilon > 0$, one can compute a sparse Laplacian \tilde{S}_α such that $\tilde{S}_\alpha \approx_\epsilon S_\alpha$. Generally, a larger value of ϵ leads to a sparser \tilde{S}_α . In this work, we implement the method of Spielman and Srivastava [20] that sparsifies S_α by sampling edges in the corresponding dense graph based on their *effective resistances*. Intuitively, the effective resistances measure the importance of edges to the overall graph connectivity. The sparse matrix \tilde{S}_α produced by this method has $O(|\mathcal{C}| \log |\mathcal{C}|)$ entries, as opposed to the worst case $O(|\mathcal{C}|^2)$ entries in S_α . Appendix I provides the complete description and pseudocode of the sparsification algorithm. Fig. 1d illustrates a spectral sparsification for robot 2's dense reduced graph. In the proposed method, each robot transmits its sparse approximation \tilde{S}_α instead of the original Schur complement S_α . By summing together these \tilde{S}_α matrices, the server can obtain a sparse approximation to the original dense Schur complement S ; see Algorithm 2. Then, we can follow the same procedure as standard domain decomposition to obtain an approximate solution to the Laplacian system (23); see Algorithm 3. Specifically, the server first solves an *approximate* reduced system using \tilde{S} obtained from Algorithm 2 (line 7). Then, the interior solution for each robot is recovered using back-substitution (line 9).

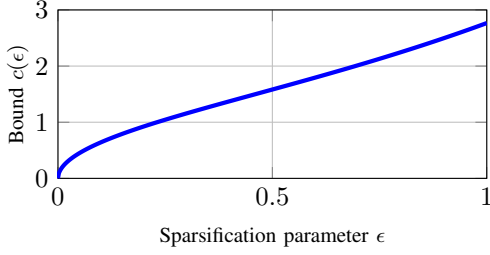


Fig. 3: Visualization of $c(\epsilon)$ in Theorem 2.

Together, Algorithms 2 and 3 provide a parallel procedure for computing an approximate solution to the original Laplacian system (23) in the server-client architecture. Crucially, the use of spectral sparsifiers allows us to establish theoretical guarantees on the accuracy of the approximate solution as stated in the following theorem.

Theorem 2 (Approximation guarantees of Algorithms 2 and 3). *Given a Laplacian system $LX = B$, Algorithms 2 and 3 together return a solution $\tilde{X} \in \mathbb{R}^{n \times p}$ such that $\tilde{L}\tilde{X} = B$, where $\tilde{L} \in \mathcal{S}_+^n$ satisfies,*

$$\tilde{L} \approx_\epsilon L. \quad (31)$$

Furthermore, let $X^* \in \mathbb{R}^{n \times p}$ be an exact solution to the input linear system, i.e., $LX^* = B$. It holds that,

$$\|\tilde{X} - X^*\|_L \leq c(\epsilon) \|X^*\|_L, \quad (32)$$

where the constant $c(\epsilon)$ is defined as,

$$c(\epsilon) = \sqrt{1 + e^{2\epsilon} - 2e^{-\epsilon}}. \quad (33)$$

We prove Theorem 2 in Appendix III-B. We have shown that the approximate solution \tilde{X} produced by Algorithms 2 and 3 remains close to the exact solution X^* when measured using the “norm” induced by the original Laplacian L .⁴ Furthermore, the quality of the approximation is controlled by the sparsification parameter ϵ through the function $c(\epsilon)$ visualized in Fig. 3. Note that when $\epsilon = 0$, sparsification is effectively skipped and robots transmit the original dense matrices S_α . In this case, we have $c(\epsilon) = 0$ and the solution \tilde{X} produced by our methods is exact, i.e., $\tilde{L}\tilde{X} = B$. Meanwhile, by increasing ϵ , our methods smoothly trade off accuracy with communication efficiency.

Remark 4 (Connections with existing Laplacian solvers [23], [24]). Our collaborative Laplacian solver (Algorithms 2 and 3) is inspired by the centralized solvers developed in [23], [24] for solving Laplacian systems in nearly linear time. However, our result differs from these works by focusing on the use of spectral sparsification in the multi-robot setting to achieve communication efficiency. Furthermore, in Sec. V-B, we apply our Laplacian solver on the non-convex Riemannian optimization problem underlying rotation averaging, and establish

⁴The reader might question the use of $\|\cdot\|_L$ in (32) because the Laplacian L is singular. Indeed, due to the singularity of L , $\|X^* - \tilde{X}\|_L$ ignores any component of $X^* - \tilde{X}$ that lives on the kernel of L , which is spanned by the vector of all ones $\mathbf{1}_n$. However, this does not create a problem for us since we only seek to compare X^* and \tilde{X} when considering both as solutions to the Laplacian system $LX = B$, and using $\|\cdot\|_L$ naturally eliminates any difference on $\ker(L)$ that is inconsequential.

provable convergence guarantees for the resulting Riemannian optimization algorithm.

Remark 5 (Communication efficiency of Algorithms 2 and 3). We discuss the communication costs of Algorithms 2 and 3 under the server-client architecture. Denote the number of separators in the measurement graph as $|\mathcal{C}|$. In Algorithm 2, each robot uploads the sparsified matrix \tilde{S}_α to the server (line 4), which is guaranteed to have $O(|\mathcal{C}| \log |\mathcal{C}|)$ entries [20]. Consequently, Algorithm 2 incurs a total *upload* cost of $O(m|\mathcal{C}| \log |\mathcal{C}|)$, where m is the number of robots. In Algorithm 3, robots upload their block vectors U_α in parallel (line 4) and the server broadcasts back the solution X_c (line 7). Since both U_α and X_c have a dimension of $|\mathcal{C}|$ -by- p (where $p = \dim \text{SO}(d)$ is constant), Algorithm 3 uses $O(m|\mathcal{C}|)$ communication in both *upload* and *download* stages.

B. Collaborative Rotation Averaging

In this section, we utilize the Laplacian solver developed in the previous section to design a fast and communication-efficient solver for rotation averaging. Recall the centralized method in Algorithm 1, where each iteration solves a Laplacian system $LV = B(R)$. In the multi-robot setting, we can use the solver developed in Sec. V-A to obtain an approximate solution to this system. Algorithm 4 shows the pseudocode. First, an initial guess R^0 is computed (line 1). Then, at line 2, robots first form the approximate Schur complement \tilde{S} using SPARSIFIEDSCHURCOMPLEMENT (Algorithm 2). Each iteration consists of three main steps. At the first step (line 4-8), robots compute and store the right-hand side $B(R)$. Specifically, recall from Remark 3 that the overall $B(R)$ is divided into multiple blocks,

$$B(R) = [B(R)_1^\top \quad \dots \quad B(R)_m^\top \quad B(R)_c^\top]^\top. \quad (34)$$

In our algorithm, each robot $\alpha \in [m]$ computes the block $B(R)_\alpha$ corresponding to its interior variables \mathcal{F}_α , and the server computes the block $B(R)_c$ corresponding to all separators. At the second step (line 10), robots collaboratively solve for the update vector V^k by calling SPARSIFIEDLAPLACIAN-SOLVER (Algorithm 3). Finally, at the last step (line 11-14), we obtain the next iterate using the solutions V^k , where robots in parallel update the rotation variables they own.

In the following, we proceed to establish theoretical guarantees for our collaborative rotation averaging algorithm. We will show that starting from a suitable initial guess, Algorithm 4 converges to a global minimizer at a *linear* rate. One might be tempted to state the linear convergence result on the total space, i.e., $\mathbf{d}(R^{k+1}, R^*) \leq \gamma \mathbf{d}(R^k, R^*)$ where k is the iteration number, $\gamma \in (0, 1)$ is a constant, and R^* is a global minimizer. However, it is challenging to prove this statement due to the gauge symmetry of rotation averaging. The iterates $\{R^k\}$ might converge to a solution R^∞ that is only equivalent to R^* up to a global rotation, i.e.,

$$(SR_1^\infty, \dots, SR_n^\infty) = (R_1^*, \dots, R_n^*), \text{ for some } S \in \text{SO}(d), \quad (35)$$

and as a result $\mathbf{d}(R^\infty, R^*) \neq 0$ in general. Fortunately, this issue can be resolved using the machinery of Riemannian quotient manifolds. Instead of measuring the distance on the

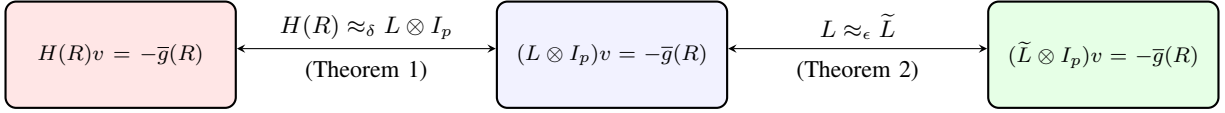


Fig. 4: Intuitions behind the convergence rate in Theorem 3. Recall from Theorem 1 that under bounded measurement noise, the original Newton system (left box) is locally δ -approximated by a linear system specified by a Laplacian L (middle box). In addition, in Theorem 2 we have shown that our distributed Laplacian solver approximates L with \tilde{L} where $L \approx_\epsilon \tilde{L}$ (right box). The composition of the two approximation relations thus gives $H(R) \approx_{\delta+\epsilon} (\tilde{L} \otimes I_p)$, which intuitively explains why (36) depends on a function of $\delta + \epsilon$.

Algorithm 4 COLLABORATIVE ROTATION AVERAGING

```

1: Initialize rotation estimates  $R^0$ .
2:  $\tilde{S} = \text{SPARSIFIEDSCHURCOMPLEMENT}(L, \epsilon)$ .
3: for iteration  $k = 0, 1, \dots$  do
4:   // Distributed computation of  $B(R^k)$ 
5:   Server computes  $B(R^k)_c$  that corresponds to all separators.
6:   for each robot  $\alpha$  in parallel do
7:     Compute  $B(R^k)_\alpha$  that corresponds to interior  $\mathcal{F}_\alpha$ .
8:   end for
9:   // Single round of communication to compute  $V^k$ 
10:  Solve  $V^k = \text{SPARSIFIEDLAPLACIAN SOLVER}(L, B(R^k), \tilde{S})$ .
11:  // Distributed updates of all rotation variables
12:  for each robot  $\alpha$  in parallel do
13:    Update iterates by  $R_i^{k+1} = \text{Exp}(v_i^k)R_i^k$ , for each rota-
      tion variable  $R_i$  owned by robot  $\alpha$ .
14:  end for
15: end for

```

total space $\mathbf{d}(R^k, R^*)$, we will compute the distance between the underlying equivalence classes $\mathbf{d}([R^k], [R^*])$. We note that $\mathbf{d}([R^k], [R^*])$ is well-defined since a quotient manifold inherits the Riemannian metric from its total space [26, Chapter 9]. Equipped with this distance metric, we are ready to formally state the convergence result for Algorithm 4.

Theorem 3 (Convergence rate of Algorithm 4). *Define $\gamma(x) = 2\sqrt{\kappa_H}c(x)$ where $\kappa_H = L_H/\mu_H$ is the condition number in Corollary 1 and $c(\cdot)$ is defined in (33). Under the assumptions of Theorem 1, suppose ϵ is selected such that $\gamma(\delta + \epsilon) < 1$. In addition, suppose at each iteration k , the update vector $v^k \in \mathbb{R}^{pn}$ is orthogonal to the vertical space, i.e., $v^k \perp \mathcal{N}$. Let R^* be an optimal solution to Problem 1. There exists $r' > 0$ such that for any R^0 where $\mathbf{d}([R^0], [R^*]) < r'$, Algorithm 4 generates an infinite sequence $\{R^k\}$ where the corresponding sequence of equivalence classes $[R^k]$ converges linearly to $[R^*]$. Furthermore, the convergence rate factor is,*

$$\limsup_{k \rightarrow \infty} \frac{\mathbf{d}([R^{k+1}], [R^*])}{\mathbf{d}([R^k], [R^*])} = \gamma(\delta + \epsilon). \quad (36)$$

We prove Theorem 3 in Appendix IV-B. Theorem 3 shows that using the distance metric on the quotient manifold, Algorithm 4 locally converges to the global minimizer at a linear rate.⁵ Fig. 4 provides intuitions behind the convergence rate in (36). Recall that δ appears in Theorem 1 where we show $H(R) \approx_\delta (L \otimes I_p)$ under bounded measurement noise. On the other hand, ϵ is the parameter for spectral sparsification

⁵In Theorem 3, the orthogonality assumption $v^k \perp \mathcal{N}$ is needed to ensure that the update vector v^k corresponds to a valid tangent vector on the tangent space of the underlying quotient manifold; see Appendix IV-B for details. One can satisfy this assumption by projecting v^k to the horizontal space, which requires a single round of communication between the server and robots. However, in practice, we find that this has negligible impact on the iterates and thus skip this step in our implementation.

Algorithm 5 COLLABORATIVE TRANSLATION ESTIMATION

```

1: Initialize translation estimates  $M_t^0 = 0_{n \times d}$ .
2:  $\tilde{S} = \text{SPARSIFIEDSCHURCOMPLEMENT}(L, \epsilon)$ .
3: for iteration  $k = 0, 1, \dots$  do
4:   // Distributed computation of  $E^k$ 
5:   Server computes  $E_c^k$  that corresponds to all separators.
6:   for each robot  $\alpha$  in parallel do
7:     Compute  $E_\alpha^k$  that corresponds to interior  $\mathcal{F}_\alpha$ .
8:   end for
9:   // Single round of communication to compute  $D^k$ 
10:  Solve  $D^k = \text{SPARSIFIEDLAPLACIAN SOLVER}(L, E^k, \tilde{S})$ .
11:  // Distributed updates of all translations:  $M_t^{k+1} = M_t^k + D^k$ 
12:  for each robot  $\alpha$  in parallel do
13:    Update iterates by  $t_i^{k+1} = t_i^k + (D_{[i,:]}^k)^\top$  for each
      translation variable  $t_i$  owned by robot  $\alpha$ .
14:  end for
15: end for

```

and is controlled by the user. In Theorem 2, we showed that our methods transform the input Laplacian L into an approximation \tilde{L} such that $L \approx_\epsilon \tilde{L}$. The composition of the two approximation relations thus gives $H(R) \approx_{\delta+\epsilon} (\tilde{L} \otimes I_p)$, which intuitively explains why the convergence rate depends on a function of $\delta + \epsilon$. Lastly, we note that while our theoretical convergence guarantees require $\gamma(\delta + \epsilon) < 1$, our experiments (Sec. VI) show that Algorithm 4 is not sensitive to the choice of ϵ and converges under a wide range of parameter settings.

Remark 6 (Communication efficiency of Algorithm 4). In Algorithm 4, note that only a single call to SPARSIFIEDSCHURCOMPLEMENT (Algorithm 2) is needed, which incurs a total upload of $O(m|\mathcal{C}| \log |\mathcal{C}|)$; see Remark 5. In each iteration, a single call to SPARSIFIEDLAPLACIAN SOLVER (Algorithm 3) is made, which requires a single round of upload and download. Furthermore, by Remark 5, both upload and download costs are bounded by $O(m|\mathcal{C}|)$. Therefore, after $K > 0$ iterations, Algorithm 4 uses a total upload of $O(m|\mathcal{C}| \log |\mathcal{C}| + mK|\mathcal{C}|)$ and a total download of $O(mK|\mathcal{C}|)$. In particular, the terms that involve the number of iterations K scales linearly with the number of separators $|\mathcal{C}|$, which makes the algorithm very communication-efficient.

C. Collaborative Translation Estimation

Similar to rotation averaging, we can develop a fast and communication-efficient method to solve translation estimation, which is equivalent to the Laplacian system (22) as shown in Sec. IV-B. Specifically, we employ our collaborative Laplacian solver (Sec. V-A) in an *iterative refinement* framework. Let $M_t^k \in \mathbb{R}^{n \times d}$ be our estimate for the translation variables at iteration k (in practice M_t^0 can simply be initialized at zero).

We seek a correction D^k to M_t^k by solving the *residual system* corresponding to (22):

$$L(M_t^k + D^k) = B_t \iff LD^k = B_t - LM_t^k \triangleq E^k. \quad (37)$$

Observing that the system on the right-hand side of (37) is another Laplacian system in $L \equiv L(G; \tau)$, we can deploy our Laplacian solver to find an approximate solution D^k . Algorithm 5 shows the pseudocode, which shares many similarities with the proposed collaborative rotation averaging method Algorithm 4. In particular, the computation of the right-hand side E^k (line 4-8) and the update step (line 11-14) are performed in a distributed fashion. The two methods also share the same communication complexity; see Remark 6. The following theorem states the theoretical guarantees for Algorithm 5.

Theorem 4 (Convergence rate of Algorithm 5). *Suppose ϵ is selected such that the constant $c(\epsilon)$ defined in (33) satisfies $c(\epsilon) < 1$. Let M_t^* be an optimal solution to Problem 2 and let M_t^k denote the solution computed by Algorithm 5 at iteration $k \geq 1$. It holds that,*

$$\|M_t^k - M_t^*\|_L \leq c(\epsilon)^k \|M_t^*\|_L, \quad (38)$$

where $L \equiv L(G; \tau)$.

We prove Theorem 4 in Appendix IV-C. Theorem 4 is simpler compared to its counterpart for rotation averaging (Theorem 3). The convergence rate (38) only depends on the sparsification parameter ϵ . Furthermore, since the translation estimation problem is convex, the convergence guarantee is *global* and holds for any initial guess.⁶ While Theorem 4 requires $c(\epsilon) < 1$, our experiments show that Algorithm 5 is not sensitive to the choice of sparsification parameter ϵ and converges under a wide range of parameter settings.

D. Extension to Outlier-Robust Optimization

So far, we have considered estimation using the standard least squares cost function, which is sensitive to *outlier measurements* that might arise in practice (e.g., due to incorrect loop closures in multi-robot SLAM). In this section, we present an extension to *outlier-robust* optimization by embedding the developed solvers in the graduated non-convexity (GNC) framework [21], [22]. We select GNC for its good performance as reported in recent works [6], [21]. However, similar robust optimization frameworks such as iterative reweighted least squares [61] can also be used. Consider robust estimation using the truncated least squares (TLS) cost:⁷

$$\underset{x \in \mathcal{X}}{\text{minimize}} \quad \sum_{(i,j) \in \mathcal{E}} \rho^{\text{TLS}}(e_{ij}(x)). \quad (39)$$

In (39), $x \in \mathcal{X}$ is the model to be estimated, and $e_{ij}(x)$ is the measurement error associated with edge $(i, j) \in \mathcal{E}$ in the measurement graph. For the robust extension of rotation averaging

⁶In (38), the use of $\|\cdot\|_L$ naturally accounts for the global translation symmetry of Problem 2 (see Sec. IV-B). Specifically, since $\ker(L) = \text{image}(\mathbf{1}_n)$, $\|M_t^k - M_t^*\|_L$ disregards any difference between M_t^k and M_t^* that corresponds to a global translation.

⁷Other robust cost functions, such as the Geman McClure function, can also be used in the same framework; see [21].

(Problem 1), we define $x = (R_1, \dots, R_n) \in \text{SO}(d)^n$, and $e_{ij}(x) = \sqrt{\kappa_{ij}/2} \mathbf{d}(R_i \tilde{R}_{ij}, R_j)$ where $\mathbf{d}(\cdot, \cdot)$ is the geodesic or the chordal distance. For the robust extension of translation estimation (Problem 2), we define $x = (t_1, \dots, t_n) \in \mathbb{R}^{d \times n}$ and $e_{ij}(x) = \sqrt{\tau_{ij}/2} \|t_j - t_i - \hat{t}_{ij}\|$. Notice that $e_{ij}(x)$ is simply the square root of a single cost term in Problem 1 or Problem 2. Finally, $\rho^{\text{TLS}}(e) \triangleq \min(e^2, \bar{e}^2)$ denotes the TLS cost function, where \bar{e} is a constant threshold that specifies the maximum acceptable error of inlier measurements. Intuitively, the TLS cost function achieves robustness by eliminating the impact of any outliers with error larger than \bar{e} .

To mitigate the non-convexity introduced by robust cost functions, GNC solves (39) by optimizing a sequence of easier (i.e., less non-convex) surrogate functions ρ_μ^{TLS} that gradually converges to the original, highly non-convex cost function ρ^{TLS} . Here, μ is the control parameter and for the TLS function, it satisfies that (i) ρ_μ^{TLS} is convex for $\mu \rightarrow 0$, and (ii) ρ_μ^{TLS} recovers ρ^{TLS} for $\mu \rightarrow +\infty$; see [21, Example 2]. In practice, we initialize by setting $\mu \approx 0$, and gradually increase μ as optimization progresses. Furthermore, leveraging the Black-Rangarajan duality [22], each surrogate problem can be formulated as follows,

$$\underset{x \in \mathcal{X}, w_{ij}^{\text{GNC}} \in [0,1]}{\text{minimize}} \quad \sum_{(i,j) \in \mathcal{E}} [w_{ij}^{\text{GNC}} e_{ij}^2(x) + \Phi_\mu(w_{ij}^{\text{GNC}})]. \quad (40)$$

In (40), w_{ij}^{GNC} is a mutable weight attached to the measurement error e_{ij} , and Φ_μ acts as a regularization term on the weight whose expression depends on the control parameter μ .

GNC leverages (40) by performing alternating updates on the model x and the weights w_{ij}^{GNC} , while simultaneously updating the control parameter μ . Specifically, each GNC outer iteration consists of three steps:

- 1) **Variable update:** optimize the surrogate problem (40) with respect to x , under fixed weights w_{ij}^{GNC} . Notice that this amounts to a standard weighted least squares problem,

$$\underset{x \in \mathcal{X}}{\text{minimize}} \quad \sum_{(i,j) \in \mathcal{E}} w_{ij}^{\text{GNC}} e_{ij}^2(x). \quad (41)$$

- 2) **Weight update:** optimize the surrogate problem (40) with respect to all w_{ij}^{GNC} , under fixed model x . For TLS, the resulting w_{ij}^{GNC} has a *closed-form* solution,

$$w_{ij}^{\text{GNC}} \leftarrow \begin{cases} 0, & \text{if } e_{ij}^2 \in \left[\frac{\mu+1}{\mu} \bar{e}^2, +\infty \right], \\ \frac{\bar{e}}{e_{ij}} \sqrt{\mu(\mu+1)} - \mu, & \text{if } e_{ij}^2 \in \left[\frac{\mu}{\mu+1} \bar{e}^2, \frac{\mu+1}{\mu} \bar{e}^2 \right], \\ 1, & \text{if } e_{ij}^2 \in \left[0, \frac{\mu}{\mu+1} \bar{e}^2 \right], \end{cases} \quad (42)$$

where $e_{ij} \equiv e_{ij}(x)$ is the current measurement error.

- 3) **Parameter update:** update control parameter μ via $\mu \leftarrow 1.4\mu$ (recommended in [21, Remark 5]), and move on to the next surrogate problem.

Initially, all measurement weights are initialized at one.

Next, we show that our algorithms developed in this work can be used within GNC to perform outlier-robust optimization. Algorithm 6 shows the pseudocode for robust rotation averaging (the case for translation estimation is analogous). The main observation is that, in the context of robust rotation averaging and translation estimation, the weighted least squares problems (41) solved during the **variable update** step have

Algorithm 6 Outlier-robust rotation averaging with GNC

- 1: Initialize control parameter μ and measurement weights by setting $w_{ij} = 1$ for all measurements $(i, j) \in \mathcal{E}$.
 - 2: **while** not converged **do**
 - 3: **Variable update:** under fixed weights, solve the weighted rotation averaging problem by executing Algorithm 4 under the server-client architecture.
 - 4: **Weight update:** in parallel, server computes (42) for all inter-robot measurements \mathcal{E}_c , and each robot α computes (42) for its local measurements \mathcal{E}_α .
 - 5: **Parameter update:** in parallel, server and all robots updates the control parameter μ .
 - 6: **end while**
-

identical forms as Problems 1 and 2. The only difference is that each measurement is now discounted by the GNC weight w_{ij}^{GNC} , as shown in (41). Therefore, we can use Algorithm 4 to perform the variable update for rotation averaging (line 3), and Algorithm 5 for translation estimation. Furthermore, the **weight update** step can also be executed under the server-client architecture, where each robot α computes (42) for its local measurements \mathcal{E}_α , and the server handles the inter-robot measurements \mathcal{E}_c ; see line 4. Lastly, the server and all robots can in parallel perform the **parameter update** step by updating their local copies of the control parameter μ (line 5).

Remark 7 (Implementation details of GNC). We discuss several implementation details for GNC.

- *Initialization.* Prior works (e.g., [6]) have observed that using an outlier-free initial guess when solving the variable update step is critical to ensure good performance. For multi-robot SLAM, we adopt the method described in [6, Section V-B] that aligns each robot’s odometry in the global reference frame by solving a robust single pose averaging problem. Notably, this method does not require iterative communication and hence is very efficient.
- *Known inliers.* In many cases, a subset of measurements $\mathcal{E}_{\text{in}} \subseteq \mathcal{E}$ are known to be inliers. For instance, \mathcal{E}_{in} may contain robots’ odometry measurements. In our implementation, we use the standard least squares cost for \mathcal{E}_{in} and only apply GNC on the remaining measurements.
- *Approximate optimization.* Recall that each outer iteration of GNC invokes Algorithm 4 or Algorithm 5 to perform the variable update step. Thus, when the number of outer iterations is large, the resulting optimization might become expensive in terms of both runtime and communication. However, in practice, we observe that GNC only requires a few outer iterations before the resulting estimates stabilize (see Sec. VI-C). This suggests that instead of running GNC to full convergence (i.e., fully classifying each measurement as either inlier or outlier), we can perform approximate optimization by limiting the number of outer iterations while still achieving robust estimation. In our experiments, we set the maximum number of GNC outer iterations to 20.

We conclude this subsection by noting that the linear convergence results (Theorems 3 and 4) we prove in this paper only hold for the outlier-free case. Extending the linear convergence to the case with outliers is challenging because GNC (and the

similar method of iterative reweighted least square) is itself a heuristic. Nevertheless, our experiments demonstrate that in practice, the proposed outlier-robust extension is very effective and produces accurate solutions on real-world SLAM and SfM problems contaminated by outlier measurements.

VI. EXPERIMENTAL RESULTS

In this section, we extensively evaluate our proposed methods and demonstrate their fast convergence and communication efficiency. In addition, we show that the combination of our rotation estimation and translation estimation algorithms can be used for accurate PGO initialization. Secs. VI-A and VI-B show evaluations using synthetic and benchmark datasets. Then, Sec. VI-C and Sec. VI-D demonstrate *outlier-robust* estimation using our approach on real-world collaborative SLAM and SfM problems. Lastly, Sec. VI-E provides additional discussions on the performance of our approach in real-world problem instances. All proposed algorithms (including the GNC extension in Sec. V-D) are implemented in MATLAB. Some experiments use GTSAM [62] and the Theia SfM library [63] for comparison, where we run their original implementations in C++. All experiments are performed on a computer with an Intel i7-7700K CPU and 16 GB RAM, and communication is simulated in memory in MATLAB.

Performance Metrics. In the experiments, we use the following metrics to evaluate algorithm performance. First, we compute the evolution of *gradient norm* that measures the rate of convergence. Second, to quantify communication efficiency, we record the *total communication* used by an algorithm. For the server-client architecture, communication is reported for both the *upload* and *download* stages. When evaluating the proposed PGO initialization method, we also compute the relative *optimality gap* in the cost function, defined as $(f_{\text{init}} - f_{\text{opt}})/f_{\text{opt}}$, where f_{init} and f_{opt} denote the cost achieved by our initialization and the global minimizer, respectively. Lastly, we also report the *solution distance* to the global minimizer and optionally to the ground truth (the latter is only available in our synthetic experiments). Specifically, for rotation estimation, we compute the distance between our solution $\hat{R} \in \text{SO}(d)^n$ and the reference $R^{\text{ref}} \in \text{SO}(d)^n$ (either global minimizer or ground truth) using the orbit distance:

$$\text{RMSE}(\hat{R}, R^{\text{ref}}) \triangleq \min_{S \in \text{SO}(d)} \sqrt{\frac{1}{n} \sum_{i=1}^n \|S \hat{R}_i - R_i^{\text{ref}}\|_F^2}. \quad (43)$$

Intuitively, (43) computes the root-mean-square error (RMSE) between two sets of rotations after alignment by a global rotation. The optimal alignment S in (43) has a closed-form expression; see [60, Appendix C.1]. Similarly, for translations, we report the RMSE between our solution and the reference after a global alignment.

A. Evaluation of Estimation Accuracy and Communication Efficiency

In this section, we evaluate the estimation accuracy and communication efficiency of the proposed methods under varying problem setups and algorithm parameters. Unless otherwise mentioned, we initialize Algorithm 4 using the

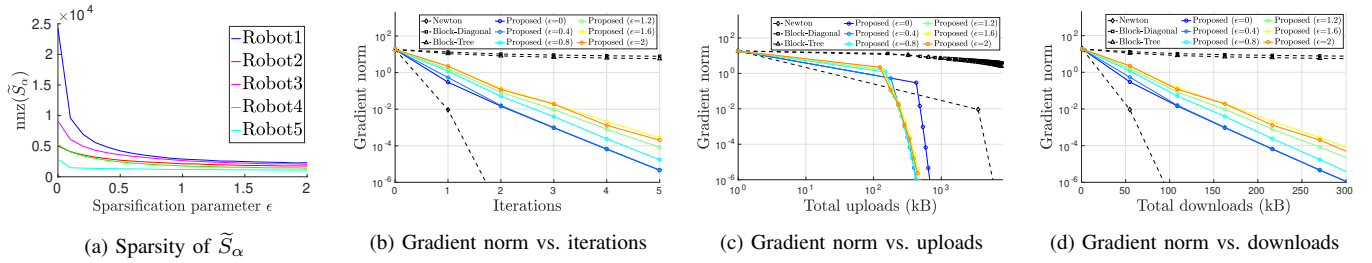


Fig. 5: Evaluation of Algorithm 4 on the 5-robot rotation averaging problem from the Cubicle dataset. (a) For each robot α , we show the number of nonzero entries (nnz) in its sparsified matrix \tilde{S}_α as a function sparsification parameter ϵ . (b) Evolution of Riemannian gradient norm as a function of iterations. (c) Evolution of Riemannian gradient norm as a function of total uploads. (d) Evolution of Riemannian gradient norm as a function of total downloads.

distributed chordal initialization approach in [9], where the number of iterations is limited to 50. Our experiments mainly consider rotation averaging problems under the chordal distance metric. Appendix VI provides additional results using the geodesic distance.

Impact of Spectral Sparsification on Convergence and Communication. First, we evaluate the impact of spectral sparsification on convergence rate and communication efficiency. We start by evaluating the proposed collaborative rotation averaging solver (Algorithm 4), by simulating a 5-robot problem using the Cubicle dataset. In Appendix VI, we present similar analysis for translation estimation. Recall that Algorithm 4 calls the SPARSIFIEDSCHURCOMPLEMENT procedure (Algorithm 2), which requires each robot α to transmit its sparsified matrix \tilde{S}_α . Fig. 5a shows the number of nonzero entries in \tilde{S}_α as a function of the sparsification parameter ϵ . Note that when $\epsilon = 0$, sparsification is effectively skipped and each robot transmits its exact S_α matrix that is potentially large and dense. In Fig. 5a, this is reflected on robot 1 (blue curve) whose exact S_α matrix has more than 2×10^4 nonzero entries and hence is expensive to transmit. However, spectral sparsification significantly reduces the density of the matrix and hence improves communication efficiency. In particular, for robot 1, applying sparsification with $\epsilon = 2$ creates a sparse \tilde{S}_α with 2300 nonzero entries, which is much sparser than the original S_α .

Next, we evaluate the convergence rate and communication efficiency of Algorithm 4 with varying sparsification parameter ϵ . We introduce three baseline methods for the purpose of comparison. The first baseline, called Newton in Fig. 5, implements the exact Newton update using domain decomposition, where each robot communicates its exact (dense) Schur complement similar to DDF-SAM [14]. In addition, we also implement two baselines that apply heuristic sparsification to Newton: in Block-Diagonal, each robot only transmits the diagonal blocks of its Schur complement, whereas in Block-Tree, each robot transmits both diagonal blocks and off-diagonal blocks that form a tree sparsity pattern. These two baselines are similar to the Jacobi and tree preconditioning [36], as well as the approximate summarization strategy in DDF-SAM 2.0 [16]. Fig. 5b shows the accuracy achieved by all methods (measured by norm of the Riemannian gradient) as a function of iterations. As expected, Newton achieves the best convergence speed and converges to a high-precision solution in two iterations. However, when combined with heuristic sparsifications in Block-Diagonal and Block-Tree, the resulting

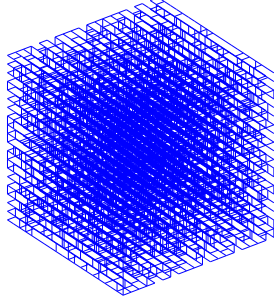
methods have very slow convergence. Intuitively, this result shows that a diagonal or tree sparsity pattern is not sufficient for preserving the spectrum of the original dense matrix.⁸ In contrast, our proposed method achieves fast convergence under a wide range of sparsification parameter ϵ . Furthermore, by varying ϵ , the proposed method provides a principled way to trade off convergence speed with communication efficiency.

Fig. 5c visualizes the accuracy as a function of total uploads to the server. Since both the Hessian and Laplacian matrices are symmetric, we only record the communication when uploading their upper triangular parts as sparse matrices. To convert the result to kilobyte (kB), we assume each scalar is transmitted in double precision. Our results show that the proposed method achieves the best communication efficiency under various settings of the sparsification parameter ϵ . Moreover, even without sparsification (i.e., $\epsilon = 0$), the proposed method is still more communication-efficient than Newton. This result is due to the following reasons. First, since the Hessian matrix varies across iterations, Newton requires communication of the updated Hessian Schur complements at every iteration. In contrast, the proposed method works with a *constant* graph Laplacian, and hence only requires a one-time communication of its Schur complements; see line 2 in Algorithm 4. Second, Newton requires communication to form the Schur complement of the original pn -by- pn Hessian matrix, where n is the number of rotation variables and $p = \dim \text{SO}(d)$ is the intrinsic dimension of the rotation group (for the Cubicle dataset, $n = 5750$ and $p = 3$). In contrast, the proposed method operates on the smaller n -by- n Laplacian matrix, and the decrease in matrix size directly translates to communication reduction.

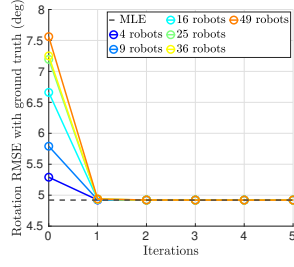
Lastly, Fig. 5d visualizes the accuracy as a function of total communication in the download stage. Notice that the evolution follows the same trend as Fig. 5b, where the horizontal axis shows the number of iterations. This observation is expected as a result of Remark 6, which shows that the communication complexity in the download stage is $O(mK|\mathcal{C}|)$, i.e., the total downloads grows *linearly* with respect to the number of iterations K .

Scalability with Number of Robots. In this experiment, we evaluate the scalability of Algorithm 4. For this purpose, we generate a large-scale synthetic rotation averaging problem with 8000 rotations arranged in a 3D grid (Fig. 6a). With

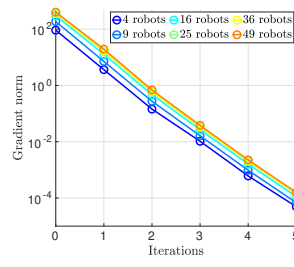
⁸In centralized optimization (e.g., [33]–[36]), these heuristic sparsifications often serve as preconditioners and need to be used within iterative methods such as conjugate gradient to provide the best performance.



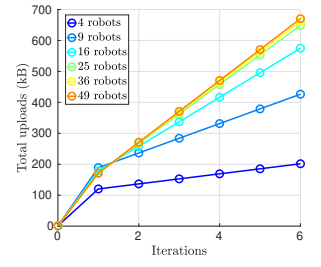
(a) Synthetic rotation averaging



(b) RMSE vs. iterations

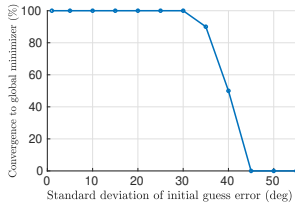


(c) Gradient norm vs. iterations

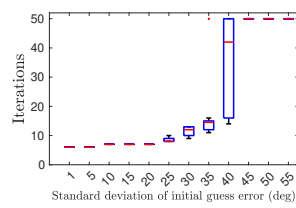


(d) Uploads vs. iterations

Fig. 6: Scalability of Algorithm 4 as the number of robots increases. (a) Synthetic chordal rotation averaging problem with 8000 total rotation variables arranged in a 3D grid. Each edge indicates a relative rotation measurement corrupted by Langevin noise. (b) Evolution of RMSE (in degree) with respect to ground truth rotations. (c) Evolution of Riemannian gradient norm as a function of iterations. (d) Evolution of total uploads as a function of iterations.

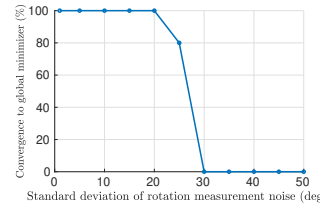


(a) Success rate

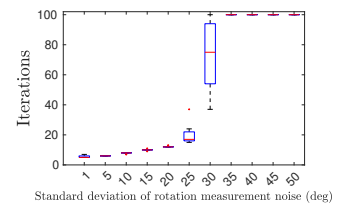


(b) Number of iterations

Fig. 7: Sensitivity of Algorithm 4 to accuracy of initial guess. We generate synthetic initial guesses with degrading accuracy by perturbing the global minimizer with increasing levels of Langevin noise. At each level of perturbation, 10 random runs are performed. (a) Percentage of runs that converge to the global minimizer. (b) Boxplot of number of iterations used by Algorithm 4.



(a) Success rate



(b) Number of iterations

Fig. 8: Sensitivity of Algorithm 4 to rotation measurement noise. We generate synthetic chordal rotation averaging problems with increasing magnitude of measurement noise. At each noise level, 10 random runs are performed. (a) Percentage of runs that converge to the global minimizer. (b) Boxplot of number of iterations used by Algorithm 4.

probability 0.3, we add relative measurements between nearby rotations, which are corrupted by Langevin noise with a standard deviation of 5 deg. Then, we divide the dataset to simulate increasing number of robots, and run Algorithm 4 with sparsification parameter $\epsilon = 0.5$ until the Riemannian gradient norm reaches 10^{-5} . Fig. 6b shows the evolution of the estimation RMSE with respect to the ground truth rotations. For reference, we also show the RMSE achieved by the global minimizer to Problem 1 (denoted as “MLE” in the figure). Note that due to measurement noise, the MLE is in general different from the ground truth. The proposed method is able to achieve an RMSE similar to the MLE after a single iteration, despite the worse initialization as the number of robots increases. Fig. 6c shows the evolution of gradient norm as a function of iterations. Note that all curves in Fig. 6c have similar slopes, which suggests that the empirical convergence rate of our method is not sensitive to the number of robots. This observation is compatible with the (local) convergence rate established in Theorem 3, which does not depend on the number of robots m . This property makes our method more appealing than existing fully distributed methods, whose convergence speed typically degrades as the number of robots increases (e.g., see [10, Fig. 8]). Lastly, Fig. 6d shows the evolution of total uploads as a function of iterations. As we divide the dataset to simulate more robots, both the number of inter-robot measurements and the number of separators $|\mathcal{C}|$ increase, and thus each iteration requires more communication.

Sensitivity to Initial Guess. So far, we have used the

distributed chordal initialization technique [9] to initialize Algorithm 4. In the next experiment, we test the sensitivity of our proposed method to poor initial guesses. For this purpose, we use a 9-robot simulation where each robot owns 512 rotation variables, and generate synthetic initial guesses by perturbing the global minimizer with increasing level of Langevin noise. Using the synthetic initialization, we run Algorithm 4 with sparsification parameter $\epsilon = 0.5$ until the Riemannian gradient norm reaches 10^{-5} or the number of iterations exceeds 50. At each noise level, 10 random runs are performed. Fig. 7a shows the fraction of trials that successfully converge to the global minimizer. We observe that Algorithm 4 enjoys a large convergence basin: the success rate only begins to decrease at a large initial guess error of 35 deg. Fig. 7b shows the number of iterations used by Algorithm 4 to reach convergence. Our results suggest that the proposed method is not sensitive to the quality of initialization and usually requires a small number of iterations to converge.

Sensitivity to Measurement Noise. Next, we analyze the sensitivity of Algorithm 4 to increasing levels of measurement noise. The setup is similar to the previous experiment, where we use a 9-robot simulation and each robot owns 512 rotations. However, instead of varying the quality of the initial guess, we vary the noise level when generating the synthetic problem. Fig. 8 shows the results. We find that Algorithm 4 is relatively more sensitive to the measurement noise, and start to converge to suboptimal local minima as the noise level increases above 25 deg. Nevertheless, we note that the level of rotation noise

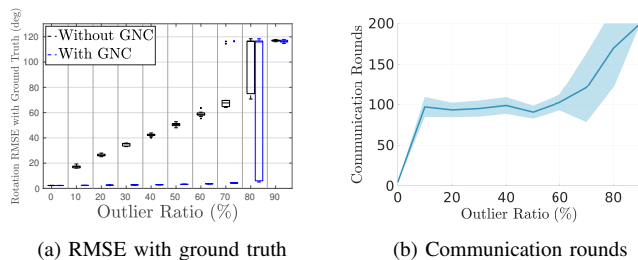


Fig. 9: Evaluation of robust optimization on synthetic rotation averaging problems corrupted by increasing percentage of outlier loop closures. At each outlier percentage, 10 random runs are performed. (a) RMSE with respect to ground truth rotations. (b) Communication rounds used by GNC. Solid line and shaded area correspond to the mean and one standard deviation, respectively.

encountered in practice is usually much lower,⁹ and thus we expect our algorithm to still provide effective estimation (see real-world evaluations in Secs. VI-C and VI-D).

Outlier-Robust Optimization. Lastly, we evaluate the proposed outlier-robust optimization method to solve robust rotation averaging problems. In this experiment, we use a 9-robot simulation where each robot owns 512 rotations. In Secs. VI-C and VI-D, we demonstrate our method on real-world SLAM and SfM problems. As in common SLAM scenarios, we assume each robot has a backbone of odometry measurements within its own trajectory that are free of outliers. Then, with increasing probability, we replace the remaining measurements (corresponding to intra-robot and inter-robot loop closures) with gross outliers. All inlier measurements (including odometry) are corrupted by Langevin noise with a standard deviation of 3 deg, and we set the TLS threshold \bar{e} to correspond to 10 deg. Fig. 9a visualizes the RMSE with respect to ground truth rotations. As expected, Algorithm 4 without GNC is not robust to outliers and shows significant error as soon as outlier measurements are introduced. Nevertheless, by using Algorithm 4 within GNC as described in Sec. V-D, the resulting approach becomes robust and is able to tolerate up to 70% of outlier loop closures. In Fig. 9b, we study the efficiency of our approach by showing the total number of inner iterations of Algorithm 4 used by GNC. Recall that each inner iteration also corresponds to a single round of communication. When the outlier ratio is zero, GNC reduces to the standard Algorithm 4 and only requires a few iterations to converge. When outliers are added, GNC requires multiple outer iterations and thus multiple calls to Algorithm 4, resulting in increased communication rounds. Nevertheless, for all test cases with less than 70% outlier measurements, the number of communication rounds is approximately 100, which is a reasonable requirement for a real system.

B. Evaluation on Benchmark PGO Datasets

In this subsection, we evaluate our approach on 12 benchmark pose graph SLAM datasets. For these datasets, we do not explicitly handle outliers. Outlier-robust estimation will be evaluated in Secs. VI-C and VI-D.

⁹Here we only consider rotation noise of *inlier* measurements. *Outlier* measurements will be handled using the robust optimization framework presented in Sec. V-D.

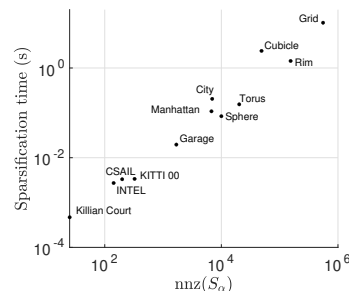


Fig. 10: Spectral sparsification runtime on benchmark datasets.

Evaluation on Rotation Averaging Subproblem. We first evaluate Algorithm 4 on the rotation averaging subproblems extracted from the benchmark datasets. For each problem, we simulate a scenario with 5 robots, and run the proposed method (Algorithm 4) with sparsification parameter $\epsilon = 1.5$ and the baseline Newton method. Both methods are terminated when the Riemannian gradient norm is smaller than 10^{-5} . Since the spectral sparsification method we use [20] is randomized, we perform 5 random runs of our method. Table I shows the average number of iterations, uploads, and downloads to reach the desired precision. On all datasets, we are able to verify that all methods converge to the global minima of the considered rotation averaging problems. The proposed method achieves an empirical convergence speed that is close to Newton and typically converges in a few iterations.¹⁰ We note that this is significantly faster than existing fully distributed methods (e.g., [10], [12]) that often require hundreds of iterations to achieve moderate precision. For both Newton and the proposed method, the total download is proportional to the number of iterations (see Remark 6). Thus, our method uses more downloads since it requires more iterations. However, we note that compared to the download stage, the upload stage is more communication-intensive since robots need to transmit (potentially dense) Schur complements to the server. Using spectral sparsification, the proposed approach achieves significant reduction in uploads, especially on challenging datasets such as Grid and Rim. Finally, the last column of Table I shows the achieved sparsification as the percentage of nonzero elements that remain after spectral sparsification. We observe that the benefit of sparsification varies across datasets. For example, on Killian Court and INTEL, the effect of sparsification is limited because the exact Schur complement S is already sparse. Meanwhile, on datasets such as Grid and Rim, the benefit of sparsification is substantial and the results have less than 10% nonzero elements. In Sec. VI-E, we provide a thorough discussion on the impact of problem properties on sparsification performance.

Sparsification Runtime. Recall that in the SPARSIFIED-SCHURCOMPLEMENT step in Algorithm 4, each robot α sparsifies its S_α matrix and transmits the result \tilde{S}_α to the server. This step uses the majority of robots' local computation

¹⁰One notable exception is the *Rim* dataset, for which our method uses more than 20 iterations to converge. A closer investigation reveals that this dataset actually contains some outlier measurements. Specifically, at the global minimizer R^* , there are 28 measurements \tilde{R}_{ij} for which $d(R_i^* \tilde{R}_{ij}, R_j^*) > 60$ deg. Since these outliers have large residuals, their contributions to the Hessian can no longer be well approximated by the corresponding Laplacian terms. As a result, the performance of our method is negatively impacted.

TABLE I: Rotation averaging on benchmark SLAM datasets with 5 robots. $|\mathcal{V}|$ and $|\mathcal{E}|$ denote the total number of rotation variables and measurements, respectively. We run the baseline **Newton** method and the proposed method (Algorithm 4) with sparsification parameter $\epsilon = 1.5$, and compare the number of iterations, uploads, and downloads to reach a Riemannian gradient norm of 10^{-5} . For the proposed method, we also show the sparsity achieved by sparsification (lower is better). Results averaged across 5 runs.

Dataset	$ \mathcal{V} $	$ \mathcal{E} $	Iterations		Upload (kB)		Download (kB)		Achieved sparsity by proposed (%)
			Newton	Proposed	Newton	Proposed	Newton	Proposed	
Killian Court (2D)	808	827	2	3	1.6	1.1	0.5	0.8	100
CSAIL (2D)	1045	1171	2	4	7.2	5.9	2.3	4.6	97.3
INTEL (2D)	1228	1483	3	4.2	10.5	5.8	3.3	4.6	96.4
Manhattan (2D)	3500	5453	2	5	118.9	49.5	12.5	31.3	38.7
KITTI 00 (2D)	4541	4676	2	2	13.2	6.6	4.4	4.4	100
City (2D)	10000	20687	2	4	450.3	351.5	129	258.1	97.3
Garage (3D)	1661	6275	1	2	274.4	88.9	35.8	71.6	93.2
Sphere (3D)	2500	4949	2	8.6	2548.8	106	19.2	82.6	16.9
Torus (3D)	5000	9048	3	9.6	10423.7	229.5	57	182.2	12.4
Grid (3D)	8000	22236	3	9.2	206871.6	886.6	220.8	677	2.7
Cubicle (3D)	5750	16869	2	6.8	7015	440.3	107.7	366.2	19.9
Rim (3D)	10195	29743	4	23.4	53657.9	1320.9	209.1	1223.2	6.6

time. In Fig. 10, we evaluate the runtime of the sparsification algorithm [20] on the 12 benchmark datasets shown in Table I. For each dataset, we record the maximum sparsification time among all robots, and visualize the result as a function of the number of nonzero entries in the input matrix S_α . On most datasets, the maximum runtime is below one second. On the Grid dataset, the input matrix has more than 5×10^5 nonzero entries and our implementation uses 10.2 seconds. Overall, we conclude that the runtime of our implementation is still reasonable. However, we believe that further improvements are possible, *e.g.*, by approximately computing effective resistances during spectral sparsification as suggested in [20].

Initialization for PGO. Lastly, we evaluate the use of our methods to initialize PGO. Recall from Sec. III-D that our initialization scheme involves two stages. First, we initialize rotations by solving the rotation averaging subproblem in PGO. In particular, we run Algorithm 4 using an initial guess computed from a spanning tree of the pose graph. This also demonstrates that our method does not need to rely on distributed chordal initialization [9], which is itself an iterative procedure. Then, fixing the rotation estimates in PGO, we initialize translations by solving the resulting translation estimation subproblem using Algorithm 5, where Algorithm 5 is simply initialized at zero. Table II reports the optimality gap and estimation RMSE of our initialization method compared to the optimal PGO solutions computed using SE-Sync [60]. Our results show that the quality of initialization varies across datasets. In general, since our initialization method decouples the estimation of rotations and translations, we expect its performance to degrade when there is significant coupling between rotation and translation terms in the full PGO problem. To investigate this hypothesis, we treat PGO as an inference problem over factor graphs [7] and consider the covariance Σ^{PGO} of the pose estimates at the optimal solution. We compare Σ^{PGO} with the corresponding covariance Σ^{INIT} produced by our two-stage initialization, where the rotation and translation blocks of Σ^{INIT} are extracted from rotation averaging and translation estimation, respectively. Since both covariance matrices are large and dense, we only compute their

diagonal blocks Σ_i^{PGO} and Σ_i^{INIT} that correspond to the marginal covariances of pose i . We quantify the error introduced by decoupled rotation and translation estimation by computing the normalized error $e_i^\Sigma = \|\Sigma_i^{\text{PGO}} - \Sigma_i^{\text{INIT}}\|_F / \|\Sigma_i^{\text{PGO}}\|_F$. Table II reports e^Σ , which is the average of e_i^Σ over all poses. We find that the results separate all datasets into two groups. INTEL, CSAIL, Torus, and Grid have small values of e^Σ , and our initialization achieves the best performance, especially in terms of optimality gap. On the remaining datasets with larger values of e^Σ , the two-stage initialization produces worse results. Lastly, we note that Rim is a special case due to the presence of outlier measurements.

In addition, Table II also reports the number of iterations and total communication (both uploads and downloads) used by our initialization during rotation estimation and translation estimation. To provide additional context, we report corresponding results for the state-of-the-art RBCD++ solver [10] to achieve the same optimality gap. We start RBCD++ using an initial guess computed by aligning trajectory estimates obtained from robots' local PGO; see Appendix VI for details. We note that the RBCD++ results are only included for reference since this method is fully distributed whereas our method assumes a server-client architecture. Furthermore, given more iterations, RBCD++ will eventually achieve better accuracy because the method is solving the full PGO problem. However, our results still suggest that when a server-client architecture is available, our method is favorable and provides high-quality initialization using only a few iterations.

C. Robust PGO Initialization for Real-World Collaborative SLAM

In this section, we show that our approach can be used to achieve *robust* PGO initialization in a real-world collaborative SLAM scenario with outlier measurements. For this purpose, we collected three sets of trajectories using a Clearpath Jackal robot equipped with a front-facing RealSense D455 RGBD camera and IMU. Each trajectory covers a different area outside a building on the MIT campus, with the robot making multiple loops within the designated area. The three trajec-

TABLE II: PGO initialization on benchmark SLAM datasets with 5 robots. e^Σ measures the average error in marginal covariance due to decoupled rotation and translation estimation. Optimality gap and RMSE are computed with respect to optimal solutions from SE-Sync [60]. In addition, we also show the number of iterations and communication (both upload and download) used by the rotation and translation estimation stages in our approach, and compare the results with RBCD++ [10] to achieve the same optimality gap.

Dataset	$ \mathcal{V} $	$ \mathcal{E} $	e^Σ	Optimality Gap	RMSE with optimal PGO solution		Iterations			Total communication (kB)		
					Rotation (deg)	Translation (m)	Rot.	Tran.	RBCD++	Rot.	Tran.	RBCD++
Killian Court (2D)	808	827	0.76	0.12	4.48	4.12	5	2	141	3.0	2.4	202
CSAIL (2D)	1045	1171	0.33	4.6×10^{-4}	0.06	0.01	3	3	367	8.3	15.2	1.9×10^3
INTEL (2D)	1228	1483	0.21	2.2×10^{-3}	0.36	0.03	4	4	109	10.0	18.7	589
Manhattan (2D)	3500	5453	0.92	0.15	1.75	0.47	4	5	42	72.8	147.8	982
KITTI 00 (2D)	4541	4676	0.86	0.33	0.46	0.64	3	2	1000	15.4	19.8	1.1×10^4
City (2D)	10000	20687	0.95	0.12	0.63	0.18	4	4	44	611	1.1×10^3	8.4×10^3
Garage (3D)	1661	6275	0.99	0.12	0.43	0.33	2	2	66	161	162	4.0×10^3
Sphere (3D)	2500	4949	0.87	0.17	1.39	0.38	7	7	1	185	185	32
Torus (3D)	5000	9048	0.25	0.01	2.15	0.07	8	6	7	394	317	305
Grid (3D)	8000	22236	0.43	0.03	1.22	0.06	8	8	5	1.7×10^3	1.7×10^3	1.2×10^3
Cubicle (3D)	5750	16869	0.86	0.18	1.53	0.16	7	6	101	869	722	9.3×10^3
Rim (3D)	10195	29743	0.79	0.63	4.95	0.78	25	6	179	2.8×10^3	748	1.3×10^4

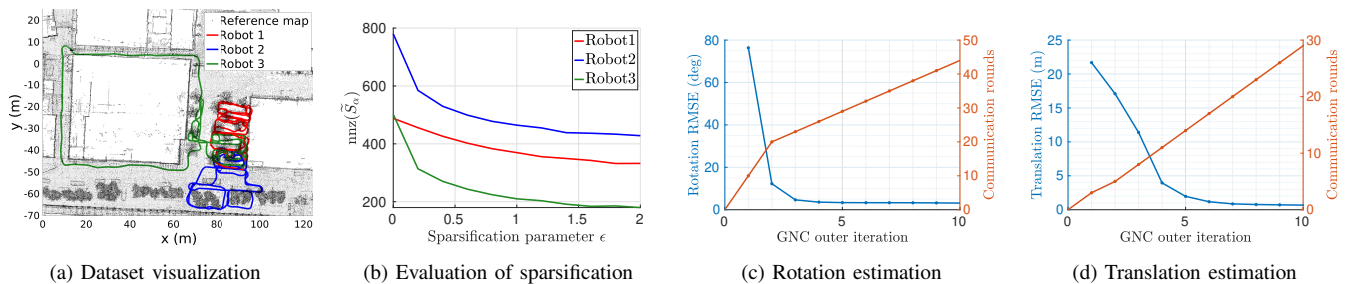


Fig. 11: Robust PGO initialization on real-world collaborative SLAM dataset. (a) Trajectory estimates produced by the proposed robust PGO initialization, which are qualitatively overlaid on top of a point cloud map of the experiment area. The point cloud map was created at an earlier time (certain objects such as cars have changed) and is included only for visualization. (b) Evaluation of spectral sparsification. (c) Rotation RMSE as a function of communication rounds during rotation estimation. (d) Translation RMSE as a function of communication rounds during translation estimation.

ries also overlap in a small region such that common features are observed (Fig. 11a). We run Kimera-Multi [6] to process the dataset as a 3-robot collaborative visual SLAM mission. The resulting multi-robot pose graph contains a 3D pose variable for each keyframe generated by visual-inertial odometry, and each robot has a backbone of odometry measurements that are free of outliers. However, there are many outlier loop closures (both within each robot’s trajectory and between different robots), due to incorrect visual feature matching.

We demonstrate the two-stage PGO initialization as described in Sec. III-D. To account for outliers, we use the GNC-based robust optimization during both rotation estimation and translation estimation stages. In our experiment, we observe that setting the TLS threshold to a smaller value of 0.5 deg for rotation estimation leads to better performance. The TLS threshold for translation estimation is set to 0.25 m. With this setting, the two-stage initialization rejects 1090 out of 1540 loop closures (71%). In Appendix VI, we provide additional evaluation on the sensitivity to the TLS thresholds. Table III reports statistics and the accuracy achieved by our robust initialization for each robot. As ground truth trajectories are not available, we compare against a reference solution computed by the GNC-based robust PGO solver implemented in GTSAM [62]. While standard initialization (without GNC) has large errors, using GNC achieves robust initialization, and the final rotation and translation RMSE over all robots are 3.0 deg and 0.57 m, respectively. Fig. 11b evaluates the effects of spectral sparsification on the real-world dataset. We observe

TABLE III: Evaluation of robust PGO initialization on real-world collaborative SLAM dataset.

Robot	Length (m)	Keyframes	RMSE without GNC		RMSE with GNC	
			Rot. (deg)	Tran. (m)	Rot. (deg)	Tran. (m)
1	483	3192	67.5	11.9	1.8	0.5
2	458	2518	73.1	17.6	3.3	0.7
3	524	3374	86.8	23.6	3.7	0.6

similar benefits as in previous experiments, where enabling sparsification ($\epsilon > 0$) significantly reduces the number of nonzero entries each robot needs to communicate. Lastly, Figs. 11c and 11d evaluate the efficiency of our two-stage robust initialization, by visualizing the evolution of RMSE and number of communication rounds as a function of GNC outer iterations. Recall that each communication round also corresponds to a single iteration of Algorithm 4 or Algorithm 5. For this experiment, the sparsification parameter is fixed at $\epsilon = 2$. Overall, for both rotation estimation and translation estimation, the RMSE converges after a few GNC outer iterations, and consequently, only a small number of communication rounds is needed.

D. Evaluation on Real-World Structure-from-Motion Datasets

Lastly, we evaluate our method on rotation averaging problems extracted from 15 real-world structure-from-motion (SfM) datasets [64]. Each dataset is a collection of many internet images taken at a particular location. We use Theia [63] to process each dataset and extract a rotation averaging problem with outliers (caused by incorrect feature matching). As

TABLE IV: Robust rotation averaging on real-world SfM datasets. Each dataset is divided to simulate 5 robots. $|\mathcal{V}|$ and $|\mathcal{E}|$ denote the total number of rotation variables and measurements, respectively. Using the reference solution, we quantify the difficulty of each dataset by computing the percentage of high-quality inlier measurements (measurement error < 5 deg) and gross outliers (measurement error > 45 deg). For the proposed method, we show the sparsity achieved by sparsification (lower is better) and total communication.

DATASETS	$ \mathcal{V} $	$ \mathcal{E} $	Measurement Quality (%)			Mean Error (deg)				Achieved sparsity (%)	Communication (MB)	
			Inlier	Outlier	Other	Initial	No GNC	With GNC	Theia		Download	Upload
Montreal Notre Dame	468	49705	81	4	15	4.2	3.3	1.1	1.1	55.1	2.09	1.21
Ellis Island	241	19507	63	1	26	7.0	5.6	2.3	2.4	66.0	0.95	0.57
NYC Library	355	17579	61	6	33	4.3	4.3	2.3	2.5	75.8	1.24	0.83
Notre Dame	553	97764	70	9	21	3.5	4.5	2.4	2.6	41.8	2.85	1.54
Roman Forum	1099	53989	74	3	23	16.5	5.1	2.5	2.5	68.1	4.43	2.73
Alamo	606	87725	74	3	23	8.0	4.5	2.9	2.8	44.7	2.62	1.39
Madrid Metropolis	379	18811	47	20	33	7.7	8.0	3.4	3.4	70.3	1.48	1.08
Yorkminster	448	24416	73	5	22	8.3	4.5	3.4	3.3	76.5	1.69	1.1
Tower of London	493	19798	76	3	21	7.4	4.7	3.5	3.4	75.3	2.00	1.35
Trafalgar	5433	680012	63	7	30	20.0	6.4	3.5	3.3	40.7	35.89	24.97
Piazza del Popolo	343	22342	82	4	14	5.4	7.8	3.6	3.5	70.0	1.29	0.8
Piccadilly	2436	254175	58	10	32	13.9	14.6	4.9	5.0	53.1	14.23	9.79
Union Square	930	25561	57	6	37	11.9	10.9	6.0	8.6	82.1	4.15	3.37
Vienna Cathedral	900	96546	70	6	24	13.9	9.6	8.9	8.6	51.9	4.62	3.13
Gendarmenmarkt	723	42980	36	27	37	45.0	40.8	38.1	38.1	63.8	4.13	3.03

ground truth is not available, we follow [63] and use 3D reconstructions produced by the incremental SfM pipeline [65] as reference solutions. Table IV reports full dataset statistics.

Based on the image IDs, we equally partition each dataset to simulate 5 robots and run our GNC-based rotation averaging solver, with the TLS threshold set to 5 deg. Compared to collaborative SLAM, in SfM there is a significantly larger number of inter-robot measurements. Furthermore, each robot no longer has an outlier-free odometry backbone in SfM. This means that we cannot use the approach of [6] to compute an outlier-free initial guess for the variable update step in GNC (see Remark 7). Instead, we use the initial guess from Theia that is computed using a spanning tree of the measurement graph. Table IV reports the mean estimation error. On 14 out of the 15 datasets, our GNC-based method produces accurate results with performance on par with the centralized Theia library. The only failure case, Gendarmenmarkt, is known to be a very challenging case in which the underlying 3D scene is highly symmetric, leading to a significantly lower percentage of inlier measurements. The initial guess has a large error, which both GNC and Theia are unable to recover from. This issue could potentially be addressed with a better initialization method (*e.g.*, using pairwise consistency maximization [66]), which we leave for future work. In summary, we conclude that on most datasets, our proposed rotation averaging solver combined with GNC is able to achieve robust rotation estimation, despite outlier measurements and the increased noise level present in internet images.

We report the performance of spectral sparsification and the total communication costs of our method. For our SfM experiment, we increase the sparsification parameter to $\epsilon = 5$. In Sec. VI-E, we explain the reasons behind using the increased value for ϵ . Table IV shows the achieved sparsity as the average ratio between the number of nonzero elements in the sparsified matrix and the input (dense) matrix. On all datasets, spectral sparsification significantly improves sparsity to as low as 40.7% on the largest Trafalgar dataset. These results,

together with the total amounts of uploads and downloads, demonstrate the effectiveness of our approach to achieve communication efficiency.

E. Discussion

We conclude our experimental evaluations by discussing the impacts of real-world problem properties on the performance of the proposed algorithms.

Effectiveness of Laplacian Approximation in the Presence of Outliers. Our rotation averaging method exploits the fact that under small measurement residuals, the Laplacian is an effective approximation of the Hessian (Theorem 1). When there are outlier measurements, we have seen that the approximation quality degrades, leading to increased number of iterations. An example is the Rim dataset in Table I, which is contaminated by outliers. Nonetheless, we note that this issue is mitigated when using a robust optimization framework such as GNC, since outliers will be gradually discounted and eventually rejected from the measurement graph. This is shown in Fig. 11c. During the first two GNC outer iterations, outliers have a substantial influence on the problem, causing our method (Algorithm 4) to use more communication rounds. However, as GNC proceeds, outliers receive increasingly small weights, and our method recovers its fast convergence. In Fig. 11c, this is shown as the slower increase in communication rounds starting from the third GNC outer iteration.

Impact of Problem Density on Sparsification Performance. As we have seen (*e.g.*, from Table I), spectral sparsification achieves different levels of sparsity improvement on the various SLAM and SfM datasets. This is because in our method, sparsification is applied to the Schur complements that the robots form after eliminating their interior variables (see Algorithm 2). Thus, we expect the performance of sparsification to vary depending on the density of the Schur complements. To make the discussion more concrete, we identify three types of problems and Fig. 12 shows a representative

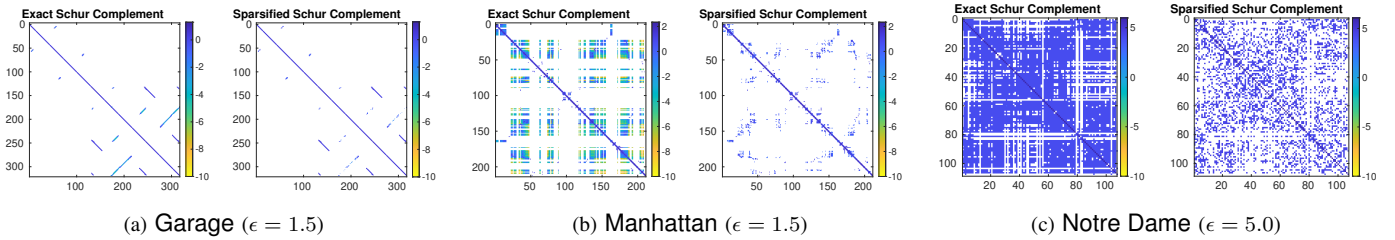


Fig. 12: Impact of the density of exact Schur complements on the performance of spectral sparsification. For each dataset, we select one robot and visualize the sparsity pattern of its exact Schur complement (corresponding to S_α in Algorithm 2), and the result after spectral sparsification (corresponding to \tilde{S}_α in Algorithm 2). Entries in the matrix are color-coded based on their magnitude in log scale.

sparsification result for each case. In the first case (Fig. 12a), the multi-robot measurement graph is extremely sparse; consequently, the resulting Schur complements are already sparse and sparsification is not necessary. In the second case, the original measurement graph is still sparse, but the robots' Schur complements become dense due to *fill-in* introduced during the elimination of interior variables. For the example in Fig. 12b, the fill-in is visualized as patches of dense entries in the exact Schur complement, and our method is highly effective at sparsifying these dense blocks. Moreover, notice that the dense fill-ins have relatively smaller magnitudes (e.g., compared to the diagonal), and thus they can be sparsified with a smaller value of the sparsification parameter ϵ . In the last case, the original measurement graph is already dense and so are the resulting Schur complements (Fig. 12c). All of the SfM datasets in Table IV belong to this category because there are many images viewing a common landmark (e.g., the Notre Dame cathedral), albeit from different locations or angles. Consequently, a relative rotation can be estimated for many image pairs, which makes the input measurement graph dense. Since there is no significant difference in the magnitudes of different matrix entries, a larger value of ϵ is needed. Similar to the second case, sparsification is highly effective at promoting sparsity in each robot's transmitted matrix in this case.

VII. CONCLUSION

We presented fast and communication-efficient methods for solving rotation averaging and translation estimation in multi-robot SLAM, SfM, and camera network localization applications. Our algorithms leverage theoretical relations between the Hessians of the optimization problems and the Laplacians of the underlying graphs. At each iteration, robots coordinate with a central server to perform approximate second-order optimization, while using spectral sparsification to achieve communication efficiency. We performed rigorous analysis of our methods and proved that they achieve (local) linear rate of convergence. Furthermore, we proposed the combination of our solvers with GNC to achieve outlier-robust estimation. Extensive experiments in real-world collaborative SLAM and SfM scenarios validate our theoretical results and demonstrate the superior convergence rate and communication efficiency of our proposed methods.

While results are promising, this work also suggests several directions for future research. First, it remains an open problem whether a similar approach can be developed for the full PGO problem. Our preliminary analysis shows that, unlike rotation averaging, the Hessian of PGO is no longer well approximated

by the corresponding graph Laplacian due to the coupling between rotation and translation terms. As a result, our current approach cannot be directly applied and additional techniques need to be considered. Secondly, the proposed algorithms assume the availability of communication links that allow all robots to participate in collaborative optimization. When some robots go offline, a practical remedy is to temporarily exclude them from optimization, but this could lead to decrease in the overall accuracy. A principled extension to cope with communication failures and evaluations under more realistic scenarios (e.g., using real-world communication protocols) would be valuable. Lastly, extending the algorithm to leverage the incremental nature of real-world SLAM problems is another interesting direction for future research.

REFERENCES

- [1] Patrik Schmuck, Thomas Ziegler, Marco Karrer, Jonathan Perraudin, and Margarita Chli. COVINS: Visual-Inertial SLAM for Centralized Collaboration. In *IEEE International Symposium on Mixed and Augmented Reality Adjunct*, 2021.
- [2] Yun Chang, Kamak Ebadi, Christopher E Denniston, Muhammad Fadhil Ginting, Antoni Rosinol, Andrzej Reinke, Matteo Palieri, Jingnan Shi, Arghya Chatterjee, Benjamin Morrell, et al. LAMP 2.0: A robust multi-robot SLAM system for operation in challenging large-scale underground environments. *IEEE Robotics and Automation Letters*, 2022.
- [3] Andrei Cramariuc, Lukas Bernreiter, Florian Tschoep, Marius Fehr, Victor Reijgwart, Juan Nieto, Roland Siegwart, and Cesar Cadena. MAPLAB 2.0-A Modular and Multi-Modal Mapping Framework. *IEEE Robotics and Automation Letters*, 8(2):520–527, 2022.
- [4] Titus Cieslewski, Siddharth Choudhary, and Davide Scaramuzza. Data-Efficient Decentralized Visual SLAM. In *IEEE Intl. Conf. on Robotics and Automation (ICRA)*, pages 2466–2473, 2018.
- [5] Pierre-Yves Lajoie, Benjamin Ramtoula, Yun Chang, Luca Carlone, and Giovanni Beltrame. DOOR-SLAM: Distributed, Online, and Outlier Resilient SLAM for Robotic Teams. *IEEE Robotics and Automation Letters*, 2020.
- [6] Yulun Tian, Yun Chang, Fernando Herrera Arias, Carlos Nieto-Granda, Jonathan P How, and Luca Carlone. Kimera-multi: Robust, distributed, dense metric-semantic slam for multi-robot systems. *IEEE Trans. Robotics*, 38(4), 2022.
- [7] Frank Dellaert, Michael Kaess, et al. Factor graphs for robot perception. *Foundations and Trends® in Robotics*, 6(1-2):1–139, 2017.
- [8] Roberto Tron and Rene Vidal. Distributed 3-D Localization of Camera Sensor Networks From 2-D Image Measurements. *IEEE Trans. on Automatic Control*, 59(12):3325–3340, Dec 2014.
- [9] Siddharth Choudhary, Luca Carlone, Carlos Nieto, John Rogers, Henrik I Christensen, and Frank Dellaert. Distributed mapping with privacy and communication constraints: Lightweight algorithms and object-based models. *Intl. J. of Robotics Research*, 2017.
- [10] Yulun Tian, Kasra Khosoussi, David M Rosen, and Jonathan P How. Distributed certifiably correct pose-graph optimization. *IEEE Trans. Robotics*, 37(6):2137–2156, 2021.
- [11] Yulun Tian, Alec Koppel, Amrit Singh Bedi, and Jonathan P How. Asynchronous and Parallel Distributed Pose Graph Optimization. *IEEE Robotics and Automation Letters*, 5(4):5819–5826, 2020.

- [12] Taosha Fan and Todd Murphey. Majorization Minimization Methods for Distributed Pose Graph Optimization. *arXiv preprint arXiv:2108.00083*, 2021.
- [13] Riku Murai, Joseph Ortiz, Sajad Saeedi, Paul HJ Kelly, and Andrew J Davison. A robot web for distributed many-device localisation. *arXiv preprint arXiv:2202.03314*, 2022.
- [14] Alexander Cunningham, Manohar Paluri, and Frank Dellaert. DDF-SAM: Fully distributed SLAM using Constrained Factor Graphs. In *IEEE/RSJ Intl. Conf. on Intelligent Robots and Systems (IROS)*, 2010.
- [15] Alexander Cunningham, Kai M. Wurm, Wolfram Burgard, and Frank Dellaert. Fully distributed scalable smoothing and mapping with robust multi-robot data association. In *IEEE Intl. Conf. on Robotics and Automation (ICRA)*, 2012.
- [16] Alexander Cunningham, Vadim Indelman, and Frank Dellaert. DDF-SAM 2.0: Consistent distributed smoothing and mapping. In *IEEE Intl. Conf. on Robotics and Automation (ICRA)*, 2013.
- [17] Luca Carlone, Roberto Tron, Kostas Daniilidis, and Frank Dellaert. Initialization techniques for 3D SLAM: A survey on rotation estimation and its use in pose graph optimization. In *IEEE Intl. Conf. on Robotics and Automation (ICRA)*, May 2015.
- [18] Siyu Zhu, Runze Zhang, Lei Zhou, Tianwei Shen, Tian Fang, Ping Tan, and Long Quan. Very Large-Scale Global SfM by Distributed Motion Averaging. In *IEEE Conf. on Computer Vision and Pattern Recognition (CVPR)*, June 2018.
- [19] Joshua Batson, Daniel A Spielman, Nikhil Srivastava, and Shang-Hua Teng. Spectral sparsification of graphs: theory and algorithms. *Communications of the ACM*, 56(8):87–94, 2013.
- [20] Daniel A. Spielman and Nikhil Srivastava. Graph Sparsification by Effective Resistances. *SIAM Journal on Computing*, 2011.
- [21] Heng Yang, Pasquale Antonante, Vasileios Tzoumas, and Luca Carlone. Graduated Non-Convexity for Robust Spatial Perception: From Non-Minimal Solvers to Global Outlier Rejection. *IEEE Robotics and Automation Letters*, 5(2):1127–1134, 2020.
- [22] Michael J Black and Anand Rangarajan. On the unification of line processes, outlier rejection, and robust statistics with applications in early vision. *Intl. J. of Computer Vision*, 1996.
- [23] Yin Tat Lee, Richard Peng, and Daniel A Spielman. Sparsified cholesky solvers for SDD linear systems. *arXiv preprint arXiv:1506.08204*, 2015.
- [24] Rasmus Kyng, Yin Tat Lee, Richard Peng, Sushant Sachdeva, and Daniel A Spielman. Sparsified cholesky and multigrid solvers for connection laplacians. In *Proceedings of the forty-eighth annual ACM symposium on Theory of Computing*, pages 842–850, 2016.
- [25] P-A Absil, Robert Mahony, and Rodolphe Sepulchre. *Optimization algorithms on matrix manifolds*. Princeton University Press, 2009.
- [26] Nicolas Boumal. An introduction to optimization on smooth manifolds, 2020.
- [27] Yulun Tian, Amrit Singh Bedi, Alec Koppel, Miguel Calvo-Fullana, David M Rosen, and Jonathan P How. Distributed riemannian optimization with lazy communication for collaborative geometric estimation. In *IEEE/RSJ Intl. Conf. on Intelligent Robots and Systems (IROS)*, pages 4391–4398. IEEE, 2022.
- [28] Henrik Kretschmar and Cyrill Stachniss. Information-theoretic compression of pose graphs for laser-based SLAM. *Intl. J. of Robotics Research*, 31(11):1219–1230, 2012.
- [29] Nicholas Carlevaris-Bianco, Michael Kaess, and Ryan M Eustice. Generic node removal for factor-graph SLAM. *IEEE Trans. Robotics*, 30(6):1371–1385, 2014.
- [30] Mladen Mazuran, Gian Diego Tipaldi, Luciano Spinello, and Wolfram Burgard. Nonlinear Graph Sparsification for SLAM. In *Robotics: Science and Systems (RSS)*, pages 1–8, 2014.
- [31] Liam Paull, Guoquan Huang, Mae Seto, and John J. Leonard. Communication-constrained multi-AUV cooperative SLAM. In *IEEE Intl. Conf. on Robotics and Automation (ICRA)*, 2015.
- [32] Yousef Saad. *Iterative methods for sparse linear systems*. SIAM, 2003.
- [33] Sameer Agarwal, Noah Snavely, Steven M. Seitz, and Richard Szeliski. Bundle Adjustment in the Large. In Kostas Daniilidis, Petros Maragos, and Nikos Paragios, editors, *European Conf. on Computer Vision (ECCV)*, pages 29–42, Berlin, Heidelberg, 2010. Springer Berlin Heidelberg.
- [34] Frank Dellaert, Justin Carlson, Viorela Ila, Kai Ni, and Charles E. Thorpe. Subgraph-preconditioned conjugate gradients for large scale SLAM. In *IEEE/RSJ Intl. Conf. on Intelligent Robots and Systems (IROS)*, pages 2566–2571, 2010.
- [35] Changchang Wu, Sameer Agarwal, Brian Curless, and Steven M. Seitz. Multicore bundle adjustment. In *IEEE Conf. on Computer Vision and Pattern Recognition (CVPR)*, pages 3057–3064, 2011.
- [36] Avanish Kushal and Sameer Agarwal. Visibility Based Preconditioning for bundle adjustment. In *IEEE Conf. on Computer Vision and Pattern Recognition (CVPR)*, pages 1442–1449, 2012.
- [37] Yetong Zhang, Ming Hsiao, Jing Dong, Jakob Engel, and Frank Dellaert. MR-iSAM2: Incremental Smoothing and Mapping with Multi-Root Bayes Tree for Multi-Robot SLAM. In *IEEE/RSJ Intl. Conf. on Intelligent Robots and Systems (IROS)*, pages 8671–8678, 2021.
- [38] Pierre-Yves Lajoie, Benjamin Ramtoulou, Fang Wu, and Giovanni Beltrame. Towards collaborative simultaneous localization and mapping: a survey of the current research landscape. *Field Robotics*, 2021.
- [39] Gonzalo Mateos, Juan Andrés Bazerque, and Georgios B. Giannakis. Distributed Sparse Linear Regression. *IEEE Transactions on Signal Processing*, 58(10):5262–5276, 2010.
- [40] Wei Shi, Qing Ling, Gang Wu, and Wotao Yin. Extra: An exact first-order algorithm for decentralized consensus optimization. *SIAM Journal on Optimization*, 25(2):944–966, 2015.
- [41] Angelia Nedic, Alex Olshevsky, and Wei Shi. Achieving geometric convergence for distributed optimization over time-varying graphs. *SIAM Journal on Optimization*, 27(4):2597–2633, 2017.
- [42] Paolo Di Lorenzo and Gesualdo Scutari. Next: In-network nonconvex optimization. *IEEE Transactions on Signal and Information Processing over Networks*, 2(2):120–136, 2016.
- [43] Nicolas Boumal, Amit Singer, P-A Absil, and Vincent D Blondel. Cramér–Rao bounds for synchronization of rotations. *Information and Inference: A Journal of the IMA*, pages 1–39, 2014.
- [44] Kasra Khosoussi, Matthew Giamou, Gaurav S Sukhatme, Shoudong Huang, Gamini Dissanayake, and Jonathan P How. Reliable graphs for SLAM. *Intl. J. of Robotics Research*, 2019.
- [45] Yongbo Chen, Shoudong Huang, Liang Zhao, and Gamini Dissanayake. Cramér–Rao bounds and optimal design metrics for pose-graph SLAM. *IEEE Trans. Robotics*, 2021.
- [46] Anders P. Eriksson, Carl Olsson, Fredrik Kahl, and Tat-Jun Chin. Rotation Averaging and Strong Duality. In *IEEE Conf. on Computer Vision and Pattern Recognition (CVPR)*, 2018.
- [47] Lukas Bernreiter, Shehryar Khattak, Lionel Ott, Roland Siegwart, Marco Hutter, and Cesar Cadena. Collaborative Robot Mapping using Spectral Graph Analysis. *arXiv preprint arXiv:2203.00308*, 2022.
- [48] Kevin J Doherty, David M Rosen, and John J Leonard. Spectral Measurement Sparsification for Pose-Graph SLAM. *arXiv preprint arXiv:2203.13897*, 2022.
- [49] Luca Carlone. A convergence analysis for pose graph optimization via Gauss-Newton methods. In *IEEE Intl. Conf. on Robotics and Automation (ICRA)*, pages 965–972, 2013.
- [50] Roberto Tron. *Distributed optimization on manifolds for consensus algorithms and camera network localization*. The Johns Hopkins University, 2012.
- [51] Kyle Wilson, David Bindel, and Noah Snavely. When is rotations averaging hard? In *European Conf. on Computer Vision (ECCV)*, 2016.
- [52] Kyle Wilson and David Bindel. On the distribution of minima in intrinsic-metric rotation averaging. In *IEEE Conf. on Computer Vision and Pattern Recognition (CVPR)*, 2020.
- [53] Seyed-Mahdi Nasiri, Reshad Hosseini, and Hadi Moradi. Novel Parameterization for Gauss-Newton Methods in 3-D Pose Graph Optimization. *IEEE Trans. Robotics*, 37(3):780–797, 2021.
- [54] Joshua D Batson, Daniel A Spielman, and Nikhil Srivastava. Twicetramanujan sparsifiers. In *Proceedings of the forty-first annual ACM symposium on Theory of computing*, pages 255–262, 2009.
- [55] Rasmus Kyng and Sushant Sachdeva. Approximate gaussian elimination for laplacians-fast, sparse, and simple. In *IEEE 57th Annual Symposium on Foundations of Computer Science (FOCS)*. IEEE, 2016.
- [56] David Durfee, Rasmus Kyng, John Peebles, Anup B Rao, and Sushant Sachdeva. Sampling random spanning trees faster than matrix multiplication. In *Proceedings of the 49th Annual ACM SIGACT Symposium on Theory of Computing*, pages 730–742, 2017.
- [57] Nisheeth K Vishnoi. $Lx=b$ Laplacian Solvers and their Algorithmic Applications. *Foundations and Trends in Theoretical Computer Science*, 2013.
- [58] Richard Peng and Daniel A Spielman. An efficient parallel solver for SDD linear systems. In *Proceedings of the forty-sixth annual ACM symposium on Theory of computing*, pages 333–342, 2014.
- [59] Rasul Tutunov, Haitham Bou-Ammar, and Ali Jadbabaie. Distributed Newton Method for Large-Scale Consensus Optimization. *IEEE Trans. on Automatic Control*, 64(10):3983–3994, 2019.
- [60] David M Rosen, Luca Carlone, Afonso S Bandeira, and John J Leonard. SE-Sync: A certifiably correct algorithm for synchronization over the special Euclidean group. *Intl. J. of Robotics Research*, 38(2-3):95–125, 2019.

- [61] Avishek Chatterjee and Venu Madhav Govindu. Robust Relative Rotation Averaging. *IEEE Trans. Pattern Anal. Machine Intell.*, 40(4):958–972, 2018.
- [62] Frank Dellaert et al. Georgia Tech Smoothing And Mapping (GTSAM). <https://gtsam.org/>, 2019.
- [63] Chris Sweeney. Theia Multiview Geometry Library: Tutorial & Reference. <http://theia-sfm.org>.
- [64] Kyle Wilson and Noah Snavely. Robust Global Translations with IDSfM. In *European Conf. on Computer Vision (ECCV)*, 2014.
- [65] Noah Snavely, Steven M. Seitz, and Richard Szeliski. Photo tourism: exploring photo collections in 3D. *ACM Trans. Graph.*, 2006.
- [66] Joshua G. Mangelson, Derrick Dominic, Ryan M. Eustice, and Ram Vasudevan. Pairwise Consistent Measurement Set Maximization for Robust Multi-robot Map Merging. In *IEEE Intl. Conf. on Robotics and Automation (ICRA)*, pages 1–8, Brisbane, Australia, May 2018.
- [67] Daniel A Spielman. Spectral and Algebraic Graph Theory. <http://cs-www.cs.yale.edu/homes/spielman/sagt/sagt.pdf>, 2019.
- [68] Richard Hartley, Jochen Trumpf, Yuchao Dai, and Hongdong Li. Rotation Averaging. *Intl. J. of Computer Vision*, 2013.
- [69] Roger A Horn and Charles R Johnson. *Matrix analysis*. Cambridge university press, 2012.

TABLE V: Summary of key notations used in this work (organized by sections).

Notation	Description	Reference
Section III		
$G = (\mathcal{V}, \mathcal{E})$	Multi-robot measurement graph with vertex (variable) set \mathcal{V} and edge (measurement) set \mathcal{E}	
R_i	The i th rotation variable to be estimated in rotation averaging	(7)
\tilde{R}_{ij}	Noisy relative rotation measurement in rotation averaging	(7)
$\varphi(\cdot, \cdot)$	Squared geodesic or chordal distance function between two rotations	(8a)-(8b)
t_i	The i th translation variable to be estimated in translation estimation	(9)
\tilde{t}_{ij}	Noisy relative translation measurement in translation estimation	(9)
\hat{t}_{ij}	Noisy relative translation measurement in PGO	(10)
κ_{ij}	Weight (precision) associated with the relative rotation measurement between vertex i and j	(7), (10)
τ_{ij}	Weight (precision) associated with the relative translation measurement between vertex i and j	(9), (10)
Section IV		
p	$p \triangleq \dim \text{SO}(d)$ is the intrinsic dimension of the rotation group $\text{SO}(d)$	
$[R]$	The equivalent class corresponding to n rotations $R = (R_1, \dots, R_n) \in \text{SO}(d)^n$	(11)
v_i	$v_i \in \mathbb{R}^p$ is the correction vector (to be optimized) for rotation variable R_i	
v	$v \in \mathbb{R}^{pn}$ is formed by concatenating the v_i vectors of all n rotation variables	(12)
V	$V \in \mathbb{R}^{n \times p}$ is the matrix representation of v	(20)
\mathcal{N}, \mathcal{H}	Subspaces of \mathbb{R}^{pn} corresponding to the vertical space and horizontal space in rotation averaging ($\mathcal{H} \triangleq \mathcal{V}^\perp$)	(13)
P_H	Orthogonal projection onto the horizontal space \mathcal{H}	(15)
$\bar{g}(R)$	$\bar{g}(R) \in \mathbb{R}^{pn}$ is the vector corresponding to the Riemannian gradient of rotation averaging in the total space	(14)
$\bar{H}(R)$	$\bar{H}(R) \in \mathbb{S}^{pn}$ is the matrix corresponding to the Riemannian Hessian of rotation averaging in the total space	(14)
$H(R)$	$H(R) \in \mathbb{S}^{pn}$ is the matrix corresponding to the Riemannian Hessian in the quotient space	(15)
w	$w : \mathcal{E} \rightarrow \mathbb{R}_{>0}$ is the edge weight function that appears in Theorem 1	(17)
δ	The approximation constant in Theorem 1 between $H(R)$ and the Laplacian $L(G; w) \otimes I_p$	(17)
μ_H	Lower bound of $H(R)$ in Corollary 1	(18)
L_H	Upper bound of $H(R)$ in Corollary 1	(18)
κ_H	Condition number of $H(R)$ as defined by $\kappa_H = L_H / \mu_H$	Cor. 1
$B(R)$	$B(R) \in \mathbb{R}^{n \times p}$ is the matrix representation of the negative Riemannian gradient $-\bar{g}(R)$	(20)
Section V		
\mathcal{V}_α	The set of vertices (variables) of robot $\alpha \in [m]$, and $\mathcal{V}_\alpha = \mathcal{F}_\alpha \uplus \mathcal{C}_\alpha$	(24)
\mathcal{F}_α	$\mathcal{F}_\alpha \subseteq \mathcal{V}_\alpha$ is the set of interior vertices of robot α that does not have inter-robot measurement	
\mathcal{C}_α	$\mathcal{C}_\alpha \subseteq \mathcal{V}_\alpha$ is the set of separator vertices of robot α that have inter-robot measurement	
\mathcal{C}	$\mathcal{C} = \mathcal{C}_1 \uplus \dots \uplus \mathcal{C}_m$ is the union of separator vertices of all m robots	
\mathcal{E}_α	The set of local edges (measurements) of robot $\alpha \in [m]$	(25)
\mathcal{E}_c	The set of inter-robot edges (measurements)	(25)
S_α	$S_\alpha \in \mathcal{S}_+^{ \mathcal{C} }$ is the exact Schur complement of robot α 's local graph G_α	
S	$S \in \mathcal{S}_+^{ \mathcal{C} }$ is the exact Schur complement of the multi-robot measurement graph	(29)
\tilde{S}_α	The sparsified version of S_α robot α transmits to the server in Algorithm 2	Alg. 2, line 4
\tilde{S}	The sparsified version of S computed by the server in Algorithm 2	Alg. 2, line 6
U_α	$U_\alpha \in \mathbb{R}^{ \mathcal{C} \times p}$ is the block vector robot α transmits to the server in Algorithm 3	Alg. 3, line 4
ϵ	The spectral sparsification parameter that is used in the algorithm and appears in Theorem 2	
ρ^{TLS}	The truncated least squares (TLS) cost function for outlier-robust estimation	(39)
e_{ij}	Measurement error corresponding to the measurement $(i, j) \in \mathcal{E}$ in the measurement graph	
\bar{e}	Threshold that specifies the maximum error of inlier measurement in TLS	
μ	Control parameter of graduated non-convexity (GNC)	
w_{ij}^{GNC}	GNC weight for measurement $(i, j) \in \mathcal{E}$ in the measurement graph	(40)

Algorithm 7 SPECTRAL SPARSIFICATION BY EFFECTIVE RESISTANCE SAMPLING

```

1: for each edge  $(i, j) \in \mathcal{E}$  in the graph  $G$  corresponding to the input Laplacian  $L$  (in parallel) do
2:   Compute leverage score  $\ell_{ij} = w_{ij}(\Delta_i - \Delta_j)^\top L^\dagger (\Delta_i - \Delta_j)$ .
3:   Select this edge with probability  $p_{ij} = \min(1, 3.5 \log n \ell_{ij} / \epsilon_l^2)$ .
4:   If this edge is selected, add it to the sparsified graph  $\tilde{G}$  with increased edge weight  $w_{ij}/p_{ij}$ .
5: end for
6: return The Laplacian  $\tilde{L}$  of the sparse graph  $\tilde{G}$ .
  
```

APPENDIX I

DETAILS OF SPECTRAL SPARSIFICATION ALGORITHM

In this appendix, we provide details of the spectral sparsification algorithm used in this work. Given the Laplacian matrix L of a dense graph G , recall that the goal of spectral sparsification is to find a *sparse* Laplacian \tilde{L} such that,

$$e^{-\epsilon} L \preceq \tilde{L} \preceq e^\epsilon L, \quad (44)$$

where $\epsilon > 0$ is the desired sparsification parameter. Note that (44) is the same definition as (1) in the main paper. In graph terms, this is the same as finding a sparse graph \tilde{G} whose Laplacian approximates that of the dense graph G .

In this work, we use the random sampling approach developed by Spielman and Srivastava [20]. In particular, we implement the improved version presented in [67, Chapter 32], which is more suitable for batch computation since it avoids sampling with replacement and the decision to keep or remove each edge can be made in parallel. Given a constant $\epsilon_l \in (0, 1)$, this method produces a sparse \tilde{L} with $O(n \log n)$ entries (where n is the number of vertices in the graph) such that with high probability,

$$(1 - \epsilon_l) L \preceq \tilde{L} \preceq (1 + \epsilon_l) L. \quad (45)$$

Note that (45) can be used to ensure that (44) holds: in our implementation, given ϵ , we find the smallest ϵ_l such that (44) holds, which is given by,

$$\epsilon_l = \min(e^\epsilon - 1, 1 - e^{-\epsilon}). \quad (46)$$

The sparsification algorithm works by selecting edges in the input dense graph G based on their *leverage scores*. Recall that each edge corresponds to a non-zero off-diagonal term in the Laplacian L , and thus selecting a small subset of edges leads to a sparse output Laplacian \tilde{L} . For each edge $(i, j) \in \mathcal{E}$, its leverage score is defined as,

$$\ell_{ij} \triangleq w_{ij}(\Delta_i - \Delta_j)^\top L^\dagger (\Delta_i - \Delta_j), \quad (47)$$

where $\Delta_i \in \mathbb{R}^n$ is the i -th basis vector with a one in coordinate i , and $w_{ij} > 0$ is the edge weight. The quantity ℓ_{ij}/w_{ij} is also known as the *effective resistance*. Intuitively, the leverage score measures the importance of each edge to the connectivity of the overall graph. Fig. 13 shows an illustration on a toy graph consisting of two clusters of vertices connected by a single edge. All edges have unit weights, and each edge is labeled by its leverage score computed according to (47). Notice that the middle edge has the highest leverage score, since it is critical to keep the overall graph connected. In comparison, the remaining edges have lower leverage scores, due to the redundancy of edges in each cluster. The actual sparsification algorithm is a remarkably simple method, which independently selects each edge with a probability proportional to its leverage score:

$$p_{ij} = \min \left(1, \frac{3.5 \log n}{\epsilon_l^2} \ell_{ij} \right). \quad (48)$$

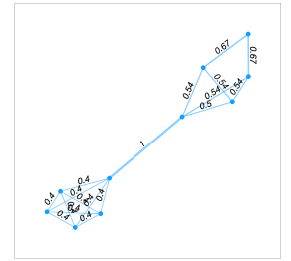


Fig. 13: Leverage scores on toy graph.

If edge $(i, j) \in \mathcal{E}$ is selected, we add it to the sparsified graph \tilde{G} with an *increased edge weight* w_{ij}/p_{ij} . The reason behind increasing the edge weight is to ensure that we can recover L in expectation, i.e., $\mathbb{E}(\tilde{L}) = L$. Algorithm 7 shows the pseudocode. The majority of computation is spent on factorizing L to compute the leverage scores in (47). The approximation guarantee (45) of the resulting \tilde{L} is proved using certain concentration bounds of random matrices. The interested reader is referred to [67, Chapter 32] for the complete proof.

Lastly, we refer the reader to Fig. 12 in the main paper, which demonstrates spectral sparsification on Laplacian matrices encountered in our application. Recall that in our case, we apply sparsification on the Schur complement S_α of robot α 's local Laplacian. Since Laplacians are closed under Schur complements [23, Fact 4.2], S_α is still a Laplacian matrix and thus the sparsified result \tilde{S}_α retains all the theoretical guarantees.

APPENDIX II

ANALYSIS OF RIEMANNIAN HESSIAN OF ROTATION AVERAGING

In this appendix, we use $\mathbf{d}_\angle \equiv \mathbf{d}$ to denote the geodesic distance on the rotation group, and use \mathbf{d}_{chr} to denote the chordal distance. Recall the definition of φ in Problem 1 as either the squared geodesic distance or the squared chordal distance,

$$\varphi(R_1, R_2) = \begin{cases} \frac{1}{2} \mathbf{d}_\angle(R_1, R_2)^2 = \frac{1}{2} \|\text{Log}(R_1^\top R_2)\|^2, & \text{squared geodesic distance,} \\ \frac{1}{2} \mathbf{d}_{\text{chr}}(R_1, R_2)^2 = \frac{1}{2} \|R_1 - R_2\|_F^2, & \text{squared chordal distance.} \end{cases} \quad (49a)$$

Using the notion of “reshaped distance” introduced in [50], we may express both cases as a function of the geodesic distance as follows,

$$\varphi(R_1, R_2) = \rho(\mathbf{d}_\angle(R_1, R_2)). \quad (50)$$

Note that the notation for reshaped distance ρ is not to be confused with ρ^{ts} in Sec. V-D, which instead denotes the truncated least squares function. It can be shown that the scalar function $\rho(\cdot)$ is defined as,

$$\rho(\theta) = \begin{cases} \theta^2/2, & \text{for squared geodesic distance (49a),} \\ 2 - 2\cos(\theta), & \text{for squared chordal distance (49b).} \end{cases} \quad (51a)$$

The first case (51a) is readily verified. The second case (51b) makes use of the relation between chordal and geodesic distances; see [68, Table 2]. To analyze the Hessian of rotation averaging (7), we start by considering the cost associated with a single relative rotation measurement,

$$f_{ij}(R_i, R_j) = \varphi(R_i \tilde{R}_{ij}, R_j). \quad (52)$$

In addition to (52), we also consider its approximation defined on the Lie algebra,

$$h_{ij}(v_i, v_j) \triangleq \varphi(\text{Exp}(v_i) R_i \tilde{R}_{ij}, \text{Exp}(v_j) R_j). \quad (53)$$

Note that (53) corresponds to a single term in the overall approximation defined in (12). Similar to (12), h_{ij} depends on the current rotation estimates R , but we omit this from our notation for simplicity. Define the gradient and Hessian of h_{ij} as follows,

$$\bar{g}_{ij} \triangleq \nabla h_{ij}(v_i, v_j)|_{v_i=v_j=0}, \quad (54)$$

$$\bar{H}_{ij} \triangleq \nabla^2 h_{ij}(v_i, v_j)|_{v_i=v_j=0}. \quad (55)$$

In the following, we first derive auxiliary results that characterize \bar{g}_{ij} and \bar{H}_{ij} . Once we understand the properties of \bar{g}_{ij} and \bar{H}_{ij} , understanding the full rotation averaging problem becomes straightforward thanks to the additive structure in the cost function (7). Note that we prove the main theoretical results Theorem 1 and Corollary 1 for 3D rotation averaging. The case of $d = 2$ can be proved using the exact same arguments, and some steps would simplify due to the fact that 2D rotations commute.

A. Auxiliary Results for 3D Rotation Averaging

Lemma 2. Consider a 3D rotation averaging problem. Let

$$\theta_{ij} = \|\text{Log}(\tilde{R}_{ij}^\top R_i^\top R_j)\|, \quad (56)$$

$$u_{ij} = \text{Log}(\tilde{R}_{ij}^\top R_i^\top R_j) / \theta_{ij}, \quad (57)$$

denote the angle-axis representation of the current rotation error. Then the gradient is given by,

$$\bar{g}_{ij} = \dot{\rho}(\theta_{ij}) \begin{bmatrix} R_i \tilde{R}_{ij} & 0 \\ 0 & R_j \end{bmatrix} \begin{bmatrix} -u_{ij} \\ u_{ij} \end{bmatrix}. \quad (58)$$

The Hessian is given by,

$$\bar{H}_{ij} = \begin{bmatrix} R_i \tilde{R}_{ij} & 0 \\ 0 & R_j \end{bmatrix} \begin{bmatrix} \mathcal{S}(\tilde{H}_{ij}) & -\tilde{H}_{ij} \\ -\tilde{H}_{ij}^\top & \mathcal{S}(\tilde{H}_{ij}) \end{bmatrix} \begin{bmatrix} R_i \tilde{R}_{ij} & 0 \\ 0 & R_j \end{bmatrix}^\top, \quad (59)$$

where $\tilde{H}_{ij} = \alpha(\theta_{ij})I + \gamma(\theta_{ij})u_{ij}u_{ij}^\top + \beta(\theta_{ij})[u_{ij}]_\times$ with

$$\alpha(\theta_{ij}) = \frac{\dot{\rho}(\theta_{ij}) \cot(\theta_{ij}/2)}{2}, \quad (60)$$

$$\gamma(\theta_{ij}) = \ddot{\rho}(\theta_{ij}) - \alpha(\theta_{ij}), \quad (61)$$

$$\beta(\theta_{ij}) = \frac{\dot{\rho}(\theta_{ij})}{2}. \quad (62)$$

Proof. Introduce new rotation variables $S_i, S_j \in \text{SO}(3)$ and consider the following function,

$$\hat{h}_{ij}(S_i, S_j) = \varphi(S_i R_i \tilde{R}_{ij}, S_j R_j). \quad (63)$$

Note that \bar{g}_{ij} and \bar{H}_{ij} correspond to the Riemannian gradient and Riemannian Hessian of (63) evaluated at $S_i = S_j = I$. Define $F : \text{SO}(3) \times \text{SO}(3) \rightarrow \text{SO}(3) \times \text{SO}(3)$ be the mapping such that,

$$F(S_i, S_j) = (S_i R_i \tilde{R}_{ij}, S_j R_j) \triangleq (\hat{S}_i, \hat{S}_j). \quad (64)$$

Then we have $\hat{h}_{ij}(S_i, S_j) = \varphi(F(S_i, S_j))$. By chain rule,

$$\text{grad } \hat{h}_{ij}(S_i, S_j) = DF(S_i, S_j)^\top [\text{grad } \varphi(\hat{S}_i, \hat{S}_j)] \quad (65)$$

$$= DF(S_i, S_j)^\top [\dot{\rho}(\theta_{ij}) \text{grad } \mathbf{d}_\angle(\hat{S}_i, \hat{S}_j)] \quad (66)$$

$$= \dot{\rho}(\theta_{ij}) DF(S_i, S_j)^\top [\text{grad } \mathbf{d}_\angle(\hat{S}_i, \hat{S}_j)]. \quad (67)$$

In (67), $DF(S_i, S_j)^\top$ stands for the adjoint operator (transpose in matrix form) of the differential $DF(S_i, S_j)$. Using the standard basis for the Lie algebra $\mathfrak{so}(3)$, Tron [50] showed that the Riemannian gradient of the geodesic distance is,

$$\text{grad } \mathbf{d}_\angle(\hat{S}_i, \hat{S}_j) = \begin{bmatrix} -u_{ij} \\ u_{ij} \end{bmatrix}, \quad (68)$$

c.f. [50, Equation (E.31)]. Substituting (68) into (67) and furthermore using the matrix form of the differential $DF(S_i, S_j)$ in the standard basis, we have

$$\bar{g}_{ij} = \text{grad } \hat{h}_{ij}(S_i, S_j) = \dot{\rho}(\theta_{ij}) \begin{bmatrix} R_i \tilde{R}_{ij} & 0 \\ 0 & R_j \end{bmatrix} \begin{bmatrix} -u_{ij} \\ u_{ij} \end{bmatrix}. \quad (69)$$

For the Riemannian Hessian, differentiating (65) again yields,

$$\text{Hess } \hat{h}_{ij}(S_i, S_j) = DF(S_i, S_j)^\top \circ \text{Hess } \varphi(\hat{S}_i, \hat{S}_j) \circ DF(S_i, S_j). \quad (70)$$

For the Hessian term in the middle of (70), we once again leverage existing results from [50, Proposition E.3.1]:

$$\text{Hess } \varphi(\hat{S}_i, \hat{S}_j) = \begin{bmatrix} \mathcal{S}(\tilde{H}_{ij}) & -\tilde{H}_{ij} \\ -\tilde{H}_{ij}^\top & \mathcal{S}(\tilde{H}_{ij}) \end{bmatrix}, \quad (71)$$

where the inner matrix \tilde{H}_{ij} is defined as,

$$\tilde{H}_{ij} = \ddot{\rho}(\theta_{ij}) u_{ij} u_{ij}^\top + \frac{\dot{\rho}(\theta_{ij})}{\theta_{ij}} (D \text{Log}(\tilde{R}_{ij}^\top R_i^\top R_j) - u_{ij} u_{ij}^\top). \quad (72)$$

Using the expression for the differential of the logarithm map [50, Proposition E.2.1], the previous expression further simplifies to,

$$\begin{aligned} \tilde{H}_{ij} &= \ddot{\rho}(\theta_{ij}) u_{ij} u_{ij}^\top + \frac{\dot{\rho}(\theta_{ij})}{\theta_{ij}} \left(u_{ij} u_{ij}^\top + \frac{\theta_{ij}}{2} \left([u_{ij}]_\times - \cot(\theta_{ij}/2) [u_{ij}]_\times^2 \right) - u_{ij} u_{ij}^\top \right) \\ &= \ddot{\rho}(\theta_{ij}) u_{ij} u_{ij}^\top + \frac{\dot{\rho}(\theta_{ij})}{2} \left([u_{ij}]_\times - \cot(\theta_{ij}/2) [u_{ij}]_\times^2 \right) \\ &= \ddot{\rho}(\theta_{ij}) u_{ij} u_{ij}^\top + \frac{\dot{\rho}(\theta_{ij})}{2} [u_{ij}]_\times - \frac{\dot{\rho}(\theta_{ij}) \cot(\theta_{ij}/2)}{2} (-I + u_{ij} u_{ij}^\top) \\ &= \frac{\dot{\rho}(\theta_{ij}) \cot(\theta_{ij}/2)}{2} I + \left(\ddot{\rho}(\theta_{ij}) - \frac{\dot{\rho}(\theta_{ij}) \cot(\theta_{ij}/2)}{2} \right) u_{ij} u_{ij}^\top + \frac{\dot{\rho}(\theta_{ij})}{2} [u_{ij}]_\times \\ &= \alpha(\theta_{ij}) I + \gamma(\theta_{ij}) u_{ij} u_{ij}^\top + \beta(\theta_{ij}) [u_{ij}]_\times. \end{aligned} \quad (73)$$

To conclude, the Hessian is obtained by substituting the above results into (70):

$$\bar{H}_{ij} = \text{Hess } \hat{h}_{ij}(S_i, S_j) = \begin{bmatrix} R_i \tilde{R}_{ij} & 0 \\ 0 & R_j \end{bmatrix} \begin{bmatrix} \mathcal{S}(\tilde{H}_{ij}) & -\tilde{H}_{ij} \\ -\tilde{H}_{ij}^\top & \mathcal{S}(\tilde{H}_{ij}) \end{bmatrix} \begin{bmatrix} R_i \tilde{R}_{ij} & 0 \\ 0 & R_j \end{bmatrix}^\top. \quad (74)$$

□

The Hessian expression in Lemma 2 is complicated in general. However, we will show that as the angular error θ_{ij} tends to zero, the Hessian \bar{H}_{ij} converges to a particular simple form. We note that the case under geodesic distance (Lemma 3 below) can also be derived as a special case of [51, Theorem 1].

Lemma 3 (Limit of \overline{H}_{ij} under geodesic distance). *For rotation averaging under the geodesic distance, it holds that,*

$$\lim_{\theta_{ij} \rightarrow 0} \overline{H}_{ij}(\theta_{ij}) = \begin{bmatrix} I_3 & -I_3 \\ -I_3 & I_3 \end{bmatrix}. \quad (75)$$

Proof. We first compute limits of $\alpha(\theta)$, $\gamma(\theta)$, and $\beta(\theta)$ that appear in the definition of \overline{H}_{ij} . For rotation averaging under the geodesic distance, the scalar function $\rho(\theta)$ is defined as in (51a). In this case, we have

$$\dot{\rho}(\theta) = \theta, \quad \ddot{\rho}(\theta) = 1. \quad (76)$$

Substituting into (60)-(62),

$$\alpha(\theta) = \frac{1}{2} \theta \cot(\theta/2) = \frac{1}{2} \frac{\theta}{\sin(\theta/2)} \cos(\theta/2), \quad (77)$$

$$\gamma(\theta) = 1 - \alpha(\theta), \quad (78)$$

$$\beta(\theta) = \theta/2. \quad (79)$$

Take the limit as θ tends to zero,

$$\lim_{\theta \rightarrow 0} \alpha(\theta) = \frac{1}{2} \cdot \lim_{\theta \rightarrow 0} \frac{\theta}{\sin(\theta/2)} \cdot \lim_{\theta \rightarrow 0} \cos(\theta/2) = 1, \quad (80)$$

$$\lim_{\theta \rightarrow 0} \gamma(\theta) = 1 - \lim_{\theta \rightarrow 0} \alpha(\theta) = 0, \quad (81)$$

$$\lim_{\theta \rightarrow 0} \beta(\theta) = 0. \quad (82)$$

Define the following matrix,

$$P = \begin{bmatrix} R_i \tilde{R}_{ij} & 0 \\ 0 & R_j \end{bmatrix}. \quad (83)$$

From the definition of \overline{H}_{ij} in (59),

$$\begin{aligned} \overline{H}_{ij} &= \alpha(\theta_{ij}) P \begin{bmatrix} I_3 & -I_3 \\ -I_3 & I_3 \end{bmatrix} P^\top \\ &\quad + \gamma(\theta_{ij}) P \begin{bmatrix} u_{ij} u_{ij}^\top & -u_{ij} u_{ij}^\top \\ -u_{ij} u_{ij}^\top & u_{ij} u_{ij}^\top \end{bmatrix} P^\top \\ &\quad + \beta(\theta_{ij}) P \begin{bmatrix} 0_3 & -[u_{ij}]_\times \\ -[u_{ij}]_\times^\top & 0_3 \end{bmatrix} P^\top. \end{aligned} \quad (84)$$

Since $\lim_{\theta \rightarrow 0} \gamma(\theta) = \lim_{\theta \rightarrow 0} \beta(\theta) = 0$ and all matrices involved in (84) are bounded, we conclude that the last two terms in (84) vanish as θ_{ij} converges to zero. For the first term in (84), notice that,

$$\alpha(\theta_{ij}) P \begin{bmatrix} I_3 & -I_3 \\ -I_3 & I_3 \end{bmatrix} P^\top = \alpha(\theta_{ij}) \begin{bmatrix} I_3 & -R_i \tilde{R}_{ij} R_j^\top \\ -R_j \tilde{R}_{ij}^\top R_i^\top & I_3 \end{bmatrix}. \quad (85)$$

As θ_{ij} tends to zero, $\alpha(\theta_{ij})$ converges to 1 and the off-diagonal blocks in (85) tend to $-I_3$. Hence the proof is completed. \square

Lemma 4 (Limit of \overline{H}_{ij} under chordal distance). *For rotation averaging under the chordal distance, it holds that,*

$$\lim_{\theta_{ij} \rightarrow 0} \overline{H}_{ij}(\theta_{ij}) = 2 \begin{bmatrix} I_3 & -I_3 \\ -I_3 & I_3 \end{bmatrix}. \quad (86)$$

Proof. For rotation averaging under the chordal distance, the scalar function $\rho(\theta)$ is defined as in (51b). In this case, we have

$$\dot{\rho}(\theta) = 2 \sin(\theta), \quad \ddot{\rho}(\theta) = 2 \cos(\theta). \quad (87)$$

Substituting into (60)-(62),

$$\alpha(\theta) = \sin(\theta) \cot(\theta/2) = 2 \cos(\theta/2)^2, \quad (88)$$

$$\gamma(\theta) = 2 \cos(\theta) - \alpha(\theta), \quad (89)$$

$$\beta(\theta) = \sin(\theta). \quad (90)$$

Take the limit as θ tends to zero,

$$\lim_{\theta \rightarrow 0} \alpha(\theta) = 2, \quad (91)$$

$$\lim_{\theta \rightarrow 0} \gamma(\theta) = 2 - \lim_{\theta \rightarrow 0} \alpha(\theta) = 0, \quad (92)$$

$$\lim_{\theta \rightarrow 0} \beta(\theta) = 0. \quad (93)$$

The remaining proof is similar to that of Lemma 3 and is omitted. \square

B. Proof of Theorem 1

Proof. We will use Lemma 3 to prove the theorem for the case of squared geodesic cost. The case of squared chordal cost is analogous: instead of Lemma 3, we will use Lemma 4 and the remaining steps are the same. Recall the approximation of the overall cost function defined in (12):

$$h(v; R) = \sum_{(i,j) \in \mathcal{E}} \kappa_{ij} h_{ij}(v_i, v_j) = \sum_{(i,j) \in \mathcal{E}} \kappa_{ij} \varphi(\text{Exp}(v_i) R_i \tilde{R}_{ij}, \text{Exp}(v_j) R_j), \quad (94)$$

Observe that the Hessian of $h(v; R)$ is simply given by the sum of the Hessian matrices of $h_{ij}(v_i, v_j)$, after “lifting” the latter to the dimension of the full optimization problem, *i.e.*,

$$\bar{H}(R) = \sum_{(i,j) \in \mathcal{E}} \kappa_{ij} W_{ij}, \quad W_{ij} = \begin{matrix} & & i & & j & & \\ & & \vdots & & \vdots & & \\ i & \left[\begin{array}{ccc} \dots & \bar{H}_{ij}^{(ii)} & \dots & \bar{H}_{ij}^{(ij)} & \dots \\ & \vdots & & \vdots & \\ j & \dots & \bar{H}_{ij}^{(ji)} & \dots & \bar{H}_{ij}^{(jj)} & \dots \\ & \vdots & & \vdots & \end{array} \right] & & \\ & & \vdots & & \vdots & & \end{matrix}. \quad (95)$$

In (95), W_{ij} is formed by placing the p -by- p blocks of \bar{H}_{ij} defined in (59) in corresponding locations of the full matrix. For instance, $\bar{H}_{ij}^{(ii)}$ is the block of \bar{H}_{ij} that corresponds to vertex i .

In the following, let $\theta_{ij}(R)$ denote the residual of edge $(i, j) \in \mathcal{E}$ evaluated at $R \in \text{SO}(d)^n$. From (95) and Lemma 3, we see that $\bar{H}(R)$ has the following limit point as all edge residuals tend to zero,

$$\lim_{\substack{\theta_{ij}(R) \rightarrow 0, \\ \forall (i,j) \in \mathcal{E}}} \bar{H}(R) = M \triangleq L(G; \kappa) \otimes I_p. \quad (96)$$

Recall from Remark 2 that $M \succeq 0$ and $\ker(M) = \mathcal{N}$ where \mathcal{N} is the vertical space defined in (13). In addition, recall the definition of $H(R)$ in (15):

$$H(R) = P_H \bar{H}(R) P_H. \quad (97)$$

Since P_H is the (constant) orthogonal projection matrix onto the horizontal space $\mathcal{H} = \mathcal{N}^\perp$, it holds that,

$$\lim_{\substack{\theta_{ij}(R) \rightarrow 0, \\ \forall (i,j) \in \mathcal{E}}} H(R) = P_H M P_H = M. \quad (98)$$

Note that for singular symmetric matrices A and B , $A \approx_\delta B$ necessarily means that $\ker(A) = \ker(B)$. Therefore, to prove the theorem, we must first show that $\ker(H(R)) = \ker(M) = \mathcal{N}$ under our assumptions. Let $\lambda_1(A), \lambda_2(A), \dots$ denote the eigenvalues of a symmetric matrix A sorted in increasing order. By construction, \mathcal{N} is always contained in $\ker(H(R))$, and thus $\dim(\mathcal{N}) = p$ eigenvalues of $H(R)$ are always zero. Next, we will show that if all measurement residuals are sufficiently small, then the remaining $pn - p$ eigenvalues of $H(R)$ will be strictly positive. Define $E(R) \triangleq H(R) - M$. Let x be any unit vector such that $x \perp \mathcal{N}$. Note that,

$$\begin{aligned} x^\top H(R) x &= x^\top M x + x^\top E(R) x \\ &\geq \lambda_{p+1}(M) - \|E(R)\|_2. \end{aligned} \quad (99)$$

Since $M = L(G; \kappa) \otimes I_p$, it holds that $\lambda_{p+1}(M) = \lambda_2(L(G; \kappa))$. The latter is known as the *algebraic connectivity* which is always positive for a connected graph G . Thus $\lambda_{p+1}(M) > 0$ and by (98), we also have $\lim_{\theta_{ij}(R) \rightarrow 0} E(R) = 0$. Consequently, when all $\theta_{ij}(R)$ are sufficiently small, the right-hand side of (99) is strictly positive, *i.e.*, there exists $\bar{\theta}_1 > 0$ such that if $\theta_{ij}(R) \leq \bar{\theta}_1$ for all $(i, j) \in \mathcal{E}$, we have,

$$\ker(H(R)) = \ker(M) = \mathcal{N}. \quad (100)$$

Under (100), the desired approximation $H(R) \approx_\delta M$ is equivalent to,

$$e^{-\delta} P_H \preceq M^{\frac{1}{2}} H(R) M^{\frac{1}{2}} \preceq e^{\delta} P_H, \quad (101)$$

where $M^{\frac{1}{2}}$ denotes the square root of the pseudoinverse of M , and P_H is the orthogonal projection onto the horizontal space \mathcal{H} . This condition is true if and only if the nontrivial eigenvalues are bounded as follows,

$$\lambda_{p+1}(M^{\frac{1}{2}}H(R)M^{\frac{1}{2}}) \geq e^{-\delta}, \quad \lambda_{pn}(M^{\frac{1}{2}}H(R)M^{\frac{1}{2}}) \leq e^{\delta}. \quad (102)$$

Using the convergence result (98) and the eigenvalue perturbation bounds in [69, Corollary 6.3.8], we conclude that there exists $\bar{\theta}_0 \in (0, \bar{\theta}_1]$ such that if $R \in \text{SO}(d)^n$ satisfies

$$\theta_{ij}(R) \leq \bar{\theta}_0, \quad \forall (i, j) \in \mathcal{E}, \quad (103)$$

then (102) holds, *i.e.*, we have the desired approximation,

$$H(R) \approx_{\delta} M. \quad (104)$$

To conclude the proof, we need to show that there exist $\bar{\theta}, r > 0$ such that condition (103) holds for all $R \in B_r(R^*)$. Let us first consider residuals at the global minimizer R^* . Using assumption (16) and the cost function, we obtain the following simple bound:

$$\max_{(i,j) \in \mathcal{E}} \frac{\kappa_{ij} \theta_{ij}(R^*)^2}{2} \leq f(R^*) \leq f(\underline{R}) \leq \frac{\sum_{(i,j) \in \mathcal{E}} \kappa_{ij} \bar{\theta}^2}{2}. \quad (105)$$

It can be verified that if,

$$\bar{\theta} \leq \frac{\bar{\theta}_0}{2} \sqrt{\frac{\min_{(i,j) \in \mathcal{E}} \kappa_{ij}}{\sum_{(i,j) \in \mathcal{E}} \kappa_{ij}}}, \quad (106)$$

then (105) yields $\theta_{ij}(R^*) \leq \bar{\theta}_0/2$ for all edges $(i, j) \in \mathcal{E}$. Finally, let us select $r \in (0, \bar{\theta}_0/4)$. For $i \in [n]$, let $E_i \in \text{SO}(d)$ such that $R_i = E_i R_i^*$. Using the triangle inequality and the fact that the geodesic distance $\mathbf{d}_{\angle}(\cdot, \cdot)$ is bi-invariant, we can show that for any $R \in B_r(R^*)$,

$$\theta_{ij}(R) = \mathbf{d}_{\angle}(R_i \tilde{R}_{ij}, R_j) \quad (107)$$

$$= \mathbf{d}_{\angle}(E_i R_i^* \tilde{R}_{ij}, E_j R_j^*) \quad (108)$$

$$= \mathbf{d}_{\angle}(R_i^* \tilde{R}_{ij} (R_j^*)^{\top}, E_i^{\top} E_j) \quad (109)$$

$$\leq \mathbf{d}_{\angle}(R_i^* \tilde{R}_{ij} (R_j^*)^{\top}, I) + \mathbf{d}_{\angle}(E_i, I) + \mathbf{d}_{\angle}(E_j, I) \quad (110)$$

$$\leq \theta_{ij}(R^*) + 2r \quad (111)$$

$$\leq \bar{\theta}_0. \quad (112)$$

In summary, we have shown that if $\bar{\theta}$ satisfies (106) and furthermore $0 < r < \bar{\theta}_0/4$, then the desired approximation $M \approx_{\delta} H(R)$ holds for all $R \in B_r(R^*)$. This concludes the proof. \square

C. Proof of Corollary 1

Proof. To simplify notation, we use L to denote $L(G; w)$. By (17), it holds that,

$$e^{-\delta}(L \otimes I_p) \preceq H(R) \preceq e^{\delta}(L \otimes I_p). \quad (113)$$

Note that the eigenvalues of $L \otimes I_p$ are given by the eigenvalues of L , repeated p times. Therefore, the desired result follows by noting that,

$$\lambda_2(L)P_H \preceq L \otimes I_p \preceq \lambda_n(L)P_H. \quad (114)$$

\square

D. Connections between Approximate Cost (12) and the Pullback Function

In this subsection, we show that the approximate cost function in (12) is related to the standard *pullback function* [25], [26] of rotation averaging in the total space via a *change of variable*. As before, we focus on the case of $d = 3$ and the derivations can be simplified for $d = 2$. Given $R = (R_1, \dots, R_n) \in \text{SO}(3)^n$, let $\bar{f}(R)$ denote the cost function in rotation averaging (Problem 1). The standard pullback function, using the Riemannian exponential map as retraction, is defined as,

$$\hat{f}(\eta) \triangleq \bar{f}(\text{Exp}_R(\eta)), \quad (115)$$

where $\eta = (\eta_1, \dots, \eta_n) \in T_R \text{SO}(3)^n$. For every $i \in [n]$, η_i is a tangent vector $\eta_i \in T_{R_i} \text{SO}(3)$ where $\eta_i = R_i [u_i]_{\times}$ for some $u_i \in \mathbb{R}^3$ [25, Example 3.5.3]. The Riemannian exponential map is given by $\text{Exp}_R(\eta) = (\text{Exp}_{R_1}(\eta_1), \dots, \text{Exp}_{R_n}(\eta_n))$, and for every $i \in [n]$,

$$\text{Exp}_{R_i}(\eta_i) = R_i \text{Exp}(u_i), \quad (116)$$

where $\text{Exp}(\cdot)$ is defined in (5); see also [50, Equation 2.23]. Next, let us define $v_i \triangleq R_i u_i$. Using the adjoint operator on $\text{SO}(3)$, we see that,

$$\text{Exp}_{R_i}(\eta_i) = R_i \text{Exp}(u_i) = \text{Exp}(v_i) R_i. \quad (117)$$

Combining the fact that $\eta_i = R_i [u_i]_\times$ and $v_i = R_i u_i$, we see that $\eta_i \in T_{R_i} \text{SO}(3)$ is related to $v_i \in \mathbb{R}^3$ via a linear and invertible mapping:

$$\eta_i = R_i [R_i^\top v_i]_\times. \quad (118)$$

Using (118), we can write the pullback (115) using the new variable $v \triangleq [v_1^\top \dots v_n^\top]^\top \in \mathbb{R}^{3n}$,

$$h(v; R) \triangleq \hat{f}(\eta(v)) = f(\text{Exp}(v_1) R_1, \dots, \text{Exp}(v_n) R_n), \quad (119)$$

where we use $\eta(v)$ to denote the change of variable from $v \in \mathbb{R}^{3n}$ to $\eta \in T_R \text{SO}(3)^n$. Note that $h(v; R)$ defined in (119) corresponds exactly with (12) after expanding the cost function $f(\cdot)$ using its definition.

In Riemannian Newton's method, one computes each iteration by minimizing a *quadratic model* of the pullback function (115). On the total space, the quadratic model is defined as follows,

$$\hat{f}(\eta) \approx \hat{m}(\eta) \triangleq \hat{f}(0) + \langle \nabla \hat{f}(0), \eta \rangle + \frac{1}{2} \langle \nabla^2 \hat{f}(0)[\eta], \eta \rangle. \quad (120)$$

By Proposition 3.59 and Proposition 5.45 in [26], it holds that,

$$\nabla \hat{f}(0) = \text{grad } \bar{f}(R), \quad \nabla^2 \hat{f}(0) = \text{Hess } \bar{f}(R), \quad (121)$$

where $\text{grad } \bar{f}(R) \in T_R \text{SO}(3)^n$ and $\text{Hess } \bar{f}(R) : T_R \text{SO}(3)^n \rightarrow T_R \text{SO}(3)^n$ are the conventional Riemannian gradient and Hessian on the total space. With the change of variable from $\eta \in T_R \text{SO}(3)$ to $v \in \mathbb{R}^{3n}$, we note that minimizing (120) is equivalent to minimizing the following quadratic model defined using v :

$$h(v; R) \approx m(v; R) \triangleq h(0; R) + \langle \bar{g}(R), v \rangle + \frac{1}{2} \langle \bar{H}(R)v, v \rangle, \quad (122)$$

where $\bar{g}(R)$ and $\bar{H}(R)$ are defined in (14) in the main paper.

APPENDIX III PERFORMANCE GUARANTEES FOR COLLABORATIVE LAPLACIAN SOLVER

A. Proof of Lemma 1

Proof. By definition in (27),

$$S = L_{cc} - \sum_{\alpha \in [m]} L_{c\alpha} L_{\alpha\alpha}^{-1} L_{\alpha c}. \quad (123)$$

Above, L_{cc} is the block of the full Laplacian L that corresponds to the separators, denoted as $L_{cc} \equiv L(G)_{cc}$. Note that L_{cc} can be decomposed as the sum,

$$L_{cc} = L(G_c) + \sum_{\alpha \in [m]} L(G_\alpha)_{cc}. \quad (124)$$

Intuitively, the first term in (124) accounts for inter-robot edges \mathcal{E}_c , and the second group of terms accounts for robots' local edges \mathcal{E}_α ; see Fig. 1b. Substitute (124) into (123),

$$\begin{aligned} S &= L(G_c) + \sum_{\alpha \in [m]} (L(G_\alpha)_{cc} - L_{c\alpha} L_{\alpha\alpha}^{-1} L_{\alpha c}) \\ &= L(G_c) + \sum_{\alpha \in [m]} \text{Sc}(L(G_\alpha), \mathcal{F}_\alpha). \end{aligned} \quad (125)$$

□

Algorithm 8 APPROXIMATE NEWTON METHOD

```

1: for iteration  $k = 0, 1, \dots$  do
2:    $\eta^k = -M(x^k)^{-1} \text{grad } f(x^k)$ .
3:   Update iterate by  $x^{k+1} = \text{Retr}_{x^k}(\eta^k)$ .
4: end for

```

B. Proof of Theorem 2

Proof. Let us simplify the notations in the Laplacian system (26) by considering interior nodes from all robots as a single block:

$$\begin{bmatrix} L_{ff} & L_{fc} \\ L_{cf} & L_{cc} \end{bmatrix} \begin{bmatrix} X_f \\ X_c \end{bmatrix} = \begin{bmatrix} B_f \\ B_c \end{bmatrix} \quad (126)$$

where

$$L_{ff} = \text{Diag}(L_{11}, \dots, L_{mm}), \quad (127)$$

$$L_{cf} = L_{fc}^\top = [L_{c1} \ \dots \ L_{cm}], \quad (128)$$

$$X_f = [X_1^\top \ \dots \ X_m^\top]^\top, \quad (129)$$

$$B_f = [B_1^\top \ \dots \ B_m^\top]^\top. \quad (130)$$

By applying the Schur complement to (126), we obtain the following factorization for the input Laplacian system $LX = B$,

$$\underbrace{\begin{bmatrix} I & 0 \\ L_{cf}L_{ff}^{-1} & I \end{bmatrix} \begin{bmatrix} L_{ff} & 0 \\ 0 & S \end{bmatrix} \begin{bmatrix} I & L_{ff}^{-1}L_{fc} \\ 0 & I \end{bmatrix}}_L \begin{bmatrix} X_f \\ X_c \end{bmatrix} = \begin{bmatrix} B_f \\ B_c \end{bmatrix}, \quad (131)$$

where $S = \text{Sc}(L, \mathcal{F})$ is the Schur complement that appears in (27). It can be verified that Algorithm 3 returns a solution to the following system,

$$\underbrace{\begin{bmatrix} I & 0 \\ L_{cf}L_{ff}^{-1} & I \end{bmatrix} \begin{bmatrix} L_{ff} & 0 \\ 0 & \tilde{S} \end{bmatrix} \begin{bmatrix} I & L_{ff}^{-1}L_{fc} \\ 0 & I \end{bmatrix}}_{\tilde{L}} \begin{bmatrix} X_f \\ X_c \end{bmatrix} = \begin{bmatrix} B_f \\ B_c \end{bmatrix}. \quad (132)$$

Recall from Lemma 1 that,

$$S = L(G_c) + \sum_{\alpha \in [m]} S_\alpha. \quad (133)$$

Meanwhile, by construction, \tilde{S} is given by,

$$\tilde{S} = L(G_c) + \sum_{\alpha \in [m]} \tilde{S}_\alpha, \quad (134)$$

where $\tilde{S}_\alpha \approx_\epsilon S_\alpha$ for all $\alpha \in [m]$. Since spectral approximation is preserved under addition, it holds that $\tilde{S} \approx_\epsilon S$. Furthermore, by comparing L defined in (131) and \tilde{L} defined in (132) and using [23, Fact 3.2], we conclude that $\tilde{L} \approx_\epsilon L$ and thus (31) is true. Lastly, (32) follows from Lemma 5. \square

APPENDIX IV CONVERGENCE ANALYSIS

In this section, we establish convergence guarantees for the collaborative rotation averaging (Algorithm 4) and translation estimation (Algorithm 5) methods developed in Sec. V. Between the two, analyzing Algorithm 4 is more complicated owing to the fact that rotation averaging is an optimization problem defined on a Riemannian manifold. To establish its convergence, in Sec. IV-A we first prove a more general result that holds for generic approximate Newton methods on manifolds. Then, in Sec. IV-B, we invoke this result for the special case of rotation averaging and show that Algorithm 4 enjoys a local *linear* convergence rate. Lastly, in Sec. IV-C, we prove the linear convergence of translation estimation (Algorithm 5).

A. Analysis of General Approximate Newton Method

In this subsection, we consider a generic optimization problem on a smooth Riemannian manifold \mathcal{M} :

$$\min_{x \in \mathcal{M}} f(x). \quad (135)$$

We consider solving the above problem using an *approximate Newton method* described in Algorithm 8. At each iteration, the Riemannian Hessian $\text{Hess } f(x)$ is replaced with an approximation $M(x)$, and the update is computed by solving a linear

system in $M(x)$; see line 2. We will show that under the following assumptions (in particular, $M(x)$ is a sufficiently good approximation of $\text{Hess } f(x)$), Algorithm 8 achieves a local linear rate of convergence.

Assumption 1. Let x^* denote a strict second-order critical point. There exist $\mu_H, L_H, \beta, \epsilon > 0$ such that for all x in a neighborhood \mathcal{U} of x^* ,

(A1) $\mu_H I \preceq \text{Hess } f(x) \preceq L_H I$.

(A2) $M(x)$ is invertible and $\|M(x)^{-1}\| \leq \beta$.

(A3) $M(x) \approx_\epsilon \text{Hess } f(x)$ and ϵ satisfies

$$\gamma(\epsilon) \triangleq 2\sqrt{\kappa_H}c(\epsilon) < 1, \quad (136)$$

where $c(\epsilon)$ is defined in (33) and $\kappa_H = L_H/\mu_H$ is the condition number.

Theorem 5. Under Assumption 1, there exists a neighborhood $\mathcal{U}' \subseteq \mathcal{U}$ such that for all $x_0 \in \mathcal{U}'$, Algorithm 8 generates an infinite sequence x^k converging linearly to x^* . Furthermore, the linear convergence factor is given by,

$$\limsup_{k \rightarrow \infty} \frac{\mathbf{d}(x^{k+1}, x^*)}{\mathbf{d}(x^k, x^*)} = \gamma(\epsilon). \quad (137)$$

Proof. We prove the theorem by adapting the local convergence analysis of the Riemannian Newton method presented in [25, Theorem 6.3.2]. Let (\mathcal{U}', φ) be a local coordinate chart defined by the normal coordinates around x^* . Similar to the original proof, we will use the $\hat{\cdot}$ notation to denote coordinate expressions in this chart. In particular, let us define,

$$\hat{x} = \varphi(x) = \text{Exp}_{x^*}^{-1}(x). \quad (138)$$

Note that under the normal coordinates, we have $\hat{x}^* = 0$, $\text{Exp}_{x^*}(\hat{x}) = x$, and $\mathbf{d}(x, x^*) = \|\hat{x}\|$. In addition, let us define,

$$\hat{\eta} = \text{D } \varphi(x)[\eta], \quad \eta \in T_x \mathcal{M}, \quad (139)$$

$$\hat{g}(\hat{x}^k) = \text{D } \varphi(x^k)[\text{grad } f], \quad (140)$$

$$\hat{H}(\hat{x}^k) = \text{D } \varphi(x^k) \circ \text{Hess } f(x^k) \circ (\text{D } \varphi(x^k))^{-1}, \quad (141)$$

$$\hat{R}_{\hat{x}}(\hat{\eta}) = \varphi(\text{Retr}_x(\eta)), \quad \eta \in T_x \mathcal{M}, \quad (142)$$

to be the coordinate expressions of vector fields, gradient, Hessian, and the retraction, respectively. Finally, let \hat{M} denote the coordinate expression of the linear map M used in Algorithm 8:

$$\hat{M}(\hat{x}^k) = \text{D } \varphi(x_k) \circ M(x^k) \circ (\text{D } \varphi(x_k))^{-1}. \quad (143)$$

Let us express each iteration of Algorithm 8 in the chart,

$$\hat{x}^{k+1} = \hat{R}_{\hat{x}^k}(-\hat{M}(\hat{x}^k)^{-1}\hat{g}(\hat{x}^k)). \quad (144)$$

Using the triangle inequality, we can bound the distance between x^{k+1} and x^* ,

$$\begin{aligned} \mathbf{d}(x^{k+1}, x^*) &= \|\hat{x}^{k+1} - \hat{x}^*\| \\ &= \|\hat{R}_{\hat{x}^k}(-\hat{M}(\hat{x}^k)^{-1}\hat{g}(\hat{x}^k)) - \hat{x}^*\| \\ &\leq \underbrace{\|\hat{R}_{\hat{x}^k}(-\hat{M}(\hat{x}^k)^{-1}\hat{g}(\hat{x}^k)) - (\hat{x}^k - \hat{M}(\hat{x}^k)^{-1}\hat{g}(\hat{x}^k))\|}_A + \\ &\quad \underbrace{\|\hat{x}^k - \hat{M}(\hat{x}^k)^{-1}\hat{g}(\hat{x}^k) - \hat{x}^*\|}_B \end{aligned} \quad (145)$$

In the following, we will derive upper bounds for A and B as a function of $\|\hat{x}^k - \hat{x}^*\| = \mathbf{d}(x^k, x^*)$.

a) *Bounding A:* Note that at x^* , we have $\text{D } \varphi(x^*) = I$. Since φ is smooth, there exists $r_1 > 0$ such that for all $x \in B_{r_1}(x^*) = \{x \in \mathcal{M}, \mathbf{d}(x, x^*) < r_1\}$,

$$\|\text{D } \varphi(x)\| \leq \sqrt{2}, \quad \|(\text{D } \varphi(x))^{-1}\| \leq \sqrt{2}. \quad (146)$$

It follows from (A2) and (143) that,

$$\|\hat{M}(\hat{x})^{-1}\| \leq 2\beta, \quad \forall x \in B_{r_1}(x^*). \quad (147)$$

Furthermore, Assumption (A1) implies that the gradient is Lipschitz continuous. Using the fact that $\hat{g}(\hat{x}^*) = 0$ (since x^* is a critical point), we have the following upper bound for the norm of the Newton step,

$$\begin{aligned} \|\hat{M}(\hat{x}^k)^{-1}\hat{g}(\hat{x}^k)\| &= \|\hat{M}(\hat{x}^k)^{-1}(\hat{g}(\hat{x}^k) - \hat{g}(\hat{x}^*))\| \\ &\leq 2\beta L' \|\hat{x}^k - \hat{x}^*\|, \end{aligned} \quad (148)$$

where $L' > 0$ is a fixed constant. Using the local rigidity property of the retraction (e.g., see [25, Definition 4.1.1]), we have that,

$$\left\| \widehat{R}_{\widehat{x}}(\widehat{\eta}) - (\widehat{x} + \widehat{\eta}) \right\| = O(\|\widehat{\eta}\|^2), \quad (149)$$

for all x in a neighborhood of x^* and all η sufficiently small; see also the discussions in [25, p. 115]. It follows from (149) and (148) that there exists $r_2, C_2 > 0$ such that

$$A \leq C_2 \|\widehat{x}^k - \widehat{x}^*\|^2, \quad (150)$$

for all $x^k \in B_{r_2}(x^*)$.

b) Bounding B : To begin, we derive the following upper bound for B using triangle inequality,

$$\begin{aligned} B &= \left\| \widehat{x}^k - \widehat{M}(\widehat{x}^k)^{-1} \widehat{g}(\widehat{x}^k) - \widehat{x}^* \right\| \\ &= \left\| \widehat{M}(\widehat{x}^k)^{-1} \left[\widehat{g}(\widehat{x}^*) - \widehat{g}(\widehat{x}^k) - \widehat{M}(\widehat{x}^k)(\widehat{x}^* - \widehat{x}^k) \right] \right\| \\ &= \left\| \widehat{M}(\widehat{x}^k)^{-1} \left[\widehat{g}(\widehat{x}^*) - \widehat{g}(\widehat{x}^k) - \widehat{H}(\widehat{x}^k)(\widehat{x}^* - \widehat{x}^k) - (\widehat{M}(\widehat{x}^k) - \widehat{H}(\widehat{x}^k))(\widehat{x}^* - \widehat{x}^k) \right] \right\| \\ &\leq \underbrace{\left\| \widehat{M}(\widehat{x}^k)^{-1} \left[\widehat{g}(\widehat{x}^*) - \widehat{g}(\widehat{x}^k) - \widehat{H}(\widehat{x}^k)(\widehat{x}^* - \widehat{x}^k) \right] \right\|}_{B_1} + \\ &\quad \underbrace{\left\| \left[I - \widehat{M}(\widehat{x}^k)^{-1} \widehat{H}(\widehat{x}^k) \right] (\widehat{x}^* - \widehat{x}^k) \right\|}_{B_2} \end{aligned} \quad (151)$$

To bound B_1 , it follows from (147) that,

$$B_1 \leq 2\beta \left\| \widehat{g}(\widehat{x}^*) - \widehat{g}(\widehat{x}^k) - \widehat{H}(\widehat{x}^k)(\widehat{x}^* - \widehat{x}^k) \right\|. \quad (152)$$

Furthermore, in the proof of [25, Theorem 6.3.2], it is shown that there exist $r_3, C_3 > 0$ such that,

$$\left\| \widehat{g}(\widehat{x}^*) - \widehat{g}(\widehat{x}^k) - \widehat{H}(\widehat{x}^k)(\widehat{x}^* - \widehat{x}^k) \right\| \leq C_3 \|\widehat{x}^k - \widehat{x}^*\|^2, \quad (153)$$

for $x^k \in B_{r_3}(x^*)$. Combining this result with (152), it holds that,

$$B_1 \leq 2\beta C_3 \|\widehat{x}^k - \widehat{x}^*\|^2. \quad (154)$$

It remains to establish an upper bound for the matrix that appears in B_2 :

$$I - \widehat{M}(\widehat{x}^k)^{-1} \widehat{H}(\widehat{x}^k) = D\varphi(x) \circ (I - M(x^k)^{-1} \text{Hess } f(x^k)) \circ (D\varphi(x))^{-1}. \quad (155)$$

In the following, we first bound the norm of $I - M(x^k)^{-1} \text{Hess } f(x^k)$. For any $\eta \in T_{x^k} \mathcal{M}$, let us consider the following quantity,

$$\begin{aligned} &\left\| (I - M(x^k)^{-1} \text{Hess } f(x^k)) \eta \right\|_{H^k} \\ &= \left\| (\text{Hess } f(x^k)^{-1} - M(x^k)^{-1}) \text{Hess } f(x^k) \eta \right\|_{H^k}, \end{aligned} \quad (156)$$

where $\|\varepsilon\|_{H^k} = \sqrt{\langle \varepsilon, \text{Hess } f(x^k) \varepsilon \rangle}$ denotes the norm induced by the Riemannian Hessian. Since $M(x^k) \approx_\epsilon \text{Hess } f(x^k)$ by Assumption (A3), we can use Lemma 5 to obtain an upper bound of (156),

$$\left\| (\text{Hess } f(x^k)^{-1} - M(x^k)^{-1}) \text{Hess } f(x^k) \eta \right\|_{H^k} \leq c(\epsilon) \|\eta\|_{H^k}. \quad (157)$$

In addition, using Assumption (A1), it holds that,

$$\sqrt{\mu_H} \|\varepsilon\| \leq \|\varepsilon\|_{H^k} \leq \sqrt{L_H} \|\varepsilon\|, \quad \forall \varepsilon \in T_{x^k} \mathcal{M}. \quad (158)$$

Combining (156)-(158) yields,

$$\begin{aligned} \sqrt{\mu_H} \left\| (I - M(x^k)^{-1} \text{Hess } f(x^k)) \eta \right\| &\leq \sqrt{L_H} c(\epsilon) \|\eta\| \\ \implies \left\| (I - M(x^k)^{-1} \text{Hess } f(x^k)) \right\| &\leq \sqrt{\kappa_H} c(\epsilon). \end{aligned} \quad (159)$$

Combining (159) and (146) in (155), we conclude that,

$$B_2 \leq 2\sqrt{\kappa_H} c(\epsilon) \|\widehat{x}^k - \widehat{x}^*\|. \quad (160)$$

c) *Finishing the proof:* We conclude the proof by combining the upper bounds (150), (154), and (160) in (145), and using the fact that $\|\hat{x}^k - \hat{x}^*\| = \mathbf{d}(x^k, x^*)$,

$$\mathbf{d}(x^{k+1}, x^*) \leq 2\sqrt{\kappa_H c(\epsilon)} \mathbf{d}(x^k, x^*) + (C_2 + 2\beta C_3) \mathbf{d}(x^k, x^*)^2. \quad (161)$$

The linear convergence factor in (137) is obtained by noting that the second term on the right-hand side vanishes at a *quadratic rate*. \square

B. Proof of Theorem 3

Proof. We will use the general linear convergence result established in Theorem 5. However, in order to properly account for the gauge symmetry in rotation averaging, we need to invoke Theorem 5 on the quotient manifold that underlies our optimization problem. In the following, we break the proof into three main parts (highlighted in bold). The proof makes heavy use of results regarding Riemannian quotient manifolds. The reader is referred to [26, Chapter 9] for a comprehensive review.

a) *Rotation Averaging and Optimization on Quotient Manifolds:* Following standard references, we denote a Riemannian quotient manifold as $\mathcal{M} = \overline{\mathcal{M}} / \sim$. For rotation averaging (Problem 1), the *total space* is given by $\overline{\mathcal{M}} = \text{SO}(d)^n$. Let $R = \{R_1, \dots, R_n\}$ and $R' = \{R'_1, \dots, R'_n\}$ be two points on $\overline{\mathcal{M}}$. We say that R and R' are equivalent if they are related via a left group action:

$$R \sim R' \iff \exists S \in \text{SO}(d), SR_i = R'_i, \forall i = 1, \dots, n. \quad (162)$$

The equivalence class represented by R is defined as,

$$[R] = \{(SR_1, \dots, SR_n), S \in \text{SO}(d)\}. \quad (163)$$

Note that the cost function of Problem 1 is invariant within an equivalence class. In the following, we use $T_R \overline{\mathcal{M}}$ to denote the usual tangent space at $R \in \overline{\mathcal{M}}$, and $T_{[R]} \mathcal{M}$ to denote the corresponding tangent space on the quotient manifold.

Given a retraction Retr on \mathcal{M} (see [26, Chapter 9.6]), we can execute the Riemannian Newton's method on \mathcal{M} :

$$[R^{k+1}] = \text{Retr}_{[R^k]}(\xi^k), \quad (164)$$

Above, $\xi^k \in T_{[R^k]} \mathcal{M}$ is the solution of the following linear equation,

$$\text{Hess } f([R^k])[\xi^k] = -\text{grad } f([R^k]), \quad (165)$$

where $\text{grad } f([R^k])$ and $\text{Hess } f([R^k])$ denote the Riemannian gradient and Hessian on the quotient manifold, respectively.

b) *Expressing the iterates of Algorithm 4 on the quotient manifold:* Recall that Algorithm 4 generates a sequence of iterates $\{R^k\}$ on the total space $\overline{\mathcal{M}}$. To prove convergence, we need to analyze the corresponding sequence of equivalence classes $\{[R^k]\}$ on the quotient manifold \mathcal{M} . Once we understand how $[R^k]$ evolves, we can prove the desired result by invoking Theorem 5 on the quotient manifold \mathcal{M} . To begin with, we write the update step in Algorithm 4 in the following general form:

$$R^{k+1} = \overline{\text{Retr}}_{R^k}(v^k), \quad (166)$$

where v^k is the vector corresponding to the matrix V^k in line 10; see (20) for how v^k and V^k are related. Together, $\overline{\text{Retr}}_{R^k}(v^k)$ is the concise notation for the update steps in line 11-14, where we update each rotation R_i^k to $\text{Exp}(v_i^k)R_i^k$. Our notation $\overline{\text{Retr}}$ serves to emphasize that the retraction is performed on the total space $\overline{\mathcal{M}}$. Recall from (19)-(21) and Theorem 2 that v^k is a solution to the linear system,

$$(\tilde{L} \otimes I_p)v^k = -\bar{g}(R^k), \quad (167)$$

where $\tilde{L} \approx_\epsilon L \equiv L(G; w)$ is defined in (31) and $\bar{g}(R^k) \in T_{R^k} \overline{\mathcal{M}}$ is the Riemannian gradient in the total space defined in (14). In this proof, we will use the notations \mathcal{N}_R and \mathcal{H}_R to denote the vertical and horizontal spaces at $R \in \overline{\mathcal{M}}$.¹¹ By assumption, v^k is the unique solution to (167) that satisfies $v^k \perp \mathcal{N}_{R^k}$, i.e., $v^k \in \mathcal{H}_{R^k}$. This implies that there is a unique tangent vector $\eta^k \in T_{[R^k]} \mathcal{M}$ on the tangent space of the quotient manifold such that v^k is the *horizontal lift* [26, Definition 9.25] of η^k at R^k :

$$v^k = \text{lift}_{R^k}(\eta^k). \quad (168)$$

At any $R \in \overline{\mathcal{M}}$, define $\overline{M}(R) : \mathcal{H}_R \rightarrow \mathcal{H}_R$ to be the linear map,

$$\overline{M}(R) : v \mapsto (\tilde{L} \otimes I_p)v, \quad (169)$$

where $v \in \mathcal{H}_R$ is any vector from the horizontal space. Since $\ker(\tilde{L} \otimes I_p) = \mathcal{N}_R$, it holds that $\overline{M}(R)$ is invertible on \mathcal{H}_R . Define $M([R]) : T_{[R]} \mathcal{M} \rightarrow T_{[R]} \mathcal{M}$ to be the corresponding linear map on the quotient manifold,

$$M([R]) = \text{lift}_R^{-1} \circ \overline{M}(R) \circ \text{lift}_R. \quad (170)$$

¹¹For rotation averaging, it turns out that definitions of vertical and horizontal spaces do not depend on the point R ; e.g., see (13) for the definition of the vertical space. However, in this proof we will still use the more general notations \mathcal{N}_R and \mathcal{H}_R , which help us to emphasize that \mathcal{N}_R and \mathcal{H}_R are subspaces of the tangent space $T_R \overline{\mathcal{M}}$.

Note that $M([R])$ is indeed linear because when considered as a mapping $\text{lift}_R : T_{[R]}\mathcal{M} \rightarrow \mathcal{H}_R$, the horizontal lift is linear and invertible (see [26, Definition 9.25]). Furthermore, applying lift_R from the left on both sides of (170) shows that for any tangent vector $\eta \in T_{[R]}\mathcal{M}$,

$$\text{lift}_R(M([R])[\eta]) = \overline{M}(R)[\text{lift}_R(\eta)]. \quad (171)$$

By [26, Proposition 9.39], at iteration k , the Riemannian gradients on the total space and quotient space are related via,

$$\bar{g}(R^k) = \text{lift}_{R^k}(\text{grad } f([R^k])). \quad (172)$$

Combining (168)-(172), we see that (167) is equivalent to,

$$\text{lift}_{R^k}(M([R^k])[\eta^k]) = -\text{lift}_{R^k}(\text{grad } f([R^k])). \quad (173)$$

Applying $\text{lift}_{R^k}^{-1}$ to both sides of (173),

$$M([R^k])[\eta^k] = -\text{grad } f([R^k]). \quad (174)$$

In [26, Chapter 9.6], it is shown that $\text{Retr}_{[R]}(\eta) = [\overline{\text{Retr}}_R(\text{lift}_R(\eta))]$. Using this result, we see that the update equation on the total space (166) can be converted to the following update equation, defined on the quotient space:

$$[R^{k+1}] = [\overline{\text{Retr}}_{R^k}(v^k)] = \text{Retr}_{[R^k]}(\eta^k). \quad (175)$$

In summary, let $\{R_k\}$ denotes the iterates generated by Algorithm 4 on the total space $\overline{\mathcal{M}}$. We have shown that $\{R_k\}$ corresponds to a sequence $\{[R^k]\}$ on the quotient space \mathcal{M} that evolves according to (174)-(175).

c) Invoking Theorem 5 on the quotient manifold.: To finish the proof, we will invoke Theorem 5 to show that the sequence of iterates $[R^k]$ generated by (174)-(175) converges linearly to $[R^*]$. This amounts to verifying that each condition in Assumption 1 holds on the quotient manifold \mathcal{M} . To start, note that there exists $r' > 0$ such that for any $R \in \text{SO}(d)^n$, the condition $\mathbf{d}([R], [R^*]) < r'$ implies that $R \in B_r(R^*)$ for some global minimizer R^* in the total space, where $B_r(R^*)$ is the neighborhood within which Theorem 1 and Corollary 1 hold.

Verifying (A1). We need to derive lower and upper bounds for the Hessian of the quotient optimization problem $\text{Hess } f([R])$. For any $\eta \in T_{[R]}\mathcal{M}$, let $v = \text{lift}_R(\eta)$. By [26, Proposition 9.45], we have,

$$\langle \eta, \text{Hess } f([R])\eta \rangle = \langle v, H(R)v \rangle, \quad (176)$$

where $H(R)$ is defined in (15). Since $v \in \mathcal{H}_R \equiv \mathcal{H}$ belongs to the horizontal space, we conclude using Corollary 1 that $\langle v, H(R)v \rangle \geq \mu_H \|v\|^2$ where μ_H is the constant defined in Corollary 1. Furthermore, since the quotient manifold \mathcal{M} inherits the Riemannian metric from the total space $\overline{\mathcal{M}}$, we have $\|\eta\| = \|v\|$. We thus conclude that,

$$\langle \eta, \text{Hess } f([R])\eta \rangle = \langle v, H(R)v \rangle \geq \mu_H \|v\|^2 = \mu_H \|\eta\|^2. \quad (177)$$

Similarly, we can show that $\langle \eta, \text{Hess } f([R])\eta \rangle \leq L_H \|\eta\|^2$ where L_H is also defined in Corollary 1. Therefore,

$$\mu_H I \preceq \text{Hess } f([R]) \preceq L_H I. \quad (178)$$

Verifying (A2). We need to show that $M([R])$ defined in (170) is invertible and the operator norm of its inverse can be upper bounded. The invertibility follows from (170) and the fact that both lift_R and $\overline{M}(R)$ are invertible on the horizontal space. To upper bound $M([R])^{-1}$, it is equivalent to derive a lower bound on $M([R])$. Let $\eta \in T_{[R]}\mathcal{M}$ and $v = \text{lift}_R(\eta)$. We have,

$$\langle \eta, M([R])\eta \rangle = \langle v, \overline{M}(R)v \rangle = v^\top (\tilde{L} \otimes I_p) v \geq \lambda_2(\tilde{L}) \|v\|^2. \quad (179)$$

The last inequality holds because $v \perp \mathcal{N}$. Thus, we conclude that,

$$\|M([R])^{-1}\| \leq 1/\lambda_2(\tilde{L}). \quad (180)$$

Verifying (A3). Lastly, we need to show that the linear map $M([R])$ is a spectral approximation of the Riemannian Hessian $\text{Hess } f([R])$ on the quotient manifold. From Theorem 1, it holds that,

$$H(R) \approx_\delta L \otimes I_p. \quad (181)$$

In addition, from Theorem 2, we have

$$L \approx_\epsilon \tilde{L} \implies L \otimes I_p \approx_\epsilon \tilde{L} \otimes I_p. \quad (182)$$

Composing the two approximations yields,

$$H(R) \approx_{\delta+\epsilon} \tilde{L} \otimes I_p. \quad (183)$$

Note that the above result directly implies the following approximation relation on the quotient manifold,

$$\text{Hess } f([R]) \approx_{\delta+\epsilon} M([R]). \quad (184)$$

To see this, note that for any $\eta \in T_{[R]}\mathcal{M}$ and $v = \text{lift}_R(\eta)$,

$$\begin{aligned}\langle \eta, \text{Hess } f([R])\eta \rangle &= \langle v, H(R)v \rangle \\ &\leq e^{\delta+\epsilon} \langle v, \overline{M}(R)v \rangle \\ &= e^{\delta+\epsilon} \langle \eta, M([R])\eta \rangle.\end{aligned}\tag{185}$$

The same argument leads to,

$$\langle \eta, \text{Hess } f([R])\eta \rangle \geq e^{-\delta-\epsilon} \langle \eta, M([R])\eta \rangle.\tag{186}$$

□

C. Proof of Theorem 4

Proof. We prove this result using induction. The base case of $k = 1$ (first iteration) is true by Theorem 2. Now suppose (38) holds at iteration $k \geq 1$. Define $D^* = M_t^* - M_t^k$. By Theorem 2, the approximate refinement D^k computed at line 10 of Algorithm 5 satisfies,

$$\begin{aligned}\|D^k - D^*\|_L &\leq c(\epsilon) \|D^*\|_L \implies \|D^k + M_t^k - M_t^*\|_L \leq c(\epsilon) \|M_t^k - M_t^*\|_L \\ &\implies \|M_t^{k+1} - M_t^*\|_L \leq c(\epsilon)^{k+1} \|M_t^*\|_L.\end{aligned}\tag{187}$$

The second step above holds by the inductive hypothesis. □

APPENDIX V AUXILIARY LEMMAS

Lemma 5. Let $L, \tilde{L} \in \mathcal{S}_+^n$ such that $L \approx_\epsilon \tilde{L}$. Let $B \in \mathbb{R}^{n \times p}$ be a matrix where each column of B lives in the image of L . Let $X^*, \tilde{X} \in \mathbb{R}^{n \times p}$ be matrices such that $LX^* = B$ and $\tilde{L}\tilde{X} = B$. Then,

$$\|X^* - \tilde{X}\|_L \leq c(\epsilon) \|X^*\|_L,\tag{188}$$

where $c(\epsilon) = \sqrt{1 + e^{2\epsilon} - 2e^{-\epsilon}}$.

Proof. We note that the proof of a similar result can be found at [24, Claim 2.4]. In the following, we provide the proof for the case where L and \tilde{L} are singular. The non-singular case can be proved in the same way by replacing matrix psuedoinverse with the inverse. Observe that

$$\|X^* - \tilde{X}\|_L^2 = \sum_{i=1}^p \|X_{[:,i]}^* - \tilde{X}_{[:,i]}\|_L^2,\tag{189}$$

where $X_{[:,i]}^*$ denotes the i -th column of X^* . Therefore, we can first obtain an upper bound for the squared norm on a single column. To simplify notation, let x^* be a column of X^* , and let \tilde{x} and b be the corresponding columns of \tilde{X} and B . Let us expand the squared norm,

$$\|x^* - \tilde{x}\|_L^2 = x^{*\top} L x^* - 2x^{*\top} L \tilde{x} + \tilde{x}^\top L \tilde{x}.\tag{190}$$

Note that since $L \approx_\epsilon \tilde{L}$, we have $\ker(L) = \ker(\tilde{L})$. In addition, any \tilde{x} where $\tilde{L}\tilde{x} = b$ can be written as $\tilde{x} = \tilde{L}^\dagger b + \tilde{x}_\perp$ for some $\tilde{x}_\perp \in \ker(\tilde{L})$. Now, let us consider the middle term in (190),

$$x^{*\top} L \tilde{x} = x^{*\top} L \tilde{L}^\dagger b = x^{*\top} L \tilde{L}^\dagger L x^* = (L^{1/2} x^*)^\top (L^{1/2} \tilde{L}^\dagger L^{1/2}) (L^{1/2} x^*).\tag{191}$$

The relation $\tilde{L} \approx_\epsilon L$ implies $\tilde{L}^\dagger \approx_\epsilon L^\dagger$, which is equivalent to,

$$e^{-\epsilon} \Pi \preceq L^{1/2} \tilde{L}^\dagger L^{1/2} \preceq e^\epsilon \Pi,\tag{192}$$

where Π denotes the orthogonal projection onto $\text{image}(L^{1/2} \tilde{L}^\dagger L^{1/2}) = \text{image}(L)$. By construction, it holds that $L^{1/2} x^* \in \text{image}(L)$. Therefore,

$$x^{*\top} L \tilde{x} = (L^{1/2} x^*)^\top (L^{1/2} \tilde{L}^\dagger L^{1/2}) (L^{1/2} x^*) \geq e^{-\epsilon} \|x^*\|_L^2.\tag{193}$$

Next, expand the last term in (190):

$$\begin{aligned}\tilde{x}^\top L \tilde{x} &= b^\top \tilde{L}^\dagger L \tilde{L}^\dagger b = x^{*\top} L \tilde{L}^\dagger L \tilde{L}^\dagger L x^* \\ &= (L^{1/2} x^*)^\top (L^{1/2} \tilde{L}^\dagger L^{1/2}) (L^{1/2} \tilde{L}^\dagger L^{1/2}) (L^{1/2} x^*) \\ &= \left\| (L^{1/2} \tilde{L}^\dagger L^{1/2}) (L^{1/2} x^*) \right\|_2^2.\end{aligned}\tag{194}$$

Using (192), we conclude that,

$$\tilde{x}^\top L \tilde{x} \leq e^{2\epsilon} \|x^*\|_L^2.\tag{195}$$

Combining (193) and (195) in (190) yields,

$$\|x^* - \tilde{x}\|_L^2 \leq (1 + e^{2\epsilon} - 2e^{-\epsilon}) \|x^*\|_L^2 = c(\epsilon)^2 \|x^*\|_L^2. \quad (196)$$

Finally, using this upper bound on (189) yields the desired result,

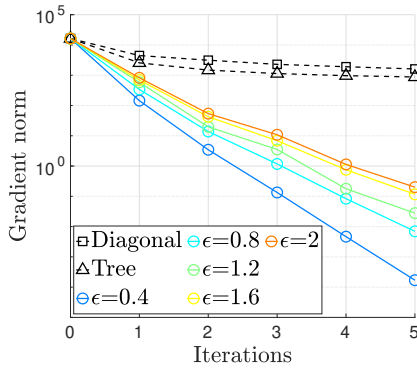
$$\begin{aligned} \|X^* - \tilde{X}\|_L^2 &= \sum_{i=1}^p \|X_{[:,i]}^* - \tilde{X}_{[:,i]}\|_L^2 \\ &\leq \sum_{i=1}^p c(\epsilon)^2 \|X_{[:,i]}^*\|_L^2 \\ &= c(\epsilon)^2 \|X^*\|_L^2. \end{aligned} \quad (197)$$

□

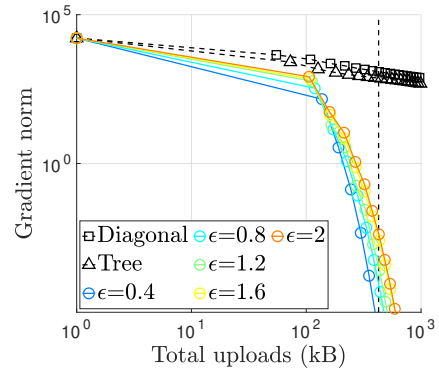
APPENDIX VI EXPERIMENT DETAILS AND ADDITIONAL RESULTS

TABLE VI: Rotation averaging on benchmark SLAM datasets with 5 robots under the **squared geodesic distance cost function**. $|\mathcal{V}|$ and $|\mathcal{E}|$ denote the total number of rotation variables and measurements, respectively. We run the baseline **Newton** method and the proposed method (Algorithm 4) with sparsification parameter $\epsilon = 1.5$, and compare the number of iterations, uploads, and downloads to reach a Riemannian gradient norm of 10^{-5} . For the proposed method, we also show the sparsity achieved by sparsification (lower is better). Results averaged across 5 runs.

Datasets	$ \mathcal{V} $	$ \mathcal{E} $	Iterations		Uploads (kB)		Downloads (kB)		Achieved sparsity (%)
			Newton	Proposed	Newton	Proposed	Newton	Proposed	
Killian Court (2D)	808	827	1	1	0.8	0.5	0.3	0.3	100
CSAIL (2D)	1045	1171	1	4	3.6	5.9	1.2	4.6	97.3
INTEL (2D)	1228	1483	1	3.4	3.5	5	1.1	3.7	96.1
Manhattan (2D)	3500	5453	1	4.8	59.5	48.3	6.3	30.1	38.8
KITTI 00 (2D)	4541	4676	1	1	6.6	4.4	2.2	2.2	100
City (2D)	10000	20687	1	4	225.1	351.5	64.5	258.1	97.2
Garage (3D)	1661	6275	1	2	274.4	88.9	35.8	71.6	93.4
Sphere (3D)	2500	4949	2	8.4	2548.8	104	19.2	80.6	16.9
Torus (3D)	5000	9048	3	9	10423.7	218.1	57	170.9	12.4
Grid (3D)	8000	22236	3	8.8	206871.6	857.9	220.8	647.5	2.8
Cubicle (3D)	5750	16869	2	6.2	7015	407.9	107.7	333.9	19.9
Rim (3D)	10195	29743	2	9	26828.9	568.4	104.5	470.4	6.6



(a) Gradient norm vs. iterations



(b) Gradient norm vs. uploads

Fig. 14: Evaluation of Algorithm 5 on the 5-robot translation estimation problem from the **Cubicle** dataset. (a) Evolution of gradient norm as a function of iterations. (b) Evolution of gradient norm as a function of total uploads to the server.

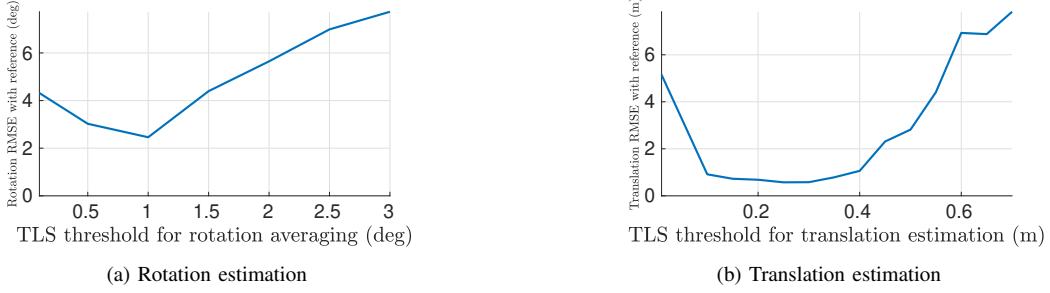


Fig. 15: Sensitivity of robust PGO initialization to TLS thresholds.

Initialization of RBCD++. In Table II, we initialize RBCD++ using a procedure that requires a single round of communication between the server and all robots, and furthermore is expected to be more accurate than the spanning tree initialization. In the following, let $\alpha \in \mathbb{N}$ denote the robot index. For each pose variable $i \in \mathcal{V}$ in the multi-robot pose graph, let $\alpha(i)$ denote the robot that owns this pose. At a high level, the initialization approach we implement for RBCD++ first lets robots solve local PGO problems in parallel, and then lets the server align the local trajectory estimates by solving another PGO problem defined using all inter-robot loop closures. We outline the steps in detail below:

- 1) In parallel, each robot solves a local PGO problem using SE-Sync [60] by considering all local odometry and intra-robot loop closures. For each pose variable $i \in \mathcal{V}$, this step returns an estimate in the corresponding robot's local frame, denoted as $\hat{T}_i^{\alpha(i)} \in \text{SE}(d)$.
- 2) The server jointly estimates the transformation of each robot α to the global frame, denoted as $T_\alpha = (R_\alpha, t_\alpha) \in \text{SE}(d)$, by solving the following PGO problem using SE-Sync,

$$\underset{R_\alpha \in \text{SO}(d), t_\alpha \in \mathbb{R}^d}{\text{minimize}} \sum_{(i,j) \in \mathcal{E}_{\text{inter}}} \kappa_{ij} \left\| R_{\alpha(i)} \hat{R}_{\alpha(j)}^{\alpha(i)} - R_{\alpha(j)} \right\|_F^2 + \tau_{ij} \left\| t_{\alpha(j)} - t_{\alpha(i)} - R_{\alpha(i)} \hat{t}_{\alpha(j)}^{\alpha(i)} \right\|_2^2. \quad (198)$$

In (198), $\mathcal{E}_{\text{inter}}$ denotes the set of inter-robot loop closures. Constants $\kappa_{ij}, \tau_{ij} > 0$ are the rotation and translation measurement weights associated with the inter-robot loop closure $(i, j) \in \mathcal{E}_{\text{inter}}$. Each $\hat{T}_{\alpha(j)}^{\alpha(i)} \triangleq (\hat{R}_{\alpha(j)}^{\alpha(i)}, \hat{t}_{\alpha(j)}^{\alpha(i)}) \in \text{SE}(d)$ is an estimate of the relative transformation between robots $\alpha(i)$ and $\alpha(j)$ where $\alpha(i) \neq \alpha(j)$, computed as,

$$\hat{T}_{\alpha(j)}^{\alpha(i)} = \hat{T}_i^{\alpha(i)} \tilde{T}_{ij} \left(\hat{T}_j^{\alpha(j)} \right)^{-1}. \quad (199)$$

In (199), $\tilde{T}_{ij} \in \text{SE}(d)$ is the original inter-robot loop closure, and $\hat{T}_i^{\alpha(i)}, \hat{T}_j^{\alpha(j)} \in \text{SE}(d)$ are the pose estimates in robots' local frames computed in step 1.

- 3) For each pose variable $i \in \mathcal{V}$ in the pose graph, its final initialization (input to RBCD++) is computed as,

$$\hat{T}_i = \hat{T}_{\alpha(i)} \hat{T}_i^{\alpha(i)}, \quad (200)$$

where $\hat{T}_{\alpha(i)} \in \text{SE}(d)$ is robot $\alpha(i)$'s coordinate frame estimated in step 2.

Impact of Spectral Sparsification on Translation Estimation. In Fig. 14, we evaluate the impact of spectral sparsification on Algorithm 5 for collaborative translation estimation. For conciseness, we only evaluate convergence as a function of iteration (Fig. 14a) and uploads (Fig. 14b). Using the Cubicle dataset, we generate the translation estimation problem by fixing the rotation estimates in PGO (10) to the solution produced by Algorithm 4; see our discussions in Sec. III-D. Note that for translation estimation, setting $\epsilon = 0$ (*i.e.*, no sparsification) in Algorithm 5 corresponds to the exact Newton method and recovers the exact solution in a single iteration (since Problem 2 is a linear least squares problem). In Fig. 14b, the vertical line shows the total uploads incurred with this setting. We run Algorithm 5 under varying sparsification parameter ϵ . Similar to the rotation averaging experiment, we introduce two baselines in which each robot heuristically sparsifies its Schur complement matrix S_α according to a diagonal sparsity pattern (Diagonal) or a tree sparsity pattern (Tree). Our results in Fig. 14 show that the proposed method dominates the baselines in terms of both iteration and communication complexity. Furthermore, spectral sparsification provides a way to trade off accuracy with communication efficiency. For instance, to obtain an approximate solution, we can run Algorithm 5 with $\epsilon = 0.4$ and terminate when the gradient norm reaches 10^{-1} , which would incur less communication compared to recovering the exact solution with $\epsilon = 0$.

Sensitivity of robust PGO initialization to TLS thresholds. In Fig. 15, we evaluate the sensitivity of our two-stage robust PGO initialization to the choice of TLS thresholds on the real-world collaborative SLAM dataset (Sec. VI-C). First, for rotation estimation, Fig. 15a shows the final rotation RMSE achieved by GNC as a function of the TLS threshold. We observe that setting the threshold between 0.5 deg to 1.5 deg produces the best performance. For values too small, GNC starts to reject correct (*i.e.* inlier) measurements, while for large values the final solution is negatively influenced by outliers. Fig. 15b repeats the analysis for the translation estimation stage. While a similar trend is observed, the result shows that GNC is less sensitive to the TLS threshold in translation estimation.